Development of a robotic system for CubeSat Attitude Determination and Control System ground tests

Irina Gavrilovich

THÈSE
Pour obtenir le grade de
Docteur

Délivré par **Université de Montpellier**

Préparée au sein de l'école doctorale
Information, Structures, Systèmes (I2S)
Et de l'unité de recherche
Laboratoire d'Informatique, de Robotique et de
Microélectronique de Montpellier (LIRMM)

Spécialité : **SYAM**

Présentée par **Irina GAVRILOVICH**

DEVELOPMENT OF A ROBOTIC SYSTEM FOR CUBESAT ATTITUDE DETERMINATION AND CONTROL SYSTEM GROUND TESTS

Soutenue le 14 Décembre 2016 devant le jury composé de

Laurent Dusseau	Professeur	UM, Centre Spatial Universitaire	Président
François Pierrot	DR CNRS	LIRMM	Directeur
Sébastien Krut	CR CNRS	LIRMM	Encadrant
Marc Gouttefarde	CR CNRS	LIRMM	Encadrant
Gabriel Abba	Professeur	Université de Lorraine	Rapporteur
Paolo Tortora	Assoc. Prof.	Université de Bologne	Rapporteur
Sabrina Corpino	Assist. Prof	Ecole Polytechnique de Turin	Examinateur

Resume

Après le lancement du premier satellite artificiel en 1957, l'évolution de diverses technologies a favorisé la miniaturisation des satellites. En 1999, le développement des nano-satellites modulaires appelés CubeSats, qui ont la forme d'un cube d'un décimètre de côté et une masse de 1 kg à 10 kg, a été initié par un effort commun de l'Université polytechnique de Californie et de l'Université de Stanford. Depuis lors, grâce à l'utilisation de composants électroniques standards à faible coût, les CubeSats se sont largement répandus.

Au cours des dernières années, le nombre de CubeSats lancés a régulièrement augmenté, mais moins de la moitié des missions ont atteint leurs objectifs. L'analyse des défaillances des CubeSats montre que la cause la plus évidente est le manque d'essais adéquats des composants du système ou du système au complet. Parmi les tâches particulièrement difficiles, on compte les essais « hardware-in-the-loop » (HIL) du système de contrôle d'attitude et d'orbite (SCAO) d'un CubeSat. Un système dédié à ces essais doit permettre des simulations fiables de l'environnement spatial et des mouvements réalistes des CubeSats. La façon la plus appropriée d'obtenir de telles conditions d'essai repose sur l'utilisation d'un coussin d'air. Toutefois, les mouvements du satellite sont alors contraints par les limites géométriques, qui sont inhérentes aux coussins d'air. De plus, après 15 années de développements de CubeSats, la liste des systèmes proposés pour tester leur SCAO reste très limitée.

Aussi, cette thèse est consacrée à l'étude et à la conception d'un système robotique innovant pour des essais HIL du SCAO d'un CubeSat. La nouveauté principale du système d'essai proposé est l'usage de quatre coussins d'air au lieu d'un seul et l'emploi d'un robot manipulateur. Ce système doit permettre des mouvements non contraints du CubeSat. Outre la conception du système d'essai, cette thèse porte sur les questions liées: (i) à la détermination de l'orientation d'un CubeSat au moyen de mesures sans contact; (ii) au comportement de l'assemblage des coussins d'air; (iii) à l'équilibrage des masses du système.

Afin de vérifier la faisabilité de la conception proposée, un prototype du système d'essai a été développé et testé. Plusieurs modifications destinées à en simplifier la structure et à réduire le temps de fabrication ont été effectuées. Un robot Adept Viper s650 est notamment utilisé à la place d'un mécanisme sphérique spécifiquement conçu. Une stratégie de commande est proposée dans le but d'assurer un mouvement adéquat du robot qui doit suivre les rotations du CubeSat. Finalement, les résultats obtenus sont présentés et une évaluation globale du système d'essai est discutée.

After the launch of the first artificial Earth satellite in 1957, the evolution of various technologies has fostered the miniaturization of satellites. In 1999, the development of standardized modular satellites with masses limited to a few kilograms, called CubeSats, was initiated by a joint effort of California Polytechnic State University and Stanford University. Since then, CubeSats became a widespread and significant trend, due to a number of available off-the-shelf low cost components.

In last years, the number of launched CubeSats constantly grows, but less than half of all CubeSat missions achieved their goals (either partly or completely). The analysis of these failures shows that the most evident cause is a lack of proper component-level and system-level CubeSat testing. An especially challenging task is Hardware-In-the-Loop (HIL) tests of the Attitude Determination and Control System (ADCS). A system devoted to these tests shall offer reliable simulations of the space environment and allow realistic CubeSat motions. The most relevant approach to provide a satellite with such test conditions consists in using air bearing platforms. However, the possible satellite motions are strictly constrained because of geometrical limitations, which are inherent in the air bearing platforms. Despite 15 years of CubeSat history, the list of the air bearing platforms suitable for CubeSat ADCS test is very limited.

This thesis is devoted to the design and development of an air bearing testbed for CubeSat ADCS HIL testing. The main novelty of the proposed testbed design consists in using four air bearings instead of one and in utilizing a robotic arm, which allows potentially unconstrained CubeSat motions. Besides the testbed design principle, this thesis deals with the related issues of the determination of the CubeSat orientation by means of contactless measurements, and of the behavior of the air bearings, as well as with the need of a mass balancing method.

In order to verify the feasibility of the proposed design, a prototype of the testbed is developed and tested. Several modifications aimed at simplifying the structure and at shortening the fabrication timeline have been made. For this reason, the Adept Viper s650 robot is involved in place of a custom-designed 4DoF robotic arm. A control strategy is proposed in order to provide the robot with a proper motion to follow the CubeSat orientation. Finally, the obtained results are presented and the overall assessment of the proposed testbed is put into perspective.

Acknowledgements

First and foremost I would like to acknowledge my thesis director, Prof. François Pierrot, who accepted me as a Ph.D student at the LIRMM and has believed in my research. I would like to express my sincere gratitude to my thesis advisors, Sébastien Krut and Marc Gouttefarde, for they continuous support and guidance during these 3 years. Sébastien was the first person who welcomed me at the LIRMM and since then he has always provided me with encouragement and valuable advices whenever it was needed. I am very grateful to him for knowledge he has shared with me and all time he has spent to facilitate my habituation to the new domain. I appreciate all his contributions of energy, ideas and funding to make my research productive. Besides that he has helped me identify my professional strengths and accept them. I would like to thank Marc for his assistant with all my writings and his patience to correct them. I dare to believe that all his efforts to improve my writing skills were not in vain. They both, Sébastien and Marc, have taught me, equally consciously and unconsciously, how good research is done.

My research would not have been possible without support of the Montpellier-Nîmes University Space Center (CSU) and funding from the Van Allen Foundation. I wish to thank these organizations and personally Prof. Laurent Dusseau and Prof. Frédéric Saigné for giving me the invaluable opportunity to fulfill myself as a researcher, to present results of my work on several conferences and to write this thesis.

I would like to thank my colleagues from the Robotics Department for their readiness to help and to share their experience. Especially, I am grateful to Samah Shayya for his short in time, but very informative introduction to the Simulink Real-Time and Speedgoat target, and to Alonso Sanches who has aided me deal with the Viper robot and provided his C++ code that saved me a good half-year of work.

Let me also mention my friends who have been responsible for the entertainment aspects of my life during these years: Nastya, Artem, Andrey, Roman, Viyas. I appreciate their support, advices and all wonderful moments we have spent together, and I hope our friendship will last long despite distances and boarders.

I would like to express my deepest gratitude to my family that was the most supportive and motivating team I could ever imagine. I warmly thank my mom who bravely let me go in my big journey abroad and has always selflessly supported me in all my pursuits. And I especially thank my beloved husband who has always been on my side during these years. He has encouraged me when I needed it, he has inspired me when I ran out of new ideas, and he has never let me give up. More than I can express I am grateful to him for his faith in me and my intellect, unbelievable patience and endless love.

Lastly, I would like to thank everyone who has aided me on my long way to the Ph.D degree, those who has assisted to make my experiment happen, who has helped me deal with administrative and bureaucratic issues and those who has simply been around to cheer me up, and my cat that has comforted me with purring at the most tense moments of these three years.

CONTENTS

LIST OF FIGURES

LIST OF TABLES

ACRONYMS

ADCS	Attitude Determination and Control System
C&DH	Command and Data Handling
CAD	Computer-aided design
CoM	Center of mass
CoR	Center of rotation
COTS	Commercial-off-the-shelf
DAC	Data acquisition card
DoF	Degree of freedom
EPS	Electrical Power System
EVA	Extra-vehicular activity
FOV	Field of view
GC	Geometrical center
GNC	Guidance, Navigation and Control
GPS	Global Positioning System
HIL	Hardware-in-the-loop
IMU	Inertial measurement unit
ISS	International Space Station
LEO	Low Earth orbit
LS	Least Square
MEMS	Micro-Electro-Mechanical System
OPW	Ortho-parallel manipulator with spherical wrist
P-POD	Poly-Picosatellite Orbital Deployer
SIL	Software-in-the-loop

INTRODUCTION

The history of space exploration started in 1957 with the launch of the first artificial Earth satellite. This event opened the door for thousands of space missions to be launched, including inhabited space stations, manned and unmanned Moon expeditions, and deep space exploration. The success of many of these missions significantly impacted technology and science. Years later, and despite the progress of manned missions, satellites are in high demand in numerous domains, such as telecommunications, technological, educational and scientific projects, Earth, sun-orbiting planet and asteroid observations, and defense programs.

Satellite technology has significantly evolved since the 1960s. These technological changes have affected not only the performance capabilities of satellites, but also their size. Thus, thanks to the minimization of electric and other components, and with masses similar to those of older satellites, modern satellites are able to perform a wider range of tasks. This is particularly true for spacecraft intended to operate at large distances from Earth, as illustrated by Mars exploration missions: Viking 1[1], the first spacecraft to successfully land on Mars in 1975, and Mars Science Laboratory (MSL)[2], with the Curiosity rover, which landed in 2012, had similar fueled (3,527 kg and 3,893 kg) and lander (572 kg and 899 kg) masses. Besides a mobility system designed to exceed a total distance of at least 19 km, Curiosity contains 13 on-board instruments, which allow an incomparably wider range of investigations than was available with the Viking 1 lander. However, not only did the performance of the spacecraft increase, but their masses also decreased for the same range of function capabilities. This is illustrated by several satellites designed for Earth observation in the last 20 years. Spot 5[3] (3,030 kg, launched in 2002), RapidEye[3] (150 kg, launched in 2008) and Flock[3] (5 kg, launched in 2014) were intended for similar purposes, yet had dramatically different masses and – consequently – project cost structures.

The evolution of technology has thusly fostered the miniaturization of satellites. In 1999, the CubeSat program was started. CubeSats are standardized modular nanosatellites (with masses limited to few kilograms), which have to be built according to specifications guaranteeing their compatibility with deployment systems. Furthermore, commercial off-the-shelf components are widely used in CubeSat design. As a whole, CubeSat guidelines make for shorter development timelines and lower expenses. As a result, CubeSats have therefore become a popular bus for space missions. Every year, the number of CubeSat launches increases; their mission objectives become more and more sophisticated and ambitious. Hence, the first CubeSats, launched in 2003, were mainly devoted to amateur radio and technology demonstrations. Today, they increasingly complement deep space missions: In 2017, INSPIRE[4] will demonstrate CubeSat functionality in deep space and, later on, MarCO[5] will fly independently to the Mars orbit to perform telecommunication

[1] http://www.jpl.nasa.gov/missions/viking-1/
[2] http://mars.jpl.nasa.gov/msl/
[3] https://directory.eoportal.org
[4] http://www.jpl.nasa.gov/cubesat/missions/inspire.php
[5] http://www.jpl.nasa.gov/cubesat/missions/marco.php

tasks. The anticipated success of these CubeSat missions will usher the era of deep space nanosatellites, making the exploration of the Solar system faster and cheaper. Obviously, such missions require more sophisticated architecture of satellite subsystems.

The trend towards more complex CubeSats presents higher risks of failure. Indeed, the specific operational parameters of the space environment render spacecraft repair almost impossible. This is particularly true for small satellites, because repair costs usually vastly exceed total satellite production and launch costs. In the history of space flights, successful on-orbit repairs have been made only to inhabited orbital stations, the Solar Maximum Mission and the famous Hubble Space Telescope. It is therefore essential that potential satellite malfunctions be identified and fixed before their launch.

One of the most complex and sensitive subsystems of a satellite is the Attitude Determination and Control System (ADCS), which determines the satellite's orientation and controls its stabilization, pointing and maneuvers.

Several techniques are used to perform ADCS component ground tests. However, testing the whole system is challenging because it requires simulating spatial conditions and effects, as well as satellite dynamics. Simulators were initially designed in the early 1960s (Smith, 1965). They allowed the placement of the satellite's ADCS components on an air bearing table which eliminated friction. Precise mass balancing ensured minimized gravity torque effects; sensor signals were simulated electrically or optically. These systems were used mainly for control law studies and rarely for assembled hardware evaluations. Since then, the architecture of test platforms has not undergone significant changes. While other techniques to simulate low-torque environment were developed, the use of air-bearing platforms remains prevalent for the complete testing of satellite ADCS.

However advanced, the test systems developed for larger satellites are not adapted for small satellite testing – still less for CubeSat testing. The main issue is the unacceptable level of residual perturbations caused – mostly – by the respectively large mass and moments of inertia of the table. This thesis is devoted to the design and development of an experimental system suitable for CubeSat ADCS evaluation. Additionally, a task to extend the performance range of existent air bearing testbeds is proposed. To this end, a robotic gimbal is used to widen the rotational freedom of the CubeSat on the testbed. In spacecraft design, manipulators are used widely and for a variety of purposes. The most renowned examples are the manipulators used on the Space Shuttle and the International Space Station: Canadarm and Canadarm2, Dextre, the European Robotic Arm and the Remote Manipulator System. They were built to perform various tasks, such as moving cargo and equipment, assisting with station assembly and docking, and even providing assistance to astronauts working in space. The Canadarm was used in the repair missions mentioned above. However, examples of a robotic arm application for air bearing ADCS testbeds were not found in the literature.

This thesis is organized in four chapters:

Chapter 1 introduces the historical and statistical background of CubeSats. This information is necessary to understand the motivation for the thesis. Subsequently, an overview of the CubeSat subsystem is presented, with a focus on the ADCS. Further, an introduction to CubeSat ground testing is given. It is followed by a detailed State-of-the-Art review of test facilities for satellite ADCS, ranging from 1960's CubeSat test platforms to the most current ones. This review highlights the shortcomings and limitations of current test systems, and presents the motivation for the development of a new ADCS testbed for CubeSats. Finally, based on the calculations of the perturbations experienced by a CubeSat in the space environment, technical requirements for the testbed are formulated.

Chapter 2 proposes three approaches to extending the performance range of a CubeSat ADCS testbed and to satisfying the aforementioned requirements. All three approaches rely on the use of air bearings as a means to minimize friction, but the manner in which unconstrained rotation is provided to the CubeSat differs. One of these approaches is selected for implementation: It is based on a novel way to combine spherical air bearings with a robotic gimbal. This testbed concept, called AirBall, is presented, and the design of its prototype is described in details.

Chapter 3 introduces the numerical simulations required to verify the feasibility of the proposed testbed concept. First, the study of the behavior of the air bearing assembly is presented with related simulation results. Further, techniques required to determine CubeSat orientation and perform mass balancing are described. The results of the simulations illustrate the efficiency of those newly developed techniques.

Chapter 4 is devoted to experimentations with the AirBall prototype. Specifically, test objectives, experiment setup and results are presented. Additionally, the control strategy required to use the Viper s650 robot arm is examined.

In *the Conclusion*, an overall assessment of the proposed AirBall testbed is given and put into perspective. It includes concluding remarks about the prototype's performance and perspectives for future work.

The main contributions of this thesis can be outlined as follows:

- **The design and development of an experimental testbed with a robotic gimbal for CubeSat ADCS testing**. The AirBall testbed employs a novel concept of the air bearing platform, whose essential part is a spherical assembly comprising four air bearings. CubeSats can conveniently be placed in the center of the sphere; the system provides it with unconstrained rotation.
- **The assessment of an air bearing platform's behavior,** including the analysis of the relative platform and payload motions.
- **The determination of CubeSat orientation** using contactless indirect measurements. The system is capable of providing information about the angular position of a rotating rigid body via a minimum of three distance sensors.
- **A mass balancing technique for CubeSat** testbeds without any actuation means. Related algorithms are proposed and confirmed by the simulation results.

Chapter 1. CubeSat Testbed State Of The Art

1.1 Introduction

Since CubeSat program has started in 1999, CubeSat-class nanosatellites became a widespread and significant trend. Due to low cost and a number of off-the-shelf components, the development of such satellites became common, especially among school and universities. Building a CubeSat takes less time than needed to design a nanosatellite from scratch. Hence, developers can focus on scientific payload integration and students can lead the project through all stages during their university years. Despite small sizes and standardized construction, CubeSats are useful to solve wide range of tasks in different fields of space exploration - communication, earth and near-earth space observation, scientific missions.

Despite a significant difference in size, CubeSats inherit their system architecture from previous generations of satellites. All systems required to ensure CubeSat functions are similar to those of large satellites, but their complexity and component selection are constrained by strict size and mass requirements. Besides these constrains, CubeSat developers are often limited by budget and timeline that results in wide usage of commercial-off-the-shelf (COTS) components with minimum or zero space heritage. Malfunction of one element in a system is enough to bring a whole satellite failure. In order to verify that components keep their functions under space environment and the CubeSat operates properly, ground tests shall be performed for every involved component and system.

The Attitude Determination and Control System (ADCS) is one of the most difficult systems to test. The ADCS verification requires dynamic simulations of the space environment and some freedom of the CubeSat motion. There are several techniques to permit satellite motion in a low-torque environment, i.e. an environment with minimized gravity and friction torques. Every technique has its own advantages and disadvantages, and the air bearing platform is the most widely used approach. Air bearing platforms for large satellites have been developed for more than 50 years. However, they cannot be adopted for CubeSat tests due to several distinctions.

This Chapter is devoted to the survey of the CubeSat ground test facilities and, particularly, air bearing testbeds. Section 1.2 gives an introduction into CubeSats, including a general overview of this class of nanosatellites, a statistical analysis of CubeSat missions and lessons to be learnt from the past 15 years of CubeSat development. Section 1.3 introduces the ADCS architecture, its essential components, and distinctive features of CubeSat ADCS. The prior to launch satellite verification philosophy is presented in Section 1.4 together with the typical strategy of the CubeSats tests. Section 1.5 is focused on the overview of satellite ground test facilities and, especially, existing air bearing platforms for ADCS dynamic tests. Section 1.6 is dedicated to the state of the art of the air bearing platforms suitable for CubeSats. The main goal of this thesis is stated in Section 1.7 together with the requirements to be fulfilled. In Section 1.8 the conclusion of the Chapter is given.

1.2 CUBESATS IN BRIEF

1.2.1 What is a CubeSat?

Almost fifty years after the beginning of the Space Age, the CubeSat standard was initiated as a response to the current principle of the satellites: "Smaller, Cheaper, Faster, Better" [1]. The concept of a nanosatellite with mass <1 kg and the size of a 10 cm cube was publicly proposed in 2000 as result of a cooperation between California Polytechnic State University (Cal Poly) and Stanford University. And shortly after, this concept evolved to the unified nanosatellite platform called CubeSat that consists of one (1U) or multiple (0.5U, 3U, etc.) standardized 100x100x113.5 mm cubic units with mass not exceeding 1.33kg per unit. The first CubeSats were successfully launched in June 2003, and in ten years their number has exceeded one hundred. By April 2016, there are 431 CubeSats-class missions designed in various institutions all over the world and launched, more of them are scheduled for the coming years [2].

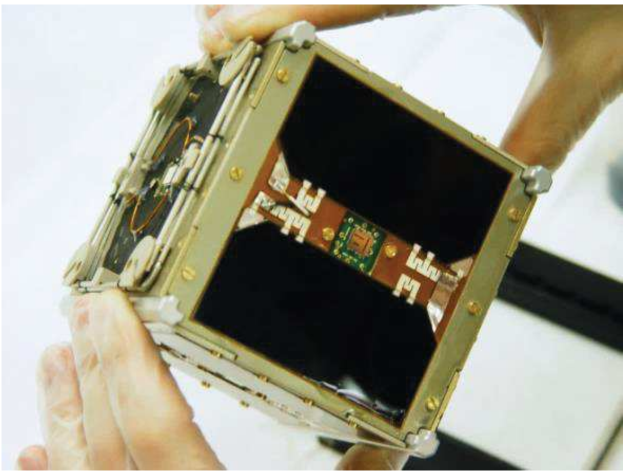

Figure 1.2-1 DTUsat-1 (Technical University of Denmark), one of first CubeSats launched in June 2003 [3]

By the original definition, a CubeSat is compatible with the deployment container Poly-Picosatellite Orbital Deployer (P-POD), which is developed by Cal Poly and Stanford. P-POD provides a standardized launch interface and is able to carry a total of 3U. Several equivalent interfaces, designed by other organizations, are also dedicated to be compatible with the CubeSats [4]:

- Innovative Solutions in Space (ISIS): ISIPOD;
- Japan Aerospace Exploration Agency (JAXA): J-POD;
- NASA: Nanosatellite Launch Adapter Systems (NLAS);
- University of Toronto Space Flight Laboratory (SFL): T-POD and X-POD;
- U.S. Department of Defense: Space Shuttle Picosatellite Launcher (SSPL);
- Astro- und Feinwerktechnik Adlershof GmbH: PicoSatellite Launcher (PSL).

Additionally, the following systems shall be mentioned, as they allow deploying CubeSats from the International Space Station (ISS):

- JAXA: JEM Small Satellite Orbital Deployer (J-SSOD) [5];
- NanoRacks: NanoRacks CubeSat Deployer (NRCSD) [6].

These deployers vary in their internal dimensions and some other constrains. Thus, ISIPOD admits 3U CubeSats with mass up to 6 kg, while P-POD requires 3U to not exceed 4 kg. Some containers allow a custom design to accommodate up to 6U, or provide individual placement for 1U and 2U, that let CubeSat developers be more independent, when scheduling a launch. Despite these differences, the CubeSats shall meet common requirements given by the CubeSat Design Specification [7] that guarantees their compatibility.

Standardized launch containers and strict CubeSat mass limits lead to minimized launch and integration cost. The P-POD and its analogues allow CubeSats to be mounted on various launch vehicles and give great flexibility for seeking launch opportunity [8]. This makes the CubeSat and deployment container tandem an ideal secondary payload.

Figure 1.2-2 The 3U CubeSat O/OREOS is being inserted into a P-POD. Photo: NASA

In addition to featuring miniature dimensions and having standardized deployment systems, CubeSats are remarkable as a standard small-scale satellite platform. The platform (or bus) is the infrastructure of a satellite supporting different mission-oriented payloads. Using standard platforms, a customer does not have to develop the satellite from scratch and can focus on the desired experiment and payload. Comparing to a one-off, this approach to design spacecrafts reduces costs and improves operability. As for any other satellite, a CubeSat bus consists of several subsystems [9]:

- Command and Data Handling (C&DH)
- Telecommunication System
- Electrical Power System (EPS)
- Thermal Control
- Attitude Determination and Control System (ADCS)
- Guidance, Navigation & Orbit Control (GNC)
- Structure and mechanisms
- Propulsion

However, for several missions, some of the subsystems listed above are excessive and can be omitted. For example, propulsion system is a rare choice for CubeSats, because the latter generally stay on their initially reached orbit. But some CubeSats have thrusters on board: ESTCube-1 was aimed at making an experiment with an electric solar wind sail [10]; Lunar IceCube (NASA), designed to fly to the Moon orbit in 2018, make use of a miniature electric ion engine [11]. Also, ADCS is missing on some CubeSats, whose missions do not require the attitude control (instead, having free rotation). In the following Sections, this aspect will be discussed in details. Other subsystems, even with significant performance degradation comparing to full-scale satellites, always have to be part of the CubeSat bus.

The wide choice of COST components for the mechanical structure and subsystems makes the CubeSat a great customized platform for educational and technological missions, which have to be completed in 1-2 years. Indeed, each subsystem can be assembled of the components available in number of specialized CubeSat shops [12]–[14]. Besides, CubeSats are able to perform quite complicated missions competing with larger satellites. Such missions require newly developed components and subsystems that imply more time and higher costs to build the satellite. However, the obvious advantages of the simplified integration and low launch cost attract more satellite developers every year to choose CubeSats.

1.2.2 Success and failure

The CubeSat features stated above, lead to the large popularity of these nanosatellites. As Figure 1.2-3 shows, the number of CubeSats dramatically increased in 2013 and still grows every year.

Thanks to accessibility of CubeSats, 34 countries performed their own space mission so far, and for 14 of them, it was the first satellite launch. More than 150 CubeSats have been developed by universities for educational, science, communication or technology demonstration purposes. Besides, 182 of 431 CubeSats are built by private organizations for commercial uses. The world's largest constellation of Earth-imaging satellites, called the Flock and reckoned at 77 successfully launched CubeSats [15], [16], contributes a lot in these numbers. The other CubeSat missions belong to civil or military/defense government organizations [2], [17]. This statistics clearly indicates that CubeSats are highly demanded by different developers, from amateurs to governmental institutions, and can be used in a wide range of applications. It can be confidently asserted that, in the coming years CubeSats will continue to grow in number and their subsystems and missions are expected to be more intriguing and challenging.

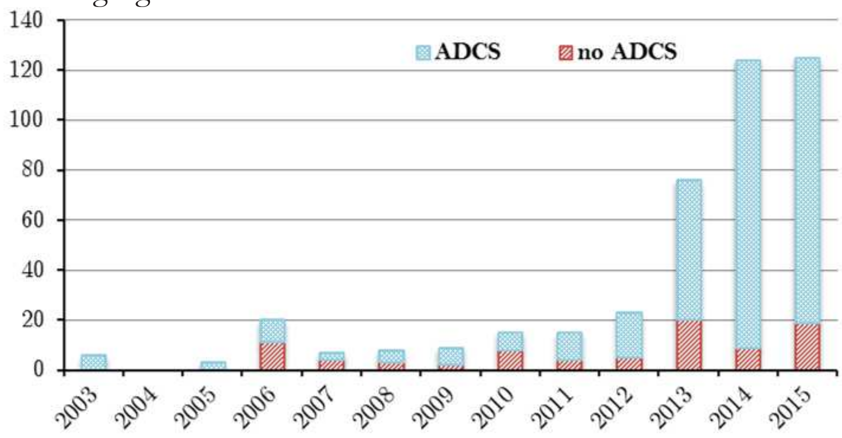

Figure 1.2-3 Number of CubeSat missions per year, considering presence of ADCS [2], [17]

However, not all CubeSat missions succeed. As shown in Figure 1.2-4, less than 50% of the launched satellites achieved their goals. The harmful factor, which strikes CubeSats massively and cannot be predicted or avoided by the developer, is a launch vehicle crash. As nanosatellites mainly launched in groups, one launch failure kills dozens of them. For 12 years of CubeSat development, almost 100 nanosatellites are lost because of only 4 launch failures.

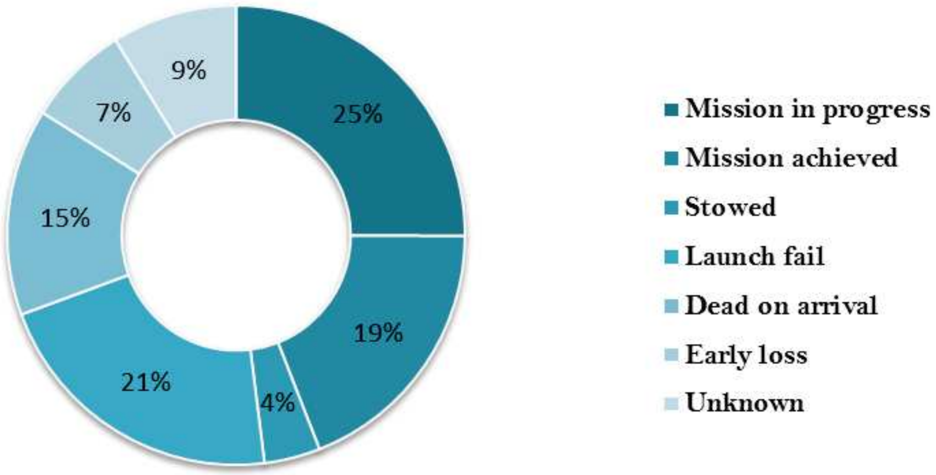

Figure 1.2-4 CubeSat mission status for 2003-1015 years [2]

The examination of the reasons that lead to mission failures after the deployment shows distribution of the subsystem malfunctions (Figure 1.2-5) [4]. It is easily seen, that almost half of failed CubeSats have never been contacted after launch. There are many causes that possibly lead to this end, and, unluckily, they cannot be identified due to specificities of the space missions. However, they can be estimated based on the statistics (Figure 1.2-5) or analyzing the examples of the CubeSats, which were semi-functional after deployment and reanimated lately. The leading positions through the recognized failure reasons belong to communication and power malfunctions. Though, they are not always caused by Telecommunication subsystem and EPS, because statistics represents reasons of satellite failure, but not the actual causes.

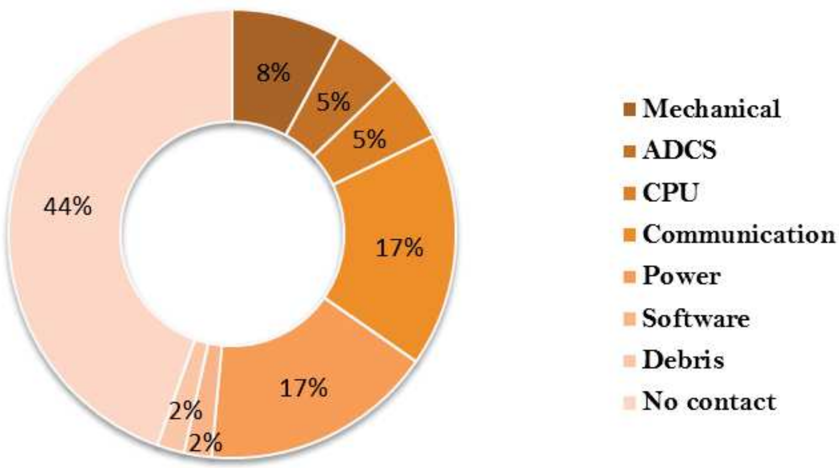

Figure 1.2-5 CubeSat Mission Failures for 2000-2012 years [4]

The most critical stage of the CubeSat on-orbit operation is its separation from the deployment container. As CubeSats are usually regarded as secondary payloads, the tip-off rates imparted on a CubeSat upon separation is weakly overseen [18]. Providers of the deployment system do not declare maximum tip-off rates that CubeSats may acquire during the separation from the container. While according to the study of the CubeSat separation dynamics [19] the theoretical tip-off rate does not exceed 45 °/s, based on experience, a CubeSat might get spinning up to 100 °/s [20] and, exceptionally, even higher. Moreover, since many CubeSats have ADCS with an extremely limited efficiency, the unexpectedly high-speed tumbling can be critical for them. Accordingly, when a CubeSat didn't succeed to recharge accumulator batteries or cannot properly communicate with a ground station, the possible cause is an incorrect satellite attitude due to the ADCS fault. Several examples well illustrate the significance of ADCS for the proper CubeSat on orbit operation and, therefore, for the CubeSat failure:

- SwissCube, the first Swiss satellite, launched in September 2009, acquired extremely high rotation around 200 °/s after separation that prevented from using its payload or trying to de-tumble by means of ADCS. It was decided to let SwissCube de-tumble "naturally", and in 14 months the rotation slowed down to 80 °/s, then ADCS could accomplish the stabilization. While the planned SwissCube lifetime was 4 month, all satellite systems were still able to work. In February 2011, SwissCube was fully controlled and still stays operational so far [21].
- AAUSAT3, the third Danish student-built CubeSat, launched in February 2013, experienced a spin velocity of almost 540 °/s due to both the separation rate and an incorrect feedback sign of one of the magnetic coils in ADCS. Fortunately, this bug was identified and fixed in a good timing and AAUSAT3 managed to de-tumble itself. It successfully operated until October 2014. Developers noted that if AAUSAT3 had reached 650 °/s, it would have been impossible to recover it [22].
- SamSat-218, the Russian CubeSat developed by the Samara State Aerospace University, was launched in April 2016. At the moment (May 2016) SamSat-218 does not communicate with ground stations, while some radio enthusiasts report hearing fragments of Morse code from the CubeSat. According to the developer's hypothesis, the high tip-off rate during the satellite deployment prevents SanSat-218 from successful communication with the ground [23], [24].

Indeed, ADCS is the system which ensures the safety of a CubeSat in the early stages of the on-orbit operation and supports its correct work later on. The statistics of CubeSats employing ADCS (Figure 1.2-3) shows that majority of launched missions carries on board ADCS components, but their complexity and performance vary widely: from a rough attitude measurement to a full-functional 3-axis control analogous to the systems used for larger satellites. Nonetheless, every year the proportion of nanosatellites with no attitude control declines, and the tendency of CubeSat missions leaves ADCS no option but to improve its performance. The current state of the art of ADCS technologies is given in the following section.

1.3 Overview of Attitude Determination and Control System (ADCS)

Any satellite mission is designed according to the needs of the payload, which requires certain orientation at definite time. However, the payload is not designed to change satellite orientation and an Attitude Determination and Control System (ADCS) is provided for this purpose. ADCS is a subsystem, which determines the satellite attitude using sensors and provides attitude control using actuators.

Satellite attitude is defined by the relationship between axes of the satellite and some reference frame, and usually described by yaw, pitch and roll angles. Depending on the mission objectives and used sensors, different reference frames (or all of them) can be employed for attitude determination [25], [26]:

- International Celestial Reference System (ICRS) has its origin at the center of mass (CoM) of the solar system. The z axis is aligned to the Earth's North Pole and the x axis with the vernal equinox. ICRS is the basis for fundamental measurements of the positions and motion of celestial bodies; it is used for interplanetary missions.
- Earth Centered Inertial (ECI) coordinate system has its origin at the geometric Earth center. The z axis is aligned to the Earth's North Pole and the x axis points towards the vernal equinox. Satellite orientation with respect to the ECI can be determined from stellar observation.
- Earth Centered Earth Fixed (ECEF) coordinate system rotates with the Earth, so its z axis is aligned to the Earth's North Pole and the x axis is pointed to the intersection between the prime meridian and the equator. Satellite orientation with respect to ECEF is required for ground communication tasks and for any Earth sensing mission.
- Orbit Fixed Coordinate System is fixed to the satellite body. Its z axis points directly away from Earth center (to nadir) and its x axis is tangent to the orbit trajectory. It is often used for Earth pointing satellites.

The ADCS is tightly coupled to other satellite subsystems and this makes it responsible for correct operation of the whole satellite (Figure 1.3-1). As it was mentioned in the previous section, number of malfunctions was caused by ADCS failures. For proper satellite operation, the ADCS has to perform the following tasks [25]:

- Provides satellite attitude knowledge;
- Provides rate stabilization and pointing for payload and other subsystems;
- Provides rate and attitude control, and station keeping maneuvers;

Depending on the mission objectives, different control techniques can be implemented by means of ADCS [25], [27]–[29].

When there is no need to rotate the satellite quickly and change its pointing, *passive control techniques* are used. They take advantage of basic physical principles: The control forces are generated by means of interaction between a satellite and the space environment.

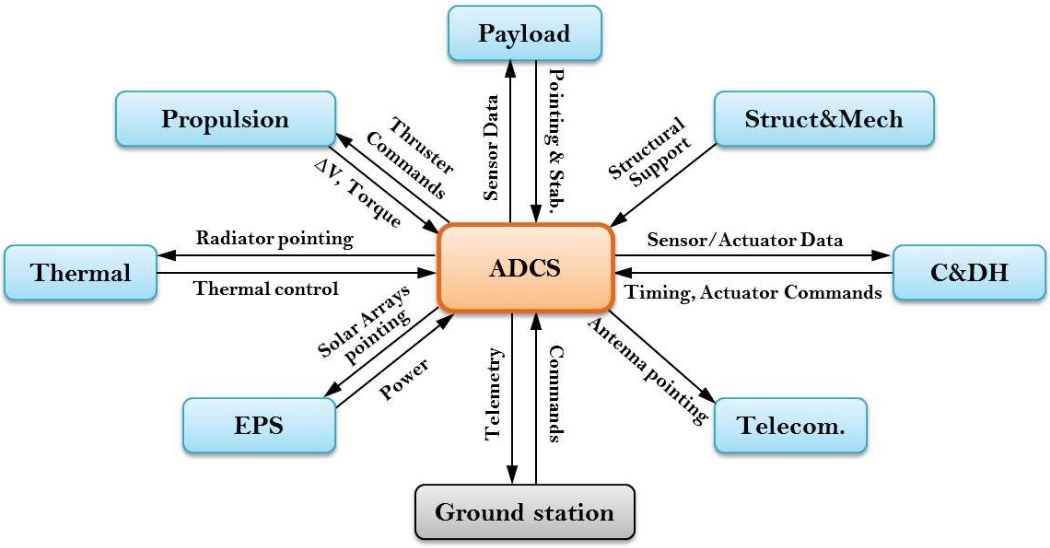

Figure 1.3-1 ADCS functional relationships

The gravity-gradient controlled satellites use the property of an elongated body in a gravity field to align its minimum inertia axis with the local vertical. Often a deployed boom is used to enlarge the inertia of two satellite axes and to accentuate the one, which it pointed to Earth's center. This technique is very helpful for satellites in Low Earth Orbit (LEO) without yaw orientation requirements.

Other type of passive ADCS employs a permanent magnet to make the satellite aligned in the Earth's magnetic field. This attitude control usually experiences some perturbations caused by variations of the Earth's magnetic field, though this technique is more reliable for near-equatorial orbits where the magnetic field stays almost stable.

The passive control techniques have very limited accuracy and provide only two-axis stabilization, when they are not combined together or with other methods.

Spin stabilization can also be considered as a passive control technique, because it relies on the gyroscopic stability, so that the satellite angular momentum vector is almost fixed in inertial space. A spin-stabilized satellite (or spinner) is stable if it is spinning about the largest inertia axis. The higher the stored momentum is, the less sensitive to disturbances the satellite is. Thus, when a spinner has to be reoriented, extra torque is required because of the gyroscopic stiffness. Another disadvantage is that a spinner must be actively controlled if has any cause of energy dissipation on board and to periodically adjust its attitude and spin rate.

Three-axis control technique is the most developed approach to satellite attitude control. It allows 3-axes stabilization as well as stable, agile and accurate maneuvers. And these capabilities require both sensors and actuators that make active ADCS more complex and expensive comparing to passive one. There are two sub-types of three-axis control: (i) Momentum bias systems are similar to the spin stabilization, with an exception that it employs a wheel (with its spin axis normal to the orbit plane) to provide gyroscopic stiffness. This wheel is also used to control attitude by slightly changing its speed. (ii) Zero-momentum systems rely on the actuators which keep a satellite stable responding to disturbances and provide required maneuvers (satisfying both rate and pointing constrains).

The selected control technique must respond to the needs of satellite mission: 2- or 3-axis control, accuracy of stabilization and pointing, reorientation speed. The ADCS hardware generally uses two types of components: sensors and actuators, whose classification and features are explained in the following sections.

1.3.1 Sensors

While actuators are not always included in the ADCS, as it was enlightened above, sensors are essential components of the ADCS. They ensure determination of the current satellite attitude with respect to the chosen coordinate system. The sensor technologies typically used for the satellite ADCS and their performance specifics are introduced below [9], [27]–[29].

Sun sensors measure two angles between their base and the direction to the sun. They range from detectors that find whether the Sun is in the field of view (FOV), to the fine instruments that can accurately determine its direction. They are light-weight and reliable, that makes them popular as part of the normal ADCS operation as well as part of initial acquisition or failure recovery system. However, being used on LEO, they inevitably experience the regular loss of data due to the eclipse periods, and this issue must be covered by redundant sensors of other type or by specific ADCS algorithms.

Star sensors are the most frequent choice for the mission where high accuracy of attitude determination is required. They determine the satellite orientation based on the association of the information about the starry sky in their FOV and the known star database. Star sensors are classified as star scanners and star trackers. *Star scanners* are designed to be used on a spinning satellite. The spin provides the scanning of the sky. After several crossing, the satellite's attitude can be derived by comparing the stars passed through FOV with a star directory. *Star trackers* are able to select, locate and track one stellar image to derive the attitude information. They are more accurate tool then scanners and commonly used on 3-axis stabilized satellites. Moreover, the preliminary stabilization of a satellite is often required, so that the star trackers get initial pointing. All star sensors are sensible to bright light and can be blinded by the Sun, Moon and bright planets or accidental reflections from mechanical parts of the satellite structure. To prevent ADCS from the loss of attitude information, the star sensors are usually paired with a complement sensor of another type.

Horizon sensors work in infrared light bandwidth and they are able to detect the contrasted border between the cold space and the heat of the Earth, so that the nadir direction can be determined. Horizon sensors can be *static* (or *starring*), which have a FOV large enough to view the entire Earth disk or a portion of the limb. The static horizon sensors measure errors in pitch and roll from a nominal satellite attitude; however, they cannot detect errors in yaw. The *scanning horizon sensors* have other principle of work: they have a narrow FOV and use a rotating mirror or lens to scan the horizon. Horizon sensors provide direct attitude knowledge relative to the Earth, but they tend to be less accurate then star trackers.

Magnetometers measure the direction and magnitude of the Earth's magnetic field and then compare them to the known data of the Earth's field that let them to determine the satellite's attitude. They are simple, reliable and lightweight, but their accuracy is not as good as that of star trackers or horizon sensors, because of possible shifts of the magnetic field and imprecisions of its known model.

Gyroscopes are inertial sensors and shall be combined with external sensors for the precise knowledge of satellite attitude in the external reference frame. Gyroscopes measure the speed or angle of rotation from an initial orientation. One gyro provides knowledge about one or two axes and, commonly, they are combined together to an *Inertial Reference Unit* for full three axes. Being complemented by accelerometers, they are called *Inertial Measurement Unit* (IMU). There are a number of technologies used to build gyros: spinning wheels, ring lasers, fiber optic wounds, vibrating structures (including hemispherical resonators) and those with MicroElectroMechanical Systems (MEMS). Every technology has its own pro and cons. For small satellites, MEMS gyros are very popular due to their low size and mass together with their competitive sensing capabilities.

There are also technologies for the satellite attitude determination using *GPS receivers* (requires a set of antennae), or other based on *radio frequency beacons*. However, they are not wide-spread nowadays, especially, for small satellites.

1.3.2 Actuators

Actuators are instruments to control the satellite attitude; they maintain required rate and support pointing and maneuvers. To this end, the torque shall be applied to the satellite to insure its rotation around an axis containing its CoM with a needed spin rate. Several technologies are used to provide this control torque [9], [27]–[29].

Reaction wheels are essentially torque motors with high-inertia rotor. A reaction wheel has a zero nominal speed and is able to rotate in either direction with speed up to several thousand revolutions per minute (rpm), by that it generates a torque to spin a satellite in an opposite direction around an axis aligned with the rotor axis. As reaction wheels have a saturation speed (maximum speed), their storage capability is limited by the maximum angular momentum capacity. After reaching this value, a reaction wheel must be dumped. This process induces an undesired satellite rotation, which must be compensated by means of other actuators. For 3-axis stabilized system, at least 3 wheels are required with their axes not aligned; one or more additional wheels are often used for redundancy.

Momentum wheels are similar to reaction wheels, but have a nominal speed above zero. Hence, they accommodate a nearly constant angular momentum that yields satellite gyroscopic stiffness along two axes. The control torque changes the momentum wheel speed within 10% of nominal value.

Control moment gyroscope is a device consisting of a rotor spinning at a constant speed and mounted in a motorized gimbal with one or few degrees of freedom (DoF). It uses the same principle that spinning wheel gyro sensors, but instead of measuring the gyroscopic torque, it generates this latter by applying a tilt to the rotation axis. Control moment gyroscopes are able to produce large torques about all three satellite axes, that makes them highly demanded for missions requiring agile maneuvers. Their disadvantages are large weight and complicated control law.

Magnetorquers produce a control torque by means of the interaction between the generated magnetic dipole momentum and the Earth's magnetic field. Magnetorquers are simple, light weight and quite efficient. They consist of a wire-wound coil and require only a magnetometer for field sensing. Magnetorquers are often used to desaturate reaction wheels or for the missions with not very exigent requirements to attitude control and strict mass constraints.

Thrusters are able to produce both a control torque and a delta-v (change in velocity) by expelling mass. While there are various types of thrusts, only hot-gas and cold-gas engines found their application in the ADCS. Most of well-tried thrusters for ADCS feature a high control torque and relatively large propellant mass required to be stored on board. Thus, large satellites benefit from provided torque and deal with required mass constrains, but for the fine attitude control of small satellite, these features turn into some difficulties. However, propulsion technologies rapidly evolve and get adapted for smaller satellites.

1.3.3 Specificities of CubeSat ADCS

ADCS design depends on the mission needs. As CubeSats tend to be analogue to larger satellites and fulfill the same in-orbit operations, their attitude control system must be capable of the same level of performance. CubeSat ADCS inherits all principles and features from the one of large satellites. The passive and active ADCS are equally used in nanosatellite missions. They comprise similar selection of the sensors and actuators (with capabilities scaled to CubeSat needs) with the only difference of tightly constrained volume and mass budget.

Due to recent progress in microelectronics and overall miniaturization of electric and mechanical components, satellite hardware is getting smaller in size, so that it can fit nanosatellites with minimum performance degradation. However, CubeSat construction process is often constrained by rapid timescale and strict budget that leads to extensive use of low cost and COTS technologies for every subsystem, including ADCS. Rapid development of the technologies means that most of CubeSat state-of-the-art components have little or no flight heritage. That poses a question - how these components will operate in space if they never flown before? [28]

The verification of a component or a whole satellite is dedicated to answer this question. Requirements to the space product verification process are designated by the standards (developed by different institutions for various purposes), which have several distinctions. The satellite verification process and its adaptation to nanosatellites are discussed in the following section, where also the classification of the required pre-launch tests is given.

1.4 CubeSat ground tests philosophy

The verification process aims to demonstrate that the space product meets the specified requirements and is capable of sustaining its operational role. The verification shall be accomplished for both software and hardware by at least one of the following methods [30]:

- Test;
- Analysis;
- Review of design;
- Inspection.

All safety critical functions shall be verified by test. This leads to the necessity of ground tests, which have objective to demonstrate the satellite (and its components) operability while being placed in the conditions closed to those the satellite experiences during the preparation to launch, the launch and in-orbit operation.

The tests requirements for satellites and space systems are specified by a number of standards, which are asserted by different institutions. In [31], the most widely used standards, which are ECSS-E-ST-10-03C [30], ISO-15864 [32], NASA-STD-7002A [33], GSFC-STD-7000 [34], JERG-2-002 [35] and SMC-S-016 [36] are studied and compared. The study shows that the standards differ and reflect the test philosophy of the corresponding countries and institutions. Some tests mentioned in one standard are not listed in another one. Moreover, these test requirements are tailored for large satellites and space systems and some of them are excessive for low-cost and short timescale nanosatellites. Often CubeSat developers skip some essential for large satellite tests and tend to fulfil the minimum requirements specified only by the user manual of the launchers. Small organizations, like schools or universities, hardly have access to specialized testing facilities or underestimate the necessity of comprehensive ground tests [31]. Other reasons of insufficient CubeSat verification are time limits and lack of experience of novice satellite developers that force them to miss some verification steps in order to fit timing [4]. All these situations lead to high risk of a malfunction at early stages of in-orbit CubeSat operation and cause sad but true statistics of failures, mentioned in the previous section.

Trying to adapt the existing standards of satellite test requirement to needs and constraints of the nanosatellites, a new ISO standard is about to be established by joined efforts of several Japanese organizations [31], [37]. It intends to provide a guideline to test and verification process in order to help new comers to CubeSat development.

Besides the details and particularities of every standard, three categories of essential satellite tests can be distinguished: environmental, electrical and functional. This classification reflects the nature of the possible satellite malfunction causes and differs from that used in some standards.

1.4.1 Environmental tests

Environmental tests are intended to demonstrate how a space system or its components survive in the conditions of the pre-launch, launch and in-orbit environment. On the pre-launch stage, a space product experiences effects caused by transportation and storage means: vibration, shock and climate (including temperature, pressure and humidity). During the launch phase, the following effects take place: acoustics, static load, vibration and mechanical shocks. Orbit stage features thermal, vacuum and radiation effects. To prove that the space segment equipment withstand the foregoing environmental effects, the corresponding tests shall be performed:

- Random vibration test
- Sinusoidal vibration test
- Shock test
- Acoustic test

Figure 1.4-1 LituanicaSAT-2 is being installed in the thermal vacuum chamber

- Thermal vacuum test (might be replaced by the thermal ambient test for components which operate in non-vacuum environment during their entire lifetime)

Exceptionally, for some space equipment, several additional tests might be performed, if they are critical for products operation due to some particularities of design or operation and transportation environment:

- Acceleration tests
- Proof pressure test
- Pressure cycling test
- Humidity test
- Radiation test

The levels of environmental loads are identified prior to the testing and they must be concerned with one of the standards of space environment (for example [38]) and with the user manual of the selected launch vehicle.

1.4.2 Electrical tests

Within electrical tests, a space product shall demonstrate the electromagnetic compatibility of its components and systems, as well as fulfillment of the general electric system requirements. There are several key aspects to be verified:

- Electromagnetic compatibility
- Magnetic field emission and magnetic moment
- Electrostatic discharge
- Passive intermodulation test
- Multipaction test
- Corona and arc discharge test

The electrical tests are intended to prove the correct operation of electrical connections and interfaces, while correctness of the logical interface responses is verified within functional tests.

1.4.3 Functional tests

Functional tests verify the complete function of the space system or component in all operational modes. They include demonstration of both mechanical and logical operations. Functional tests shall be performed before and after environmental tests to ensure that the space equipment survived and maintained its functionality.

Functional tests must be implemented on different levels of satellite integrity. *Component-level* tests demonstrate complete performance of one component according to its functional requirements. They prove that a component is ready to be integrated in the system. *System-level* functional tests verify correct operation of the whole system or an assembled satellite. They are required to prove that the satellite is ready to implement its mission.

As some satellite components and systems require particular conditions to operate that might be hardly achieved at ground environment, functional tests are complex tasks. Thus, there are different principles to check the space equipment performance fractionally or completely.

The *software-in-the-loop* (SIL) approach is dedicated to verify the component or system functionality by replacing one or several physical elements with mathematical models, which represent their behavior and functions, while using real software. This approach is very useful for design verification on early stages and for software functional tests. In some cases, well organized SIL simulations can prove performance of the whole system.

The *hardware-in-the-loop* (HIL) technique is implemented on the real hardware and software and may include electrical simulations of system dynamics, environment or external effects. This is the most capable approach for effective functional tests, because it allows verification of the entire complex of the hardware and software.

1.4.4 CubeSat testing scenario

The methodology of space product testing is illustrated using an example of a hypothetical CubeSat (system) and its star tracker (component).

The scenario of testing procedure is similar for components and systems, it is organized as follows:

- functional tests
- environmental tests
- electrical tests
- functional tests

It shall be noted that the basic functional tests are recommended to be executed at each milestone of the system assembling and verification.

At early stages of development, the star tracker passes many SIL tests in order, at first, to verify choice of elements to be used, and then, to debug and verify flight software. Once hardware of the star tracker is done, the functional tests shall be performed. To this end, HIL test is organized using the star tracker hardware and running its flight software, while the starry sky is emulated by means of a simulator, projecting certain area of the sky. Thus, dynamics of the star tracker (its motion together with a satellite in orbit) is simulated by varying the projected area of the starry sky and the real star light emission is replaced by the simulator.

Then, in order to be verified and validated for space application, the star tracker passes environmental and electrical tests as they are established by the selected standard. Once these tests are successfully accomplished, the performance of the tested product is checked again to prove that environmental loads did not perturb its functions. At the end of the testing program, the star tracker is considered as validated, if it succeeded at all steps of verification.

After being installed onboard of the CudeSat, the star tracker becomes an element of ADCS. At the stage of CubeSat functional tests, every sub-system of the satellite is checked separately and together with related sub-systems. Then, environmental and electrical tests are performed for the satellite according to the selected standard. At the end of the testing procedure, whether or not the CubeSat is ready for launch is decided.

1.5 ADCS HIL TEST FACILITIES

Within the framework of ADCS functional tests, SIL or HIL simulations can be performed depending on the available facilities [39]–[41]. SIL approach to the ADCS test proves software performance and relies on faithful functionality of every component and their correct coupling. HIL mode is more appropriate to verify ADCS performance and it is more difficult to be realized, because of the nature of ADCS components: (i) actuators are intended to move the whole satellite and their efficiency depends on CubeSat dynamic parameters, its dynamics and certain environmental effects (magnetic field, gravity gradient); (ii) sensors require environmental effects as those in orbit (magnetic field, sun and starry sky or Earth radiation); (iii) implemented algorithms are tightly coupled with hardware response and, consequently, with CubeSat dynamics, (iv) sizing and collocation of ADCS component matter. Thus, HIL technique gives better overview of ADCS performance. Different approaches to the organization of HIL ADCS testing and corresponding facilities are discussed in this section.

The main purpose of the facilities supporting ADCS HIL tests is to simulate environment close to that in orbit. It means that the low-torque environment, faithful representation of magnetic field and starry sky and sun simulation must be provided. Selection of functions for an ADCS testing facility depends on the employed sensors and control system capabilities. However, having the minimal-torque environment is an essential requirement.

1.5.1 Sun and starry sky simulators

For sun simulation, a light source is typically used, its relative orientation to the sun sensor is adjusted and constantly altered to emulate orbital motion. The most low-tech sun simulators can be made of a correctly sized lamp, which provides a reasonable simulation level for low cost photodiode sun sensors [42]. The most advanced simulators include precisely calibrated light sources and specific optical systems. That organization of the simulator allows imitation of various characteristics of the natural sun light, such as typical intensity, spectrum and collimated light beam.

Starry sky simulation is a more challenging task, as the latest generations of star trackers feature widened range of functionality, which should be achieved via advanced complex of hardware and software routines. Star tracker is an accurately tuned instrument, its optics is designed to operate with an image at infinite distance from the sensor and it is very sensitive to any deviations of the light source characteristics or a focus change. As a result, the testing procedure and corresponding setup required both for calibration and performance assessment of the novel algorithms and hardware, are very demanding. There are several known techniques for the starry sky simulation:

- Outdoor procedure, typically at remote sites. Common disadvantages of this approach are appearance of atmospheric effects (light absorption, background light, retraction and scintillation) and time constrains [43];
- Tests at astronomical observatories, which provide appropriate conditions for long-term experiments and take advantages of a telescope tracking system to keep a fixed inertial pointing [44]. However, these tests lack realistic simulation of the stars light characteristics;
- Projection of the stars on the LCD monitor. Using the star catalog, number of the preselected brightest stars is made into a two-dimensional star field and imaged on a monitor. This kind of simulator can be fixed [45] or moving [46];
- Optical head with a collimator and independent control. This kind of simulators is mounted directly on the star tracker optics and gives the most advanced simulated image of the sky, including such characteristics of the stars as intensity, color and collimated light [47] (Figure 1.5-1, left);
- Combination of the previous two methods, which comprises an LCD monitor and separated collimated optics, for instance, the starry sky simulators presented in [44] and [48] (Figure 1.5-1, right).

It shall be noted that the first two techniques in the list above are difficult to be adapted for the system-level ADCS HIL tests and they are mainly used for calibration and evaluation of the star tracker during the development phase. The other three approaches are applicable to both component- and system-level tests.

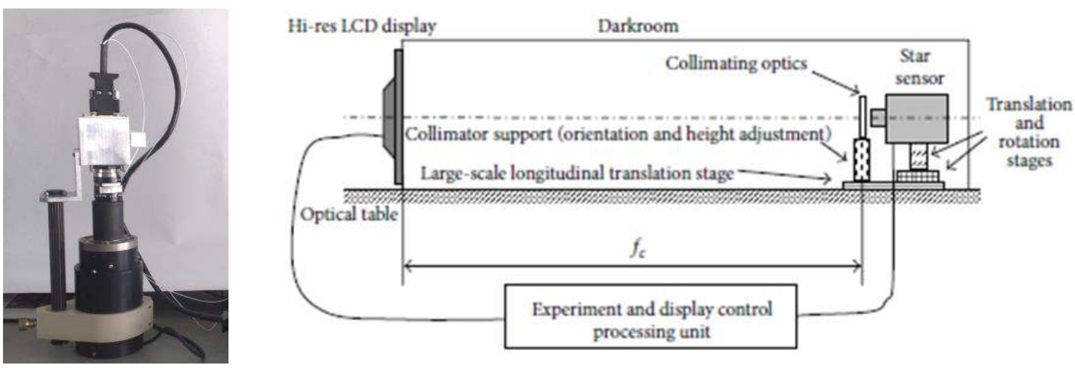

Figure 1.5-1 Optical head for starry sky simulation with the star tracker camera mounted [47] (left); Scheme of the starry sky simulating facility with the LCD monitor and collimating optics [44] (right)

1.5.2 Helmholtz cage

A Helmholtz coil is a device often used for calibration, characterization and testing of space systems. It consists of two solenoid electromagnets placed symmetrically along a common axis. Helmholtz coils were first suggested for generation of uniform magnetic field in 1926 [49] and latter this technique was widely implemented in the space product testing and instruments calibration [50], [51], since homogeneous magnetic field has critical significance for space magnetometers and magnetorquers evaluation.

The principle of Helmholtz coils is based on the fact that two wire loops carrying a current create a magnetic field in the volume between them. This field had a single dominant direction and nearly constant magnitude, which depends on the current and number of the wire loops and their dimensions. Thus, a set of two Helmholtz coils generates a controllable magnetic field in the direction of their common axis. In order to completely control a magnetic field within a certain volume, at least 3 pairs of coils are required. Such assembly is called Helmholtz cage. The Helmholtz cage can be built up of the circular or square coils. Though being of comparable dimensions, square coils are able to produce larger region of the homogeneous field then circular coils [52], but the first ones need to have more wire loops to produce same magnetic flux density.


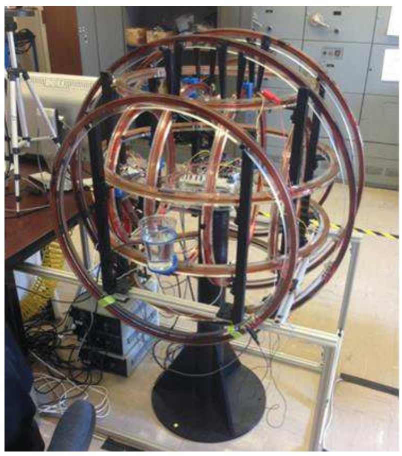

Figure 1.5-2 Helmholtz cages designed at Delft University of technology [53] (left) and at UC Berkeley [54] (right)

With an explosion of the number of CubeSats developments, the Helmholtz cage was rapidly adapted for nanosatellite ground tests. The cage, capable to accommodate up to 6U CubeSat with all deployable elements, has reasonable dimensions (around 2 m side) and is feasible to be assembled even at university facilities. There are several examples of Helmholtz cages developed for micro- and nanosatellites [46], [53]–[58], which were published or proposed as off-the-shelf product.

1.5.3 Overview of low-torque environment simulations

Simulating the functional space environment is required for ADCS HIL tests, and the key problem is minimizing torques, which perturb the satellite during the tests. Two unique features of the space environment relevant to ADCS performance are the absence of gravity torques and the elimination of frictional resisting torques due to near vacuum conditions.

There is no method to create microgravity environment in the laboratory facility, but the virtual absence of gravity effects and friction can be simulated by several fundamentally different techniques, which were developed since the dawn of the Space Age. Backstory of the low-torque environment simulations is tightly coupled with the history of space technologies development. The most satisfactory and widespread way to simulate near space environment for ADCS is by the use of the *air bearing supported platform*. The first such platform appeared in the open documentary is constructed at NASA Ames Research Center and dated back to 1959 [59]. This platform is probably one of the first systems assigned for simulation of low-torque environment. Since that and until nowadays, a number of air bearing supported simulators was developed. However, air bearing platforms is only one of the possibilities. Some other techniques may be more efficient or feasible depending on the situation.

The astronaut's and cosmonaut's preparation program necessarily involves training in a *neutral buoyancy pool*. The microgravity is imitated by the accurate weighting of the pressure suits and space vehicle mockups until they are neutrally buoyant. An additional effort is required to keep the human or structure CoM and the center of pressure coincident, so that neither the gravity force nor the force of buoyancy yields a torque. More frequently, the neutral buoyancy facilities are used to train the operating sequences required for the Extravehicular activity (EVA) in most realistic environment. Evaluation of the large spacecrafts ADCS was also performed in the pools. Some ADCS components must be modified before their operation in the pool. For instance, thrusters are replaced by screw propellers in order to keep their functions in the underwater environment. However, operation in the pool doesn't solve the problem of friction torques. On the contrary, underwater environment yields magnified friction that must be considered in the test planning: In case of small satellites, the friction torques and actuator torques can be of the same order of magnitude.

For some kinds of space oriented experiments and instrument testing, *the parabolic flight* is a suitable option. The parabolic (or zero G) flight is carried out by an aircraft in order to achieve a brief period of near-weightless environment (around 20 sec) between alternates ascent and descent maneuvers. During this period all objects onboard of the aircraft experience free fall. This means the only force acting on objects is gravity and it does not induce any torques. The zero G flights are often used to introduce future space travelers to the real microgravity environment. For long-term experimentation, this technique of the reduced gravity simulation can be hardly applied, while it is modestly suitable for short-term ADCS verification tests.

Gravity offload systems are designed to simulate reduced or microgravity for humans and large deployable structures. Such systems use counter-weights or actively offload a portion of a weight by using the steel cables attached to several points of the payload. Thus, the gravity force is compensated by the applied tension force. The state-of-the-art gravity offload systems allow large displacements of the payload along three axes [60], [61], and the functional tests of large or deployable structures (solar panels) take advantages of it. For the ADCS HIL tests, the rotational freedom is most pertinent, thus this kind of low-torque environment simulators are not often applicable.

Figure 1.5-3 KnightCube (University of Central Florida) ADCS testing in microgravity conditions during the parabolic flight

The low-cost and easy-to-do variation of the gravity offload is a *string suspension.* One end of the string is connected to the payload (such way to avoid the gravity pendulum effect) and other end is fixed to the elevated base through a low-friction joint [62]–[64]. While the string suspension allows low-torque motion around one axis only, this approach is quite popular for micro- and nanosatellites ADCS HIL tests due to accessibility and low cost of this method.

Another way to deal with undesired torques is a *magnetic suspension* or magnetic levitation. It features nearly frictionless motion, but provides only one rotational axis [65] and has some other constrains caused by the nature of magnetic levitation phenomena: strong magnetic perturbations, unstable static force and damping when a payload accelerates.

Figure 1.5-4 CubeSat mockup with ADCS components suspended on a string inside Helmholtz coils [64]

1.5.4 Air bearing platforms

The air bearing platforms are highly demanded for low-torque environment simulations due to nearly frictionless motion and the potential to provide up to 3 rotational DoF. While different types of air bearings exist, they all use one operational principle: The pressurized air flow blows through a number of small orifice in the grounded part of the air bearing (active part) that provides a thin air film which supports the weight of the floating part (passive part) without contact between surfaces. Indeed, the air film is an effective lubricant and creates very small friction forces. Thus, there are two significant forces acting in the air bearing system: the gravity force and the upward force induced by the air bearing. They have equal magnitudes, so that payload is "offloaded". However, in order to simulate microgravity, the gravity torque must be minimized also. To this end, the air bearing platforms permit sensitive balance to bring the CoM close to the center of rotation (CoR) and diminish the pendulum effect caused by the gravity force. There are three types of air bearing platform design, which enable various payload movements and feature different number of DoF. Overview of these types of platforms with some representative examples of their application is given in following sections.

1.5.4.1 Planar systems

The planar air bearing platforms allow 2 DoF linear motion and 1 rotational DoF (2T-1R) around a vertical axis. Because of planar motion, these platforms do not experience perturbation torques from gravity, thus, they do not need weight balancing. The planar systems usually carry their own air supply and create an air cushion that permits nearly frictionless sliding motion on a polished surface. These systems are typically used to demonstrate docking and rendezvous maneuvers, to check ADCS performance for formation flying or to test foldable structures and space robotic arms. Despite the fact that only vertical spin is available, the relative motion of two or more satellites can be considered as a favorable feature of this kind of systems that enables evaluation both ADCS and GNC.

One of the examples of the planar air bearing systems for formation-flight experimentation is The Synchronized Position Hold Engage Re-orient Experimental Satellites (SPHERES) project developed by students from the Massachusetts Institute of Technology (MIT). SPHERES aims to evaluate the dynamics of a multiple satellite systems. It was designed specifically for operations in the ISS to enable demonstration in a 6 DoF microgravity environment [66]. In order to develop and verify algorithms, first tests were conducted at MIT facilities, which allow 2 DoF experiment on planar air bearing platform (Figure 1.5-5). The SPHERES satellites were mounted on the air carriage mobility system consisting a series of air bearing active parts and gas tanks providing an air cushion [67]. Using cold gas thrusters, satellites are able to perform multi-satellite proximity, docking and undocking maneuvers.

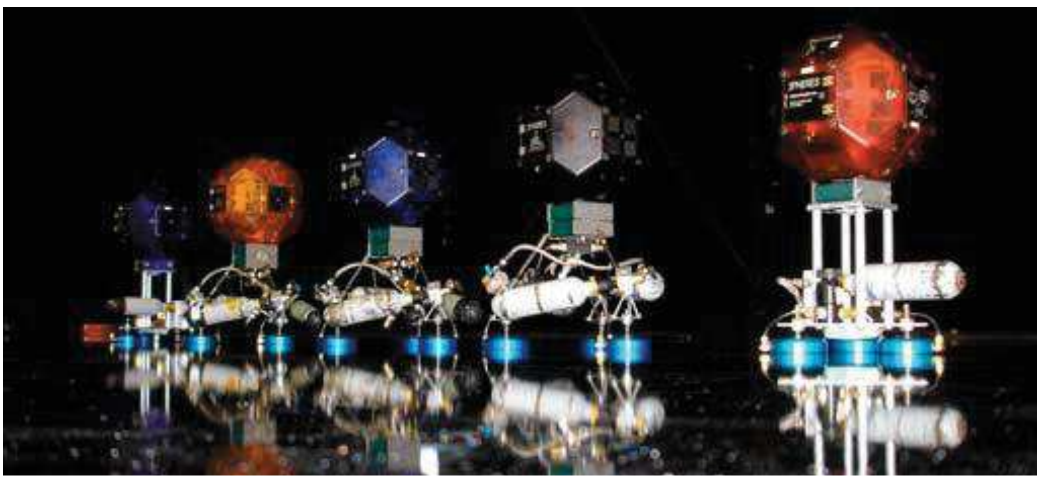

Figure 1.5-5 Five satellite maneuvers, SPHERES projects [66]

There are several other project that involve the ground demonstration of formation flying using bearing planar platforms: The robotic camera AERCam was intended to provide external inspection of the space shuttle and ISS without requiring EVA [68]; Demonstration of the GPS-based relative position and attitude sensing system, developed by Stanford University, involved a formation of three free-flying vehicles on a 3.6 x 2.7m granite table [69]; The prototype of free-flying telerobot, developed by joint effort of three Japanese corporations to replace EVA, demonstrated its performance flying over a flat testbed on an air cushion [70]; The autonomous docking testbed developed by the Naval Postgraduate School Space Robotics Laboratory performed approach and docking operations of two vehicles floating over a smooth epoxy floor [71], The Tokyo Institute of technology investigated a problem of capturing a damaged satellite with a 7 DoF arm, using a target satellite free-floating on the air bearing table [72].

Another branch of the planar air bearing platforms application is to demonstrate space robotic manipulator performances. Usually this task requires simulation of almost frictionless motion in one plane. For large robotic arms with elongated links, offloading of each link separately is recommended, so that gravity torque does not affect joints.

The air bearing tables are used in such experiments for motion simulation of both the robotic arm and target object. Researchers at the MIT field and Space Robotic Laboratory studied the control of a free-flying multi-robot team assembling a flexible space structure [73]. The air bearing platform was used to demonstrate transportation and manipulation different shape flexible objects by means of two two-arm robots.

Figure 1.5-6 Two autonomous robots manipulate a zig-zag flexible element on a air bearing table [73]

The University of Victoria performed an experiment with a planar air bearing that host a single robotic manipulator. Obtained results were used to prove the trajectory optimization for reducing vibration excitation of flexible manipulators during point-to-point motion [74].

Summarizing all aforecited examples it can be seen that planar air bearing platforms are often used in experimentation, where translational motion is required. However, within the scope of the ADCS HIL testing, the capabilities of such platform are constrained by 1 DoF of rotational motion. Thus, similar performance can be achieved by means of a low-cost approach using a string suspension.

1.5.4.2 Rotational systems

All existing rotational air bearing platforms have geometrical restrictions, which limit their angular motion. Thus, platforms can be categorized into 3 groups based on their configurations as shown in Figure 1.5-7: (i) tabletop; (ii) umbrella and (iii) dumbbell systems [75]. All air bearing platforms provide full freedom of spin in the yaw axis. The tabletop and umbrella systems have pitch and roll motions constrained to less than a half-turn. The payload plate of the tabletop system is usually mounted directly on the hemispherical passive part of the air bearing that yields limitation of pitch and roll motion to ±45°. The umbrella system comprises an extension rod connecting the payload plate and the near fully spherical bearing. This allows widening of the motion range up to ±90°. However, because the extension rod elevates the payload over CoR, additional efforts are required to ensure mass balance in the umbrella system. The dumbbell system features unconstrained motion in both yaw and roll axes. The roll axis is defined by the extension rods and orthogonal to the payload plates. While the dumbbell configuration greatly reduces geometrical interference of the rotating and the grounded elements, it causes some inconveniences: the payload must be separated into two parts and installed on the mounting plates perpendicular to the gravity vector, or balanced by an additional weight on second plate. This particularity of the dumbbell systems complicates their application for tests of assembled satellites, but they perfectly fit evaluations of distributed satellite avionics. Moreover, two unconstrained axes give great perspectives for nonlinear rotational dynamics study.

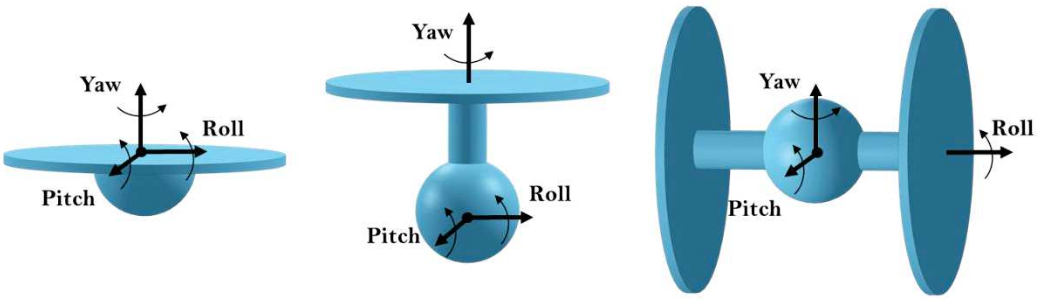

Figure 1.5-7 Tabletop, umbrella and dumbbell system configurations

The rotational air bearing platforms have the largest heritage in ADCS tests, as the first such system is dated 1959. This tabletop platform supported by 127 mm spherical air bearing involves an optical sensor and a set of reaction wheels (Figure 1.5-8). The experimentation was intended for the attitude control study: sensor measures an error when the platform drifts from a desired orientation and reaction wheels make required corrections. Citied in 1965 by G.A. Smith [59], this platform is described as "very simple compared to the present state of the art", that marks an explosive character of the air bearing systems development in the 60s. Indeed, dozen other air bearing test facilities developed in early 60s are presented in Smith's paper. One of the most remarkable systems is developed by the Grumman Aircraft Engineering Corp.: The tabletop air bearing platform is enclosed in a 6.7m spherical low-pressure chamber, which also accommodate three pairs of Helmholtz coils and 5 collimators for star tracker study. This system was designed to incorporate the Orbiting Astronomical Observatory (approx. 1600kg) and evaluate its ADCS [76].

An impressive freedom of rotational motion was achieved by researchers at Marshall Space Flight Center of NASA with the umbrella-type air bearing table constructed in 1960: it permits ±120°attitude change in roll and pitch and unlimited spin in yaw [77]. This table supported by 254 mm air bearing and able to hold up to 400 kg of payload was used for an experimental study of the effects of bearing imperfections on perturbation torques, and later for evaluation of control methods for the weather satellite NIMBUS [75]. Such freedom of the air bearing platform motion is quite challenging even for modern state-of-the-art systems. Some other examples of the rotational air bearing test platforms developed at early years of the Space Age are described in Smith's paper and [78]. However, in later decades and until now, development of the air beating tables did not come to the end. The designed systems continuously evolve to meet requirements of new satellite generations. The early developed air bearing platforms were common in use at governmental and industry facilities, they were large enough to accommodate payload mass up to several tons and even simulators of the manned space vehicles with a crew members [79]. More recent rotational air bearing platforms are capable of supporting much lighter payloads, responding to a tendency towards the satellite miniaturization. They become accessible at universities and small independent laboratories. The first known spherical air bearing table developed by an university was made at Stanford University in 1975 and used for CoM estimation applied to a drag-free satellites [80].

The Spacecraft Attitude Dynamics and Control Laboratory at the Naval Postgraduate School (NPS), having large background in the attitude control of spacecrafts since 1989, developed its first air bearing platform in 1995 in cooperation with Guidance Dynamics Corporation (GDC). The Satellite Attitude Dynamics Simulator (SADS) is a tabletop system, which has a total mass of 200 kg and includes components required for ADCS HIL study: a magnetometer, three gyros, a sun sensor, three reaction wheels, 8 cold gas thrusters and attitude control processor [81]. This system features full freedom in yaw and constrained to ±45° spin in pitch and roll. In later years, NPS developed two other tabletop air bearing platforms for 200 kg and 800 kg payload with tilt ranges limited to ±30° and ±20° respectively and with an auto-mass balancing technique [82], [83].

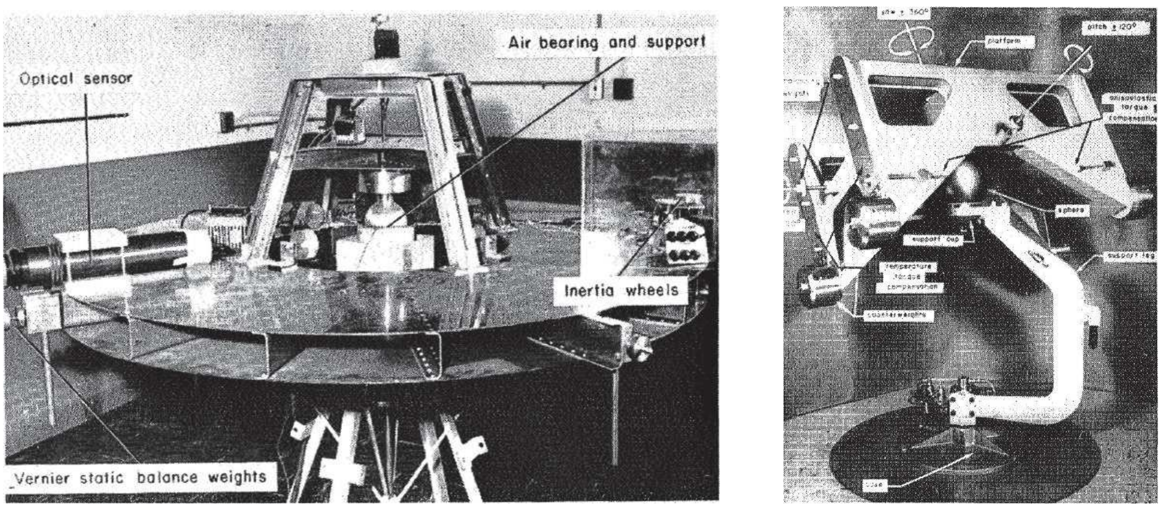

Figure 1.5-8 NASA Ames Research Center tabletop air bearing platform, dated 1959 (left) and Marshall Space Flight Center umbrella platform, dated 1960 (right) [56]

A three-axis air bearing based platform for small satellites was developed by combined efforts of four Mexican universities [84]. This platform is supported by an in-house manufactured air bearing with a nominal load of 80 kg and it comprises a set of ADCS sensors (IMU, magnetometer, sun sensor and four Earth sensors), three reaction wheels, two magnetorquers, on-board computer and wireless system for communication and monitoring. The platform is capable of unlimited spin in yaw and ±50° tilt in the other two axes, also the auto-mass balancing system is integrated in the platform and was tested.

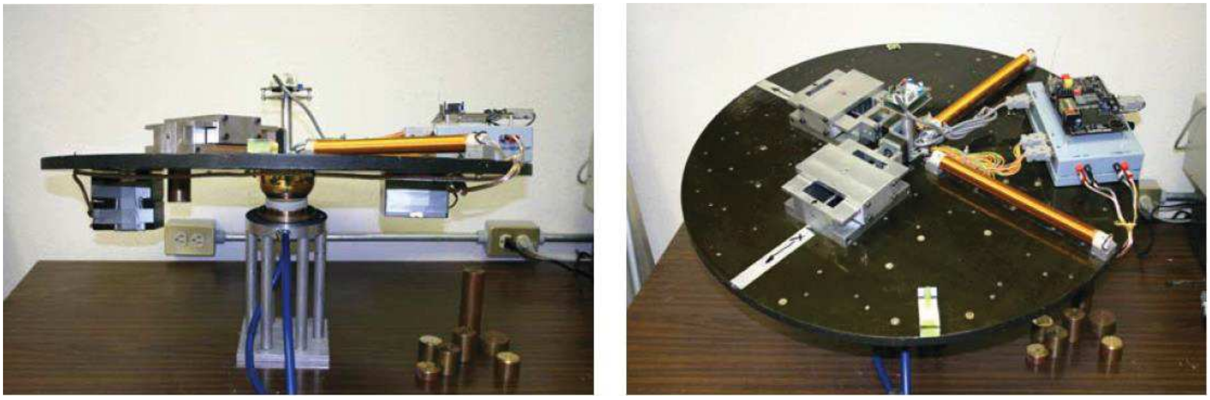

Figure 1.5-9 A three-axis air bearing based platform for small satellites [84]

While most developed rotational air bearing tables belong to the tabletop configuration, there are several examples of dumbbell systems. In the 80s, such type of air bearing simulators were used within the Army Lightweight ExoAtmospheric Projectile (LEAP) program to perform ground tests of kinetic energy kill vehicle avionics, particularly, demonstration of light weight technologies for interceptors [85]. These platforms were desirable because of their capability to support high accelerations and velocities over large angular motion [81]. In the 90s, dumbbell air bearing systems were developed by the University of Michigan and the U.S. Air Force Institute of Technology (together with Space Electronics, Inc.) for satellite attitude control study.

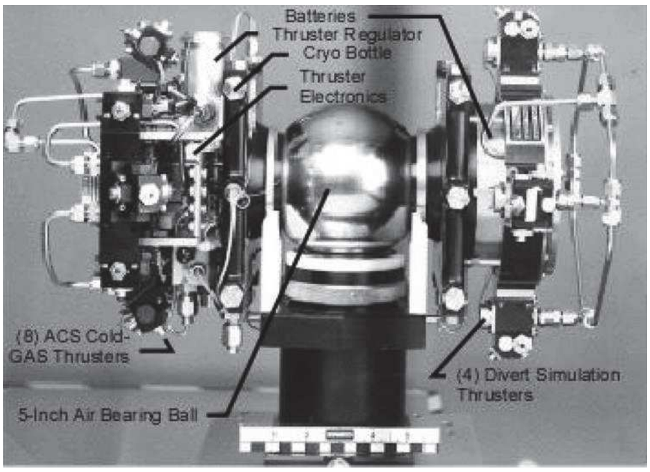

Figure 1.5-10 Dumbbell air bearing testbed for Army Lightweight ExoAtmospheric Projectile [81]

It is easy to see that the majority of rotational air bearing systems has strict limitations of motion, and additional efforts are required to slightly extend the range of possible rotation angles. The University of California and Jet Propulsion Laboratory constructed a system able to provide even more freedom than the dumbbell. It consists of three whole spheres floating of their own air bearings. Each sphere accommodates components of the communication and monitoring systems required for the experiment and a flywheel with a motor to control angular orientation and velocity of the sphere. The experimentation is aimed to study control rules for the synchronized continuous rotation of multiple spacecrafts. While such air-levitated sphere is potentially able to provide unconstrained rotation about all axes, the sphere used in the experiment performs only single-axis rotation due to using of single flywheel.

Figure 1.5-11 The synchronized rotation experiment setup and the interior the air-levitated sphere [86]

The systems described above do not complete a comprehensive list of rotational air bearing platforms. However, they are the most representative examples of such platforms, which were selected to illustrate the history and evaluation of air bearing testbeds. More systems are described in Smith's paper [59], Schwartz' Historical Review of Air-Bearing Spacecraft Simulators [75] and in [83].

1.5.4.3 Combination systems

The combination systems incorporate the capabilities of both planar and rotational air bearing platforms. They typically allow 5 or 6 DoF and comprise combination of translation and attitude stages. Such systems are used as extension of the planar tables and applied for similar tasks: demonstration of some aspects of formation flying and testing of rendezvous and docking maneuvers.

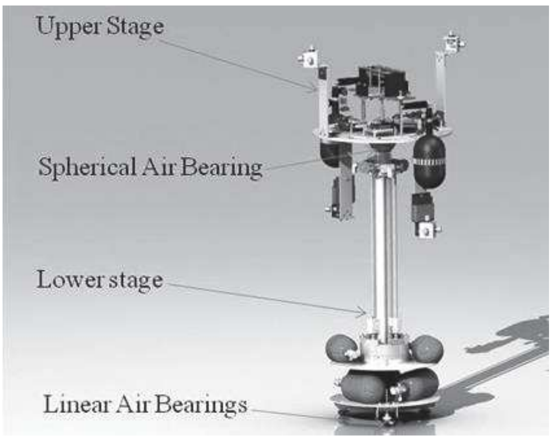

Figure 1.5-12 Rensselaer Polytechnic Institute 6 DoF platform [87]

The Rensselaer Polytechnic Institute designed and implemented a 6 DoF platform: 3 translational DoF provided by floating over the air bearing table and elevating the attitude stage along a vertical axis by means of an air bearing pulley; the attitude stage supported by a spherical air bearing and allows ±360° in yaw axis and ±45° in pitch and roll axes [87]. This system is supposed to be used for testing GNC control algorithms and, being supplemented with a second 6 DoF platform, for the formation flying and maneuvers evaluations.

Some other combination systems were developed by the Marshall Space Flight Center's Flight Robotics Laboratory [88], Georgia institute of Technology [89], NASA Jet Propulsion Laboratory [90] and Research Center of Pneumatics at Harbin Institute of Technology [91].

1.6 Air bearing platforms for CubeSat ADCS tests

Over the past decades the satellite technologies follow a course towards miniaturization due to the continuous advancement of electronic and mechanical components. The air bearing ADCS test facilities, being developed in parallel with satellites, also reflect this tendency: newly built platforms are designed to have a lower load capacity compared to systems from 60s. This drift to light-weight platforms is explained by their nature. For faithful experimentation, the platform must permit a minimal addition to the satellite dynamic parameters if the system allows testing of an assembled satellite or an accurate representation of satellite inertia and mass distribution if the system is designed for detached ADCS components. Indeed, ADCS actuators are able to demonstrate efficient operation only for satellites with mass properties within a predefined range. For example, an actuator intended for 500 kg satellites is not capable of performing effective attitude control of a 1000 kg spacecraft, and also it does not provide enough accuracy to the 100 kg satellite maneuvers. This is well illustrated by examples given in Table 1, which shows the main performance characteristics of three reaction wheels designed for different classes of satellites.

Table 1 Reaction wheels

Reaction wheel	200SP-M [92]	100SP-M [92]	CubeWheel Med. [14]
Angular momentum	12 Nms	1.5 Nms	0.01 Nms
Max torque	0.24 Nm	0.11 Nm	0.001 Nm
Mass	5.2 kg	2.6 kg	0.13 g
Intended for	Satellites up to 500 kg	Satellites up to 200 kg	CubeSats

While the air bearing platforms designed for large satellites in previous years are often very capable, they cannot be exploited for light-weight small satellites, which are very widespread nowadays. An especially challenging task is CubeSat ADCS HIL testing. Such platform must be capable of the same functionality as its larger analogues, but have mass properties comparable to CubeSats. Moreover, CubeSat actuators are feeble and they have very limited operability margin that leads to high disturbance sensitivity. Thus, requirements to the low-torque environment of CubeSat tests must be much stricter than those for large satellites.

During 15 years of CubeSat history, several rotational air bearing platforms for ADCS have been developed by different institutions. Their parameters and features are discussed below. Two types of CubeSat-related test platforms can be distinguished based on their functionality: some permit dynamic tests and verification of ADCS (testbeds) while others are devoted to control law studies (simulators). It shall be noted that this categorization is not very rigorous. Indeed, testbeds can be used also for control algorithms development. However, the main distinction is that testbeds are adapted to accommodate different CubeSats and components, but simulators are supposed to be a representation of CubeSat inertia and mass properties. Simulators comprise predefined selection of verified ADCS components that are not expected to be changed. In other words, testbeds are used (or potentially can be used) for functional ADCS HIL tests within a real mission preparation, while simulators are limited to laboratory experimentations.

One of few CubeSat ADCS testbeds is the NanoSat Air Bearing developed by Berlin Space Technologies [93]. This testbed is suitable for 1-3U CubeSats and available off the shelf. The NanoSat Air Bearing provides only 1 DoF about yaw axis that limits its application for ADCS testing. However, its obvious advantage is its small moment of inertia (MoI), which is estimated as 7.5% of 1U MoI. The platform also permits adjustment of CoM within the range ±10 mm and can be optionally equipped with Helmholtz coils and a sun simulator.

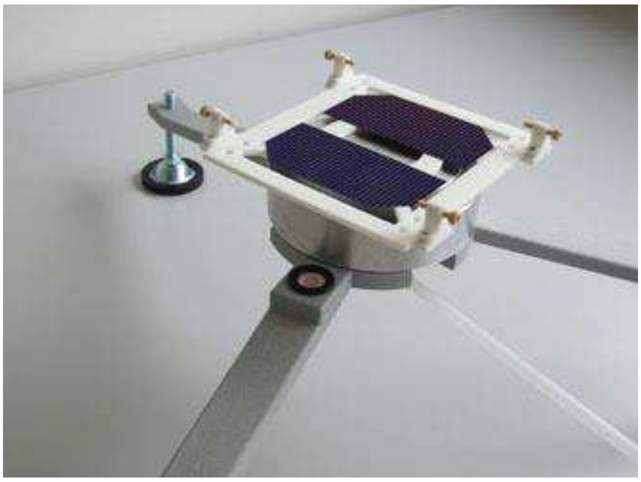

Figure 1.6-1 The NanoSat Air Bearing [93]

The Russian company SPUTNIX proposes a facility, called SX-025, for microsatellite dynamics study, which consists of a Helmholtz cage, sun simulator and an air bearing platform with load capacity up to 25kg [46]. The air bearing table allows unconstrained rotation about yaw axis and limited tilt in roll and pitch. The SX-025 facility can be used either as a testbed for ADCS and its components or as a simulator for educational and research purposes.

The testbeds above are designed by the companies and available as off the shelf products. However, several other examples of CubeSat air bearing platforms can be found in the literature.

Figure 1.6-2 SX-025 nanosatellite test facility [46]

Researchers at MIT in collaboration with Draper Laboratory developed a 3 DoF spherical air bearing testbed for ExoplanetSat project [94]. ExoplanetSat is a CubeSat technology demonstration mission with a goal to monitor a single sun-like star for two years in order to find a transiting exoplanet. During orbit day, ExoplanatSat tracks the target star and during orbit night it recharges batteries. In order to extend efficient time for star observation, a fast reorientation is required. Accurate target pointing together with fast maneuver is a challenging task for CubeSat ADCS. The air bearing testbed with ExoplanetSat simulator is used to demonstrate the pointing control algorithms on flight-like hardware (Figure 1.6-3). The testbed uses Specialty Components SRA250 spherical air bearing and provides free yaw rotation and approx. ±45° tilt in roll and pitch. The testbed CoM is placed within a few micrometers from its CoR that is achieved thanks to even payload placement and usage of six translational stages, which are able to shift small masses. Additionally, the testbed comprises a star field simulator and Helmholtz coils.

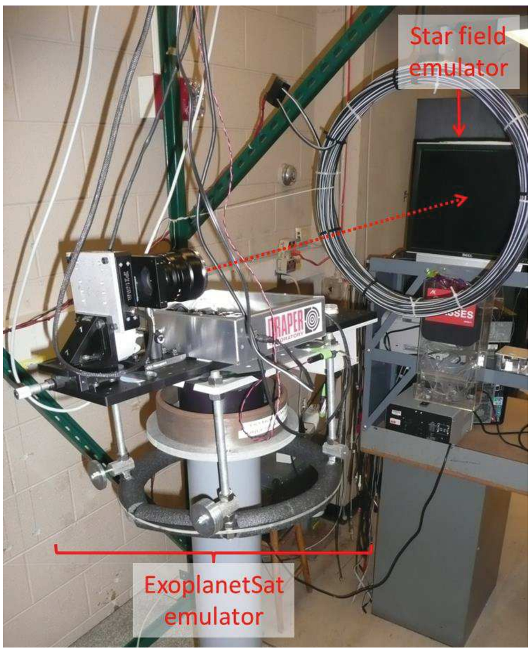

Figure 1.6-3 Air bearing testbed with ExoplanetSat simulator [94]

Experimentation with this testbed revealed several shortcomings. The cables connecting the testbed to the outside base added some damping and tended to stabilize the testbed. These issues were revised in the second version of the testbed, which is also equipped with improved payload hardware to make the experimentation simulator closer to the flight product.

The air bearing simulator designed at York University is used for attitude control law tests [57]. It consists of an air bearing, a manual balancing system, IMU, a wireless transceiver and set of Li-Ion batteries. The ADCS payload includes MEMS magnetometers and built in-house magnetorquers and reaction wheels. The simulator provides free rotation about yaw axis and ±45° tilt in roll and pitch. At a next stage of the simulator development, it was completed with a Helmholtz cage to test the performance of pure and hybrid magnetic control methods.

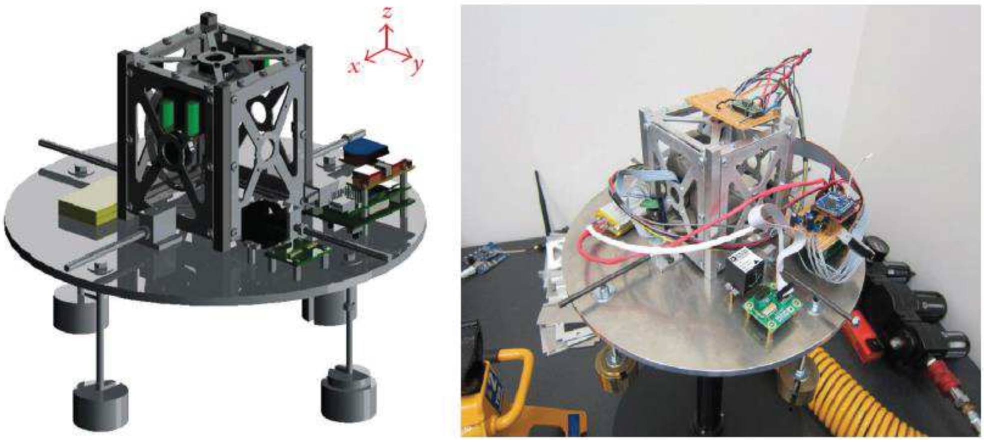

Figure 1.6-4 Air bearing simulator at York University [57]

The CubeSat Three-Axis Simulator (CubeTAS) is developed at the Spacecraft Robotics Laboratory of the Naval Postgraduate School for experimental testing of ADCS and its control methods [56], [83]. The simulator has four main parts: an air bearing platform, a Helmholtz cage, a sun simulator and a metrology system composed of four stereo cameras. The air bearing allows unconstrained rotations in yaw axis, but roll and pitch axes are limited to ±50°. The design of the air bearing platform takes into account size, volume and mass of a nanosatellite. Thus, the total mass of the floating hemisphere is 4.3 kg. All ADCS components are mounted inside of the hemisphere; there are three reaction wheels, magnetic coils, sun sensor and IMU. The hemisphere is also equipped with an auto balancing system that involves three shifting masses and corresponding motors [95]. CubeTAS was successfully used for CubeSat dynamics simulation by performing a three-axis stabilization maneuver. In a near future, validation of the magnetic attitude control techniques on CubeTAS is expected.

To the best of our knowledge, these are all air bearing platforms designed for CubeSat ADCS evaluation known from the literature. Moreover, only two of them (The NanoSat Air Bearing and SX-025) can be directly applied for any CubeSat ADCS. The ExoplanetSat simulator is designed and calibrated only for one project, while theoretically could be adapted for other CubeSat. Other air bearing platforms are simulators which comprise verified selection of ADCS components. They can be used only for laboratory experimentations and control study.

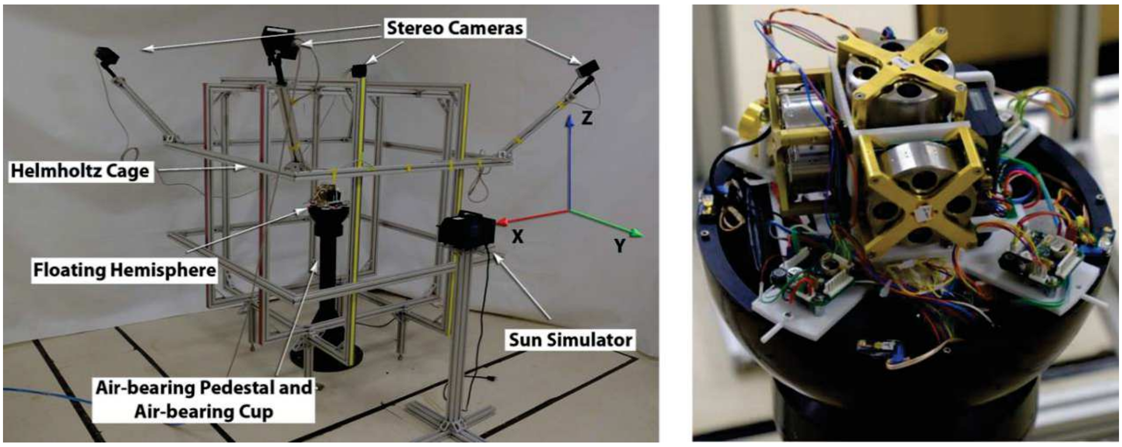

Figure 1.6-5 CubeTAS system overview (left) and hemisphere interior (right) [56]

It shall be also highlighted that all air bearing platforms for CubeSats have tabletop configuration and, consequently, their rotational freedom is significantly constrained. Indeed, umbrella or dumbbell configurations expect larger mass and inertia of the payload plate that is crucial for CubeSat actuators.

1.7 Technical requirements for the CubeSat ADCS testbed with improved performance

Despite 15 years of CubeSat history, necessity of ADCS functional tests arose recently, when nanosatellite missions matured enough for complicated attitude control. Thus, the list of the air bearing platforms appropriate for CubeSat ADCS is very limited. Summarizing the overview of those platforms, it is clear that development of testbeds for CubeSat ADCS HIL tests is a relatively new and not fully developed topic. Furthermore, for effective ADCS evaluation, the operational range of air bearing testbeds must be extended.

Following the survey of the existing platforms and their characteristics, it was decided to design a new CubeSat ADCS air bearing testbed with extended capabilities.

1.7.1 Perturbations caused by space environment

The major design effort is to maintain all interfering torques in the testbed at a low level to simulate their absence in space. In order to estimate the acceptance level, the disturbance torques, which would act upon an actual CubeSat in orbit, are calculated.

The perturbations that the CubeSat experience in orbit are caused by the fundamental effects of the space environment: the gravity gradient, atmosphere, solar pressure and the Earth magnetic field; or by internal factors: mass expulsion and momentum exchange between moving parts. The momentum exchange is typically well predicted and included in the attitude control algorithms to be compensated whereas the torque caused by the mass expulsion is unpredictable. The possible sources of the unexpected mass expulsion are the erosion of materials and gas leaks. In case of CubeSats, they are either too small to be noticed (erosion from small CubeSat-scale external surfaces) or too large (thruster leaks) to be included in the nominal performance mode. Thus, while the perturbations caused by internal factors cannot be judged, the torques from external effects can be well estimated.

1.7.1.1 Gravity gradient torque

The gravitational force between two point masses was formulated by Newton and first published in 1687 in the Principia. In vector form, it is written:

$$\mathbf{F}_{grav} = -G\frac{m_1 m_2}{r^3}\mathbf{r}\ , \tag{1.1}$$

where G is the gravitational constant, m_1 and m_2 are the two point masses, $\mathbf{r}$ is the position vector from the point mass 1 to the point mass 2 and r is the norm of $\mathbf{r}$. As (1.1) shows, the gravitational force is nonlinear and depends on the distance between the point masses. For a point mass, the gravitational force is applied at its center, but being integrated over a distributed body with an arbitrary shape, it can act at a point other than the body CoM. This effect generates the gravity gradient torque $\mathbf{T_{gg}}$ that acts upon a satellite on the Earth orbit (Figure 1.7-1). The gravity gradient torque is used in the passive attitude control systems (Section 1.3) to stabilize satellite orientation, otherwise it is considered as a perturbation factor.

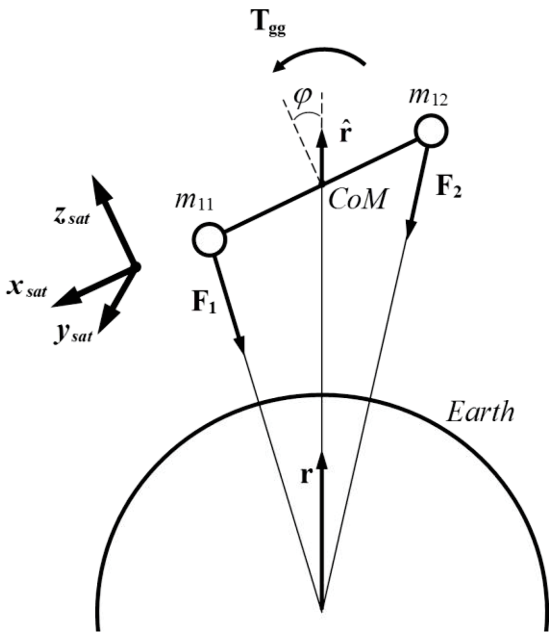

Figure 1.7-1 Gravity gradient

The satellite in orbit experiences an influence from the gravitational fields of the closest space objects, which are Sun, Moon and Earth. However, in LEO (the most common orbit for CubeSats) the effects from the Sun and Moon gravity gradients are negligibly small with respect to the one from Earth [96]. Thus, only the gravity gradient torque caused by the Earth gravitational field is considered below. The torque acting on a satellite can be found as:

$$\mathbf{T_{gg}} = \int \mathbf{r_{um}} \times d\mathbf{F_{grav}} \tag{1.2}$$

where $\mathbf{r_{um}}$ is the position vector of a unit mass of the satellite with respect to its CoM. Then, (1.2) can be given in matrix form:

$$\mathbf{T_{gg}} = \frac{3\mu_E}{r_{orb}^3}\left(\hat{\mathbf{r}} \times \mathbf{I_{sat}}\hat{\mathbf{r}}\right), \tag{1.3}$$

where μ_E is the standard gravitational parameter for Earth, r_{orb} is the orbit radius, $\hat{\mathbf{r}}$ is the unit position vector of the satellite with respect to the Earth CoM as it is shown in Figure 1.7-1, $\hat{\mathbf{r}}$ is defined in the satellite frame, $\mathbf{I_{sat}}$ is the satellite MoI matrix and the symbol $\times$ stands for the cross product of two vectors.

In order to estimate the disturbance torque from the gravity gradient, several representative CubeSat configurations are taken into account; their parameters are given in Table 2.

Table 2 CubeSat configurations and their physical parameters for the perturbation torques calculation

Configuration	Mass, kg	MoI, kg·m²	Maximum projected area, m²	Maximum CoM offset from the geom. center, mm [7]
1U 	1.13	$diag\begin{bmatrix}2.0\\2.1\\2.3\end{bmatrix}\cdot 10^{-3}$	0.01	$\begin{bmatrix}\pm 2\\\pm 2\\\pm 2\end{bmatrix}$
3U (conf. 1) 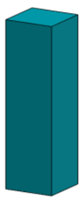	4.45	$diag\begin{bmatrix}47\\47\\8\end{bmatrix}\cdot 10^{-3}$	0.033	$\begin{bmatrix}\pm 2\\\pm 2\\\pm 7\end{bmatrix}$
3U (conf. 2) 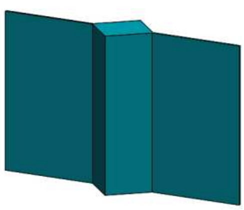	4.45	$diag\begin{bmatrix}57\\57\\28\end{bmatrix}\cdot 10^{-3}$	0.178	$\begin{bmatrix}\pm 2\\\pm 2\\\pm 7\end{bmatrix}$
3U (conf. 3) 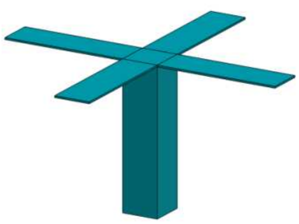	4.45	$diag\begin{bmatrix}76\\76\\48\end{bmatrix}\cdot 10^{-3}$	0.146	$\begin{bmatrix}\pm 2\\\pm 2\\\pm 7\end{bmatrix}$

Assume the unit position vector in the satellite frame to be $[-\sin\varphi \quad 0 \quad \cos\varphi]$. A static equilibrium for the satellite corresponds to its orientation where the one of the main inertia axes is aligned with $\hat{\mathbf{r}}$, thus the worst case takes place when $\varphi = \pi/4$ and, consequently, $\hat{\mathbf{r}} = [-0.5 \quad 0 \quad 0.5]$. Being given $\mu_E = 3.986 \cdot 10^{14}$ m^{3}s^{-2}, $r_{orb} = 6671 \cdot 10^3$ m for 300 km orbit and $r_{orb} = 6971 \cdot 10^3$ m for 600 km orbit, the gravity gradient torque is calculated for different CubeSat configurations and results are shown in Table 3.

1.7.1.2 Aerodynamic torques

The torques caused by the aerodynamic drag, as well as those from solar pressure, highly depend on the solar and geomagnetic activity and on the orbit height.

The aerodynamic force acts on the satellite in the direction opposite to the orbital velocity vector and applied at the center of pressure. The force magnitude is defined as follows:

$$F_{aero} = SC_D \frac{\rho v^2}{2}, \tag{1.4}$$

where S is the frontal projected area, C_D is the aerodynamic drag coefficient, ρ is the atmospheric density and v is the orbital velocity. The atmospheric density is a function of many parameter of the near Earth environment (Figure 1.7-2). It can be predicted by means of the semi-empirical models of the atmosphere, for example, the Jacchia-Bowman 2008 Model used in The Committee on Space Research International Reference Atmosphere – 2012 [97].

The aerodynamic torque appears when the center of pressure is different from the satellite CoM. The center of pressure location depends on the satellite orientation in the aerodynamic flow, thus the torque can be obtained as follows:

$$\mathbf{T_{aero}} = \int \mathbf{r_{uS}} \times C_D \frac{\rho v^2}{2} dS \tag{1.5}$$

or:

$$\mathbf{T_{aero}} = \mathbf{r_{CoP}} \times \mathbf{F_{aero}} \ , \tag{1.6}$$

where $\mathbf{r_{uS}}$ is the position vector of a unit area dS of the satellite surface with respect to the CoM, and $\mathbf{r_{CoP}}$ is the vector from the satellite CoM to its center of pressure.

The coefficient C_D can be assumed as 2.2 and the orbital velocity $v = 7726$ m/s for 300 km orbit and $v = 7562$ m/s for 600 km orbit. The complete analysis of the influence of the Earth atmosphere on the satellite can be obtained by means of specific software that allows precise modeling of the atmosphere and the satellite geometry. However, representative values of the aerodynamic torque can be estimated for certain satellite orientations. Thus, for the CubeSat configurations in Table 2, it can be assumed that the aerodynamic flow is perpendicular to the plane containing the maximum projected area. The center of pressure is coincident with the geometrical center and the CoM has the maximum acceptable offset. Being given these assumptions, the estimated aerodynamic torques are calculated according to (1.6) and the results are given in Table 3.

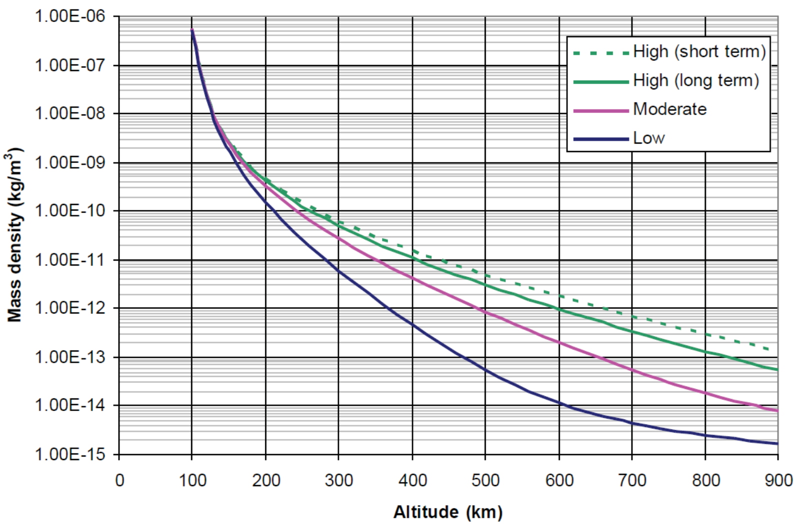

Figure 1.7-2 JB2008 mean atmosphere density with altitude for low, moderate, high long- and short-term solar and geomagnetic activity (from [97])

1.7.1.3 Solar pressure torque

Solar pressure is generated by sun light reflected and absorbed by the satellites surfaces. Its value is a function of the satellite geometry and optical properties of its surfaces. The resultant force of solar pressure acts at the optical center of pressure, so that when it is not coincident with satellite CoM, a disturbance torque is generated.

The force of solar pressure is defined as follows [98]:

$$F_{sol} = \frac{I_s S(1+K)}{c} \quad , \tag{1.7}$$

where $I_s \cong 1360\ \mathrm{W/m^2}$ is the solar constant, S is the frontal area, K is the reflectivity ($0 < K < 1$), c is the speed of light in vacuum. Then, the generated torque is found similarly to the case of the aerodynamic drag (1.5) and (1.6), so that if distance between CoM and the optical center of pressure is denoted r_{CoP} :

$$\mathbf{T_{sol}} = \mathbf{r_{CoP}} \times \mathbf{F_{sol}} \tag{1.8}$$

To estimate the solar pressure torque acting on CubeSats, the assumptions analogous to those for $\mathbf{T_{aero}}$ are made and the results are shown in Table 3.

1.7.1.4 Magnetic torques

The Earth magnetic field $\mathbf{B_E}$ interacts with the satellite residual magnetic dipole $\mathbf{M_{sat}}$ and induces a magnetic torque that tends to spin the satellite:

$$\mathbf{T_{mag}} = \mathbf{M_{sat}} \times \mathbf{B_E} \tag{1.9}$$

The residual dipole can appear due to residual magnetization and current loops on board of the satellite [98]. There are several techniques to minimize the residual magnetization before launch, but they are rarely applied to CubeSats. In the literature, there are not much data about CubeSats residual dipole strength: values given for 3U Space Dart and 2U PACE CubeSats are $9\cdot10^{-3}$ A·m² and $5\cdot10^{-4}$ A·m², respectively. It is difficult to predict the residual dipole for an arbitrary CubeSat, because the value depends strongly on the satellite wiring and the magnetic environment at pre-launch stages. Thus, based on the previously given data, $\mathbf{M}_{sat}$ is assumed to be 10^{-2} A·m² for 3U and 10^{-4} A·m² for 1U in the estimation of the magnetic disturbance torque.

The Earth magnetic field intensity highly varies with both latitude and altitude. The maximum values of the magnetic field strength are reached near Earth poles, the minimum values correspond to the near equator locations. The worst case magnetic torque $\mathbf{B}_E$ is assumed to be 50 μT for 300km orbit and 44 μT for 600km orbit which corresponds to the Earth magnetic field at near-polar regions in 2015 according to the International Geomagnetic Reference Field (IGFR-12) mathematical model [99]. Moreover, the worst-case alignment between the CubeSat dipole and the Earth magnetic field, which happens when they are perpendicular, is assumed. The corresponding results of the magnetic disturbance torques estimations are given in Table 3.

Table 3 Estimated disturbance torques for different CubeSat configurations

CubeSat configuration	Orbit height	Disturbance torques, N·m				
		Gravity gradient	Aerodynamic	Solar pressure	Magnetic	Total torque
1U	300 km	$0.6 \cdot 10^{-9}$	$1.49 \cdot 10^{-6}$	$2.31 \cdot 10^{-9}$	$5.0 \cdot 10^{-9}$	$1.49 \cdot 10^{-6}$
	600 km	$0.53 \cdot 10^{-9}$	$1.78 \cdot 10^{-8}$		$4.4 \cdot 10^{-9}$	$2.27 \cdot 10^{-8}$
3U (conf. 1)	300 km	$0.78 \cdot 10^{-7}$	$1.26 \cdot 10^{-5}$	$1.96 \cdot 10^{-8}$	$5.0 \cdot 10^{-7}$	$1.32 \cdot 10^{-5}$
	600 km	$0.69 \cdot 10^{-7}$	$1.51 \cdot 10^{-7}$		$4.4 \cdot 10^{-7}$	$6.6 \cdot 10^{-7}$
3U (conf. 2)	300 km	$0.58 \cdot 10^{-7}$	$6.55 \cdot 10^{-5}$	$1.02 \cdot 10^{-7}$	$5.0 \cdot 10^{-7}$	$6.62 \cdot 10^{-5}$
	600 km	$0.51 \cdot 10^{-7}$	$7.84 \cdot 10^{-7}$		$4.4 \cdot 10^{-7}$	$1.28 \cdot 10^{-6}$
3U (conf. 3)	300 km	$0.56 \cdot 10^{-7}$	$2.17 \cdot 10^{-5}$	$3.37 \cdot 10^{-8}$	$5.0 \cdot 10^{-7}$	$2.23 \cdot 10^{-5}$
	600 km	$0.49 \cdot 10^{-7}$	$2.60 \cdot 10^{-7}$		$4.4 \cdot 10^{-7}$	$7.49 \cdot 10^{-7}$

Table 3 gives an understanding of the estimated values for the CubeSat disturbance torques induced by the interaction with the space environment. It can be seen that on low orbits (up to 400 km), the aerodynamic torque dominates. The gravity gradient torque is slowly decreasing and it makes most of the total disturbance torque on orbits upon 700km. The magnetic torque varies a lot for different satellites and every developer considers the minimization of the residual CubeSat magnetization during pre-launch stages.

The maximum disturbance torque on orbit is the criterion by which ADCS actuators are selected. Actuators shall be able to control the CubeSat without noticing the disturbance torques. Thus, the actuators have to provide the control torque at least one order of magnitude larger than the value of expected disturbances. Accordingly, the disturbance torques generated by a CubeSat ADCS testbed shall to be within this range. It would be desirable that the level of the testbed residual disturbances is kept below the value of the orbital perturbations, but it is very difficult to obtain. Being given the estimated orbital disturbance torques for different CubeSat design (Table 3), the acceptable level of the testbed disturbance torques is assumed to be below 10^{-4} N·m. This value is based on expected perturbations for 3U CubeSat on 300 km orbit. While for higher orbits perturbations are lower, the actuators are often designed to match different missions and some safety coefficient is often taken into account. As most of CubeSats with active ADCS are 3U, actuators are mostly designed for them and can be applied for 1U missions having a margin of the control torque. The survey of COTS CubeSat actuators available in the specialized shops [12]–[14] confirms that their control torque does not go lower $2 \cdot 10^{-4}$ N·m.

1.7.2 Functional requirements

The CubeSat ADCS testbed, which has to be developed in frameworks of this thesis, is intended to extend the existing performance range. Requirements for the testbed given in Table 4 define its functionality and feasibility to be used for different satellites. Being able to accommodate CubeSats up to 3U, the testbed is suitable for the majority of existing nanosatellites. The supported range of mass up to 6 kg ensures the compatibility of the testbed with all CubeSats, regardless of a selected deployer standard. The most challenging task is to provide the testbed with the three unconstrained rotational DoF, while having a small MoI. The testbed in [93] provides 10% of 1U MoI while having 1 DoF, thus for the testbed with extended rotation freedom MoI is assumed to be 50% of 1U MoI, because the CubeSat support and adjustment system is expected to be more complex. The acceptable level of the testbed disturbance torques is selected according to the arguments discussed in Section 1.7.1 and is defined as 10^{-4} N·m. This value is very low and difficult to obtain. Moreover, it is impossible to reach this level of a residual disturbance torque without precise balancing. Thus, the testbed shall include a mass balancing system that allows the CoM and CoR alignment. In order to reduce the mass of the platform (and its MoI consequently), this system is intended to be manual. The constructive solutions allowing fulfillment of these requirements are discussed in details in Chapter 2.

Table 4 Testbed functional requirements

Accommodate satellites	1U … 3U
Holding capacity	Up to 6 kg
Rotational freedom	Unconstrained 3 DoF
Platform MoI	<50% of 1U MoI
Disturbance torque	10^{-4} N·m
Mass balancing	Manual

1.8 Conclusion

The past years of CubeSat development have shown not only a high demand for low cost nanosatellite missions, but also some weaknesses of these satellites including a wide use of nonqualified components and lack of prior to launch testing. Every year CubeSats are getting involved in more complicated missions resulting in complex configurations of their systems. Thus, recent generations of CubeSats require more comprehensive ground verification, including not only SIL and component-level HIL tests, but also system-level HIL tests. The ADCS HIL functional testing is a particularly challenging task, because ADCS performance depends on CubeSat dynamic parameters and its dynamics in the space environment. Thus, simulation of the space environment with minimized perturbation torques is essential for faithful ADCS verification. Some techniques of low-torque environment simulation are inherited from the experience of large satellites tests. The most appropriate one is the use of an air bearing platform, which efficiently eliminates the friction forces and permits an accurate balancing in order to minimize the gravity torque. During the 60 years of satellite development, tens of air bearing platforms have been built, the most representative of them were described in Section 1.5. However, only few platforms among them can be used for CubeSats due to significant differences of satellite sizes and actuators capabilities.

The number of CubeSat testbeds, which were discussed in Section 1.6, is very low and they have several important disadvantages including a tightly constrained freedom of rotation (only one axis has ±360°) and the large impact of the platform mass and inertia on the CubeSat dynamics. Meanwhile, the complexity of CubeSat missions constantly grows and their ADCS are designed to be as elaborated as those of large satellites. Thus, in order to improve capabilities of CubeSat ADCS ground testing, it has been decided to design and build a testbed with improved characteristics. The enhancement of the testbed functionality is mainly aimed to amend the existing disadvantages by expanding the range of possible CubeSat rotation up to ±360° around all axes. Moreover, a low level of residual disturbance torques is expected to be obtained by the minimization of external factors and precise mass balancing.

The goal of this work is thus to develop a testbed with improved performances in order to meet the aforementioned requirements. Potentially, such testbed may set a new level of ground ADCS HIL testing and increases the range of possible pre-launch ADCS evaluations. In the following chapter, different approaches to design such a testbed are discussed and one of them is studied in details.

Chapter 2. TESTBED CONCEPT AND PROTOTYPE

2.1 CONCEPT

The main goal of this work is to develop a testbed able to provide a CubeSat with an extended range of rotation during ground ADCS tests and, in addition, to study possibilities of the unconstrained CubeSat rotation in a low-torque environment. The essential element of the testbed is an air bearing, which ensures a near frictionless motion. The classical approach to use air bearings does not allow unconstrained payload motion that was illustrated by the overview of existent air bearing platforms in Chapter 1. Thus, an alternative design shall be developed. In this work three different possibilities are analyzed: a platform with dynamic compensation of the additional MoI; an air-levitated whole sphere testbed; and a refined modification of a whole sphere testbed called AirBall.

2.1.1 Dynamic compensation of MoI

The mechanical design of the testbed with dynamic compensation of MoI is based on a gimbal suspension allowing 3 DoF motion that is needed to meet the requirements presented in Section 1.7.2. The gimbal consists of three holding rings which are connected to each other by means of rotary air bushings. A simplified design of the gimbal with a 3U CubeSat is shown in Figure 2.1-1. It is easy to see that the inertia of the holding rings is substantial with respect to CubeSat MoI and it cannot be neglected. Thus, such testbed structure causes significant perturbations of the CubeSat dynamics, which is inadmissible for low-torque environment simulations.

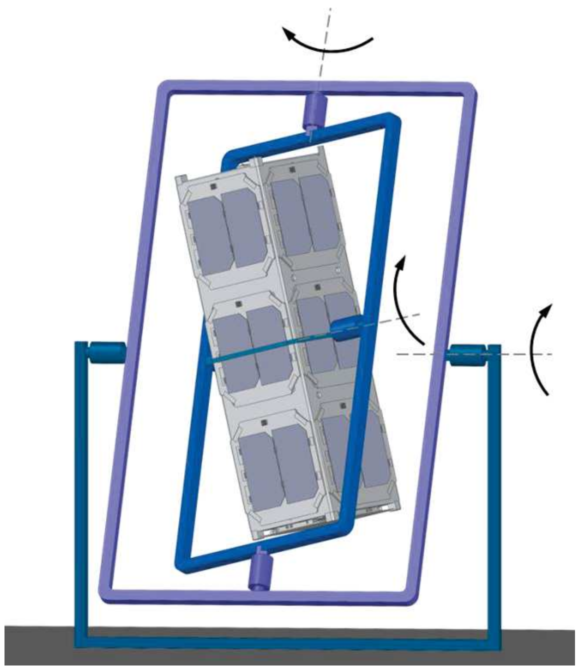

Figure 2.1-1 3U CubeSat on gimbal suspension

The principle of compensating the additional MoI is aimed at minimizing influence from testbed elements on the CubeSat dynamics. To this end, every joint shall be equipped with a sensor and a motor. The sensor is used to obtain knowledge of the rotor motion, thus the angular position of the rotor or its acceleration shall be measured. The motor shall be able to provide a required torque to the platform, so that the effect of a known additional MoI to the CubeSat dynamics is eliminated. In order to benefit the minimized friction of air bushings, the direct drive slotless motor is preferable to use.

The MoI compensation implemented to the 3 DoF gimbal is a challenging task to start with, thus it was decided to build a 1 DoF experimental setup in order to check feasibility and applicability of the compensation approach. Figure 2.1-2 schematically illustrates the concept of the experimental setup.

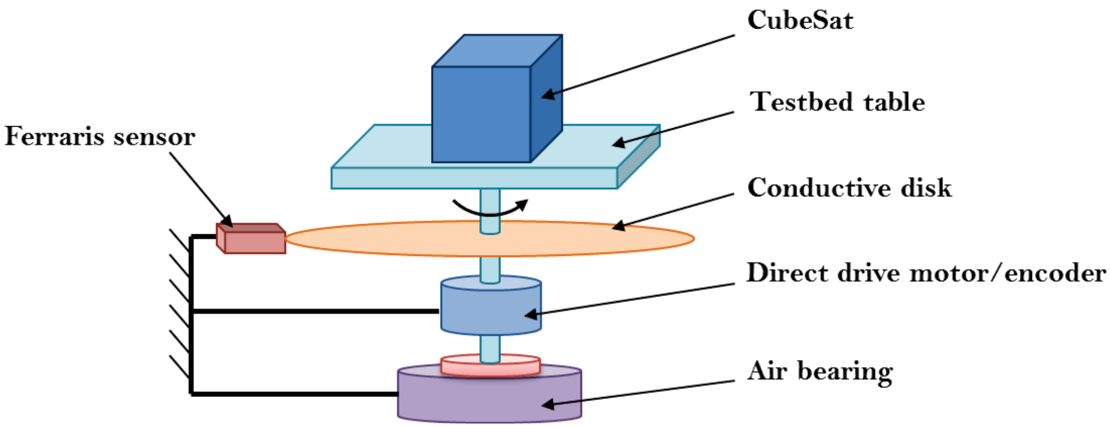

Figure 2.1-2 Concept of the 1 DoF planar platform with the MoI compensation

2.1.1.1 Experimental setup with 1 DoF

Two types of sensors can be potentially used in this compensation scheme: rotary encoders and Ferraris sensors. Rotary encoders are widely used and well-known sensors, which are able to convert angular position or motion of an axle to a digital code. Rotary encoders have a wide range of operation characteristics and can be found in different designs.

Ferraris sensors are able to directly measure angular accelerations of a rotor. When time derivatives of the position are required, there is no need to differentiate the output signal. It increases the performance of a highly-dynamic system with control loop [100]. Nevertheless, Ferraris sensors have a disadvantage which could be critical for their use in systems with tight size requirements. While Ferraris sensors are small, they require a conductive and non-magnetic disk connected to the rotor to induce eddy currents. The diameter of this disk influences the accuracy of the measurements. The tangential acceleration detected by the sensor increases with distance from the center of rotation. Accordingly, with a large disk the sensor needs smaller gain to obtain measurements and provides less noise. Thus, diameter of a disk is a result of trade-off between efficiency and dimensions of the measurement system.

The MoI compensation for the testbed requires good accuracy of measurements. Any noise, as a result of the double differentiation of the position signal, dramatically affects the system efficiency. Thus, the Ferraris sensor is considered as an essential option for the experimental setup measurement system. The Hubner Berlin Ferraris sensor accompanied by a $\varnothing$ 285 mm aluminum disc is selected for the setup. However, the rotary encoder is also included in order to estimate the impact of the differentiation noise in the data.

For actuation of the compensation system the high precision rotary stage ABRS-250 by Aerotech is used [101][102]. While the stage is designed to be used for accurate positioning, it perfectly matches the requirements of the compensation system concept. The rotary stage comprises both an air bearing and a brushless slotless direct drive motor with an inbuilt encoder. As any air bearing based system, the rotary stage has to be provided with compressed and filtered air. For this purpose the air filtration unit is engaged. The selected one is provided by Aerotech and it ensures filtered to 0.25 microns, dried to -18° C dewpoint and oil free air flow.

In order to emulate the additional MoI, which has to be compensated, two solid inertia wheals are used. Thus, using one or two of them, the compensation of different MoI can be studied. The rotor of the stage and the aluminum disc are considered to be a basic payload.

The 1 DoF experimental setup is shown in Figure 2.1-3.

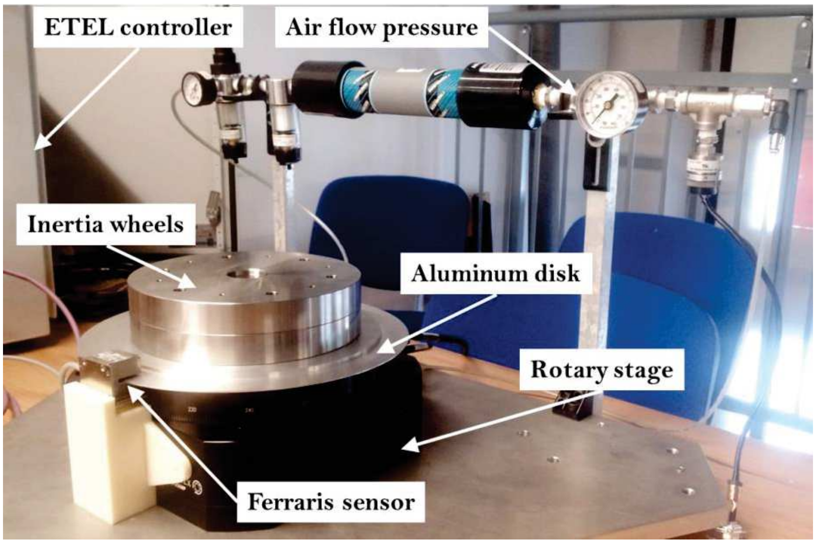

Figure 2.1-3 Experimental setup

2.1.1.2 Experiment

The goal of the experiment with the 1 DoF setup is to check the efficiency of the dynamic MoI compensation. To this end, motion of the payload is observed for three cases:

- basic payload without motor actuation;
- basic payload + additional MoI without motor actuation;
- basic payload + additional MoI with motor actuation.

An external torque is applied to the payload in order to initiate a motion sequence. While the external torque is quantified and similar for all three cases, the conclusion on the compensation approach efficiency can be done based on the observed response. The equation of the 1 DoF platform motion for first case is:

$$I_P \ddot{\theta}_P(t) = T_{ext}(t) + T_{fr}, \tag{2.1}$$

where I_P is MoI of the basic payload, $\ddot{\theta}_P$ is the angular acceleration of the payload, T_{ext} and T_{fr} are the torques caused by the external actuation and friction, respectively. Since the platform is equipped with an air bearing, the friction torque is considered negligible and T_{fr} is set to zero here and below. For the case with the additional MoI I_{ad}, the equation of motion is:

$$\left(I_P + I_{ad}\right)\ddot{\theta}_{P+ad}\left(t\right) = T_{ext}\left(t\right) \tag{2.2}$$

Thus, when the external actuation is similar to that in (2.1), the dynamics of the platform (angular acceleration $\ddot{\theta}_{P+ad}$ is observed) is different. Then the torque applied to compensate the influence of additional MoI shall be:

$$T_{comp}\left(t\right) = I_{ad}\ddot{\theta}_{P+ad}\left(t\right), \tag{2.3}$$

However, in the real system, T_{comp} can be calculated based on the previous value $\ddot{\theta}_{P+ad}\left(t-\tau\right)$ and, as result, a delay τ appears. The delay depends on the operation frequency and the approach to the sensor data processing. Thus, full equation of motion becomes:

$$\left(I_P + I_{ad}\right)\ddot{\theta}_{P+ad}\left(t\right) = T_{ext}\left(t\right) + I_{ad}\ddot{\theta}_{P+ad}\left(t-\tau\right) \tag{2.4}$$

The compensation principle given by (2.4) is employed in the control scheme for the experimental setup, which is shown in Figure 2.1-4.

The control scheme of the experimental setup is implemented in MATLAB Simulink. During the experiment it runs on the xPC target computer and allows real-time hardware control. For the motion control of the stage, the ETEL controller is engaged. It is able to communicate with the target PC and allows torque control of the stage, as it is shown in Figure 2.1-5.

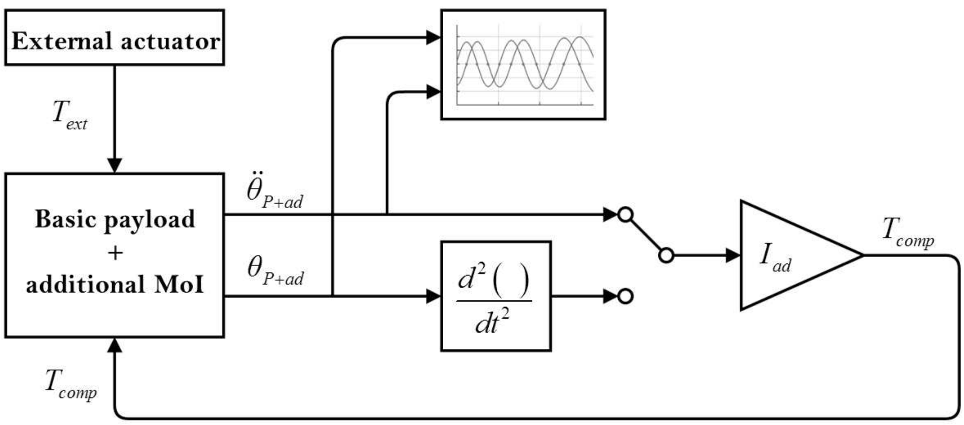

Figure 2.1-4 Control scheme for the dynamic MoI compensation on the 1 DoF experimental setup

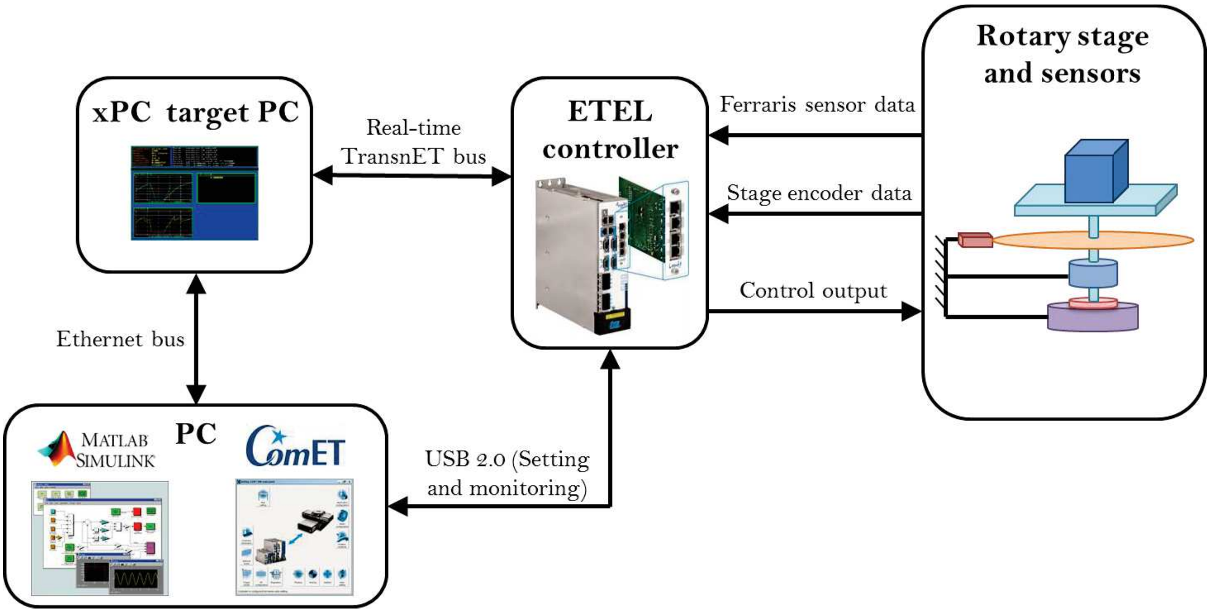

Figure 2.1-5 Experimental setup scheme

During the experimental work, several technical issues have appeared. The critical one was the rotary stage breakdown, which lead to the significantly high friction in the system so, that faithful experimental data was impossible to achieve. Hence, the experimental verification of the dynamic MoI compensation principle is postponed to future works in this field. However, some concerns regarding the perspectives of this approach for 3 DoF CubeSat ADCS testbed can be highlighted based on aforementioned progress of the work:

- The rotary stage ABRS-250 selected for the experimental setup is not the most optimal solution for the 3 DoF testbed with dynamic MoI compensation, because it is very heavy (15.6 kg total mass) and capable of unnecessary high torque and axial load. However, even more compact solution for the combination of an air bearing and a motor are bulky and, probably, insufficient once the system is extended to 3 DoF;
- Dynamics of all three element of the gimbal are tightly coupled. Thus, I_{ad} is not a constant anymore, but it is a nonlinear function of time and orientation of the inner gimbal elements. For the external ring the compensation torque will be following:

$$T_{comp\_3}(t) = I_{ad}(t-\tau,\varphi,\gamma)\ddot{\theta}_{P+ad}(t-\tau), \qquad (2.5)$$

where angles φ and γ describe orientation of the inner ring and the payload platform with respect to their initial orientations. As result, influence of the control system delay significantly increases for 3 DoF and it might be critical for the testbed performance.

Summarizing the earned experience in the development of the dynamic MoI compensation for the CubeSat ADCS testbed, it can be concluded that this approach is more suitable for 1 DoF platform. The difficulties associated with implementing the 3 DoF system prevail over advantages, which can be potentially achieved.

2.1.2 Air-levitated whole sphere

An alternative approach to the design of the CubeSat ADCS testbed with extended rotational freedom is an air-levitated whole sphere. Several developers of air bearing platforms have come up with such idea.

The sphere built for the experimental study on the synchronized rotation of multiple spacecrafts at University of California in cooperation with Jet Propulsion Laboratory [86] potentially has three unconstrained degrees of rotation, however, only the rotation about the vertical axis was employed in the experiment, because of a single flywheel inside the sphere.

At Naval Postgraduate School, the first concept of the testbed for CubeSat ADCS was supposed to engage a whole acrylic sphere levitating over an air bearing [83]. In the final design only one half of the sphere was used (Figure 1.6-5) due to difficulties to manufacture the smooth separable sphere that matches specifications.

Other example of the floating sphere is presented by EyasSat LLC [103]. A transparent sphere with a CubeSat simulator mounted inside (Figure 2.1-6) is intended to be used for classroom trainings. The developer claims possibility to change components inside the sphere with any customer's modules and to communicate with the CubeSat simulator by radio channel. Unfortunately, there is not much information available about this device except of the demonstration video [104].

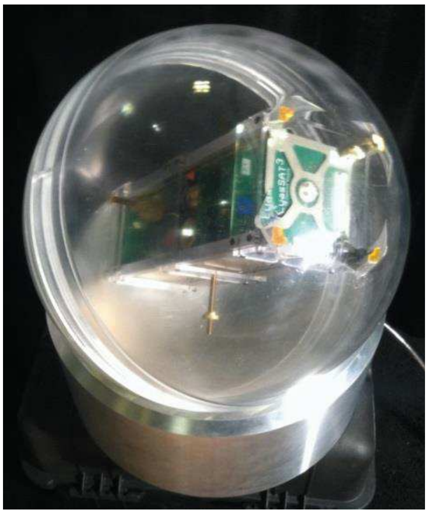

Figure 2.1-6 EyasSat's sphere for ADCS simulations

The concept of air-levitated hollow sphere is a natural way to exceed the limits of the air bearing platform performance. Indeed, constrains of the angular motion are caused by the hemispherical shape of the payload table. Thus, removing the pedestal and replacing a common hemisphere with a whole sphere eliminate geometrical restrictions.

However the air-levitated sphere has several disadvantages. Besides aforementioned manufacturing difficulties, which can stop a developer from realizing this concept, the hollow sphere features significant MoI. Thus, average MoI of an acrylic ∅450 mm sphere (large enough to accommodate 3U CubeSat) with 5mm thickness three times exceeds 3U CubeSat MoI. Such sphere dramatically impacts the CubeSat dynamics and, while being a suitable solution for simulators, it cannot be successfully used as a testbed for CubeSat ADCS functional tests.

2.1.3 AirBall

This work is focused on the concept that, while being different in details, retains the key advantage of the hollow sphere, which is the continuous friction-free contact between the CubeSat support and the air bearing. The concept is based on an idea that this property can be achieved by replacing the whole sphere with evenly spread spherical segments with a common center, as it is illustrated on Figure 2.1-7. This concept of the CubeSat ADCS testbed was called AirBall. It allows the low-torque environment and minimal additional MoI.

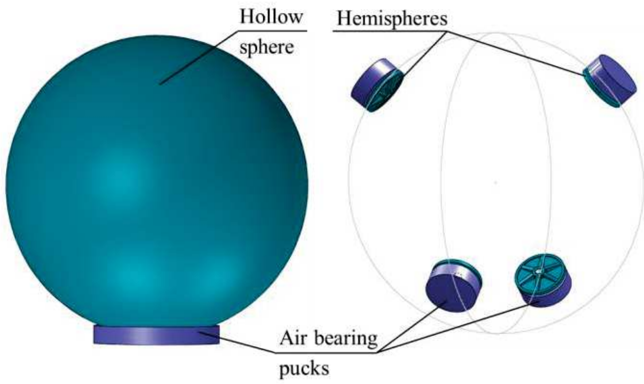

Figure 2.1-7 An air-levitated sphere and a spherical structure of the same diameter formed by several air bearings

The inner part of the AirBall, conventionally called Inner Sphere, consists of small spherical segments (i.e. passive parts of the air bearings) that makes it smaller and lighter than the air-levitated spheres. Minimizing the size and mass of this part of the testbed is essential because of its unwanted MoI.

In order to ensure friction-free contact and enough lift force at every orientation, the single large air bearing (inherent for the air-levitated sphere) is replaced with several small ones opposite to the passive parts. Additionally, the frame (called Outer Sphere), on which the active parts are attached, must follow the motion of the Inner Sphere so that active and passive parts of air bearings remain aligned. To this end, a motorized gimbal is engaged to guide the motion of the Outer Sphere around a single center of rotation. The CoR is common to both the Inner and Outer Spheres and it is coincident with the common intersection point of all gimbal revolute joint axes.

The CubeSat is fixed to the Inner Sphere by means of an adjusting mechanism, which allows limited modifications of the satellite position with respect to the CoR. This feature is required to provide precise mass balancing by aligning the Inner Sphere CoM and CoR.

The natural dynamics of the CubeSat is a key point of ADCS HIL tests, so CubeSat motion shall not be predicted but only observed. Moreover, positioning the Outer Sphere has to be rapidly corrected based on the current position of the CubeSat. Thus, the AirBall involves also a measurement system able to define current CubeSat orientation. This is important for both corrections of the Outer Sphere orientation and ADCS performance evaluations.

Summarizing the proposed testbed concept, five main elements can be distinguished:

- The Inner Sphere composed of the passive parts of the air bearings attached to the CubeSat;
- The Outer Sphere, i.e. the air bearing active parts held by the rigid frame;
- The gimbal able to rotate the Outer Sphere around the fixed CoR;
- The CubeSat fastening and adjusting mechanism;
- The measurement system

2.2 DETAILED AIRBALL DESIGN

2.2.1 Inner and Outer Spheres

The Spheres are essential in the AirBall design. The Inner and Outer Spheres hold the passive and active parts of the air bearings, respectively, and provide mechanical interfaces with the CubeSat and the gimbal.

Two types of air bearings are typically distinguished: "orifice" and "porous media" bearings. Their major difference is in the bearing surface. In case of orifice bearings the pressurized air is supplied through a small number of precisely sized holes, while in porous media bearings the air is supplied through the entire porous surface that has millions of miniature holes. Thanks to the porous technologies, the air pressure remains almost uniform across the entire surface and air bearings operate even after being stretched [105]. For the AirBall testbed, 40mm porous carbon air bearings produced by New Way are selected. The nominal lift force of the bearings is 178N that is enough to hold 3U CubeSat with the Inner Sphere [106]. Usually air bearings are coupled with the hemispheric passive parts, but for the actual application a spherical cap shape is required. Thus, the passive parts are manufactured according to the custom design. Because the spherical cap with small diameter and respectively large radius is a thin shell, it causes large flexibility of the element. In order to have deformations of the passive part within an acceptable level, a trade-off between a small mass and bending stiffness is considered in the design.

Four air bearings shall be evenly distributed on the sphere that guaranty there is no deficiency of the lift force at any angle. Number of air bearings selected to be minimal and, meantime, to secure posture of the CubeSat in a sphere. Thus, they are placed at vertices of a regular tetrahedron inscribed in a sphere with radius 105mm (Figure 2.2-2a). This sphere is smaller than one circumscribed around 3U CubeSat, but a satellite of this size still can be hold by the air bearing sphere as it shown in Figure 2.2-2c.

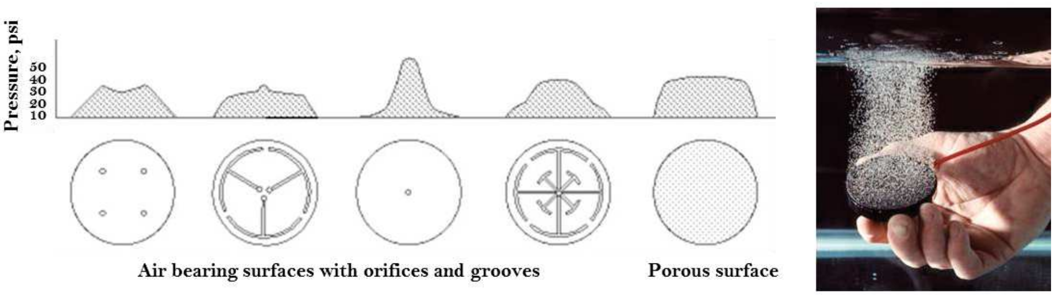

Figure 2.2-1 Orifice vs. porous media air bearings [105]

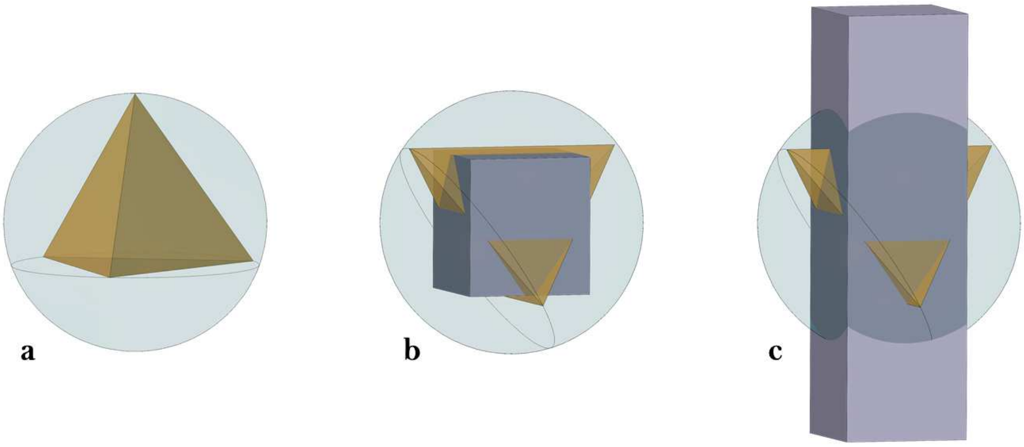

Figure 2.2-2 a – regular tetrahedron inscribed in a sphere; b and c - same sphere with 1U CubeSat- and 3U CubeSat-size cuboids, correspondingly

The frame of the Inner Sphere is designed to be as light as possible, because it is attached to the CubeSat. As dimensions of the Inner Sphere are constrained by the sizes of CubeSats and cannot be decreased, the total mass of the Inner Sphere with the passive parts of the air bearings and a CubeSat fastening mechanism shall be minimized in order to keep their total MoI within 50% of 1U CubeSat MoI. The frame holding the passive parts of the air bearings shall be accurately manufactured, so that tolerance of its dimensions does not exceed the nominal air bearings fly height, which is 5μm according to the data sheet [106]. Better accuracy of the frame shape can be achieved when it is machined out of a whole aluminum bar so that number of junctions is minimized, as it is typically done for a CubeSat main structure. However, considering sizes of the frame, this solution would be costly, so the sectional design of the frame is selected. It consists of four similar elements, which assembled together by means of four screws, as it is shown in Figure 2.2-3.

The Outer Sphere holds in place four active parts of the air bearings and provides a mechanical interface with the gimbal. Its design is not constrained by mass restrictions, because it is not connected to the CubeSat, thus its MoI does not affect satellite dynamics. Assembly of the Inner and Outer Spheres is illustrated in Figure 2.2-3.

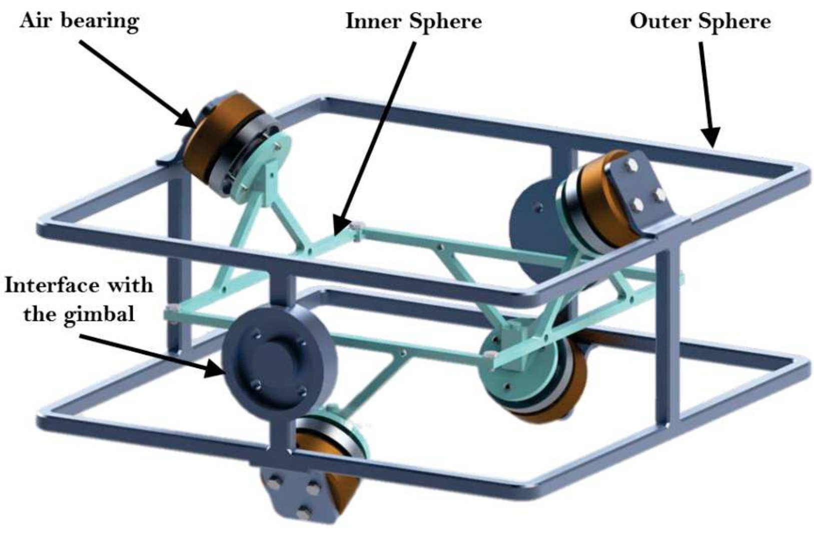

Figure 2.2-3 Inner and Outer Spheres

2.2.2 CubeSat fastening and adjustment mechanism

The adjustment mechanism is required for CubeSat fastening and mass balancing. The goal of mass balancing is to align CoM of the assembly, comprised the Inner Sphere and CubeSat, with CoR. Typically small shifting masses are used to change the CoM position. However, in order to minimize any additional masses attached to the CubeSat, different technique is proposed: By means of fine thread screws, which permit translations along the three main axes, position of the CubeSat can be precisely adjusted inside the Inner Sphere until CoM and CoR are coincident.

The concept of the proposed adjustment mechanism is shown in Figure 2.2-4. The CubeSat is fixed inside a holding square ring (1) by means of 8 small screws (2). The screws come through the threaded holes in the square ring and tightened to have a secure contact with the CubeSat rails. The ring has two pairs of the dovetail joints that are able to slide along the corresponding rails (4) on the inner surface of the L-shape brackets (3). Motion of the ring along Z axis is constrained by the fine-thread rolling ball set screws (5). In the plane XY four longer ball set screws (6 a, b) are driven through the threaded holes in the Inner Sphere frame. Their balls are able to slide along the rails (7) on the external surface of the L-shape brackets.

Thus, in order to allow CubeSat translation along X axis, one of two screws (6a) shall be tightened and other one shall be released by same number of turns. The CubeSat motion along Y axis is controlled in the same way with screws (6b). The screws (5) are engaged for translation along Z axis.

The range of available translation is ±20 mm along X and Y axis that corresponds to the CubeSat CoM position requirements specified in the CubeSat Design Specification [7]. The translation along Z axis is limited by ±10 mm, but the ring (1) can be fixed at almost any desired Z coordinate of the CubeSat structure. So the preliminary knowledge of the CubeSat CoM position, obtained from a CAD model, is used to minimize the required translation along Z axis.

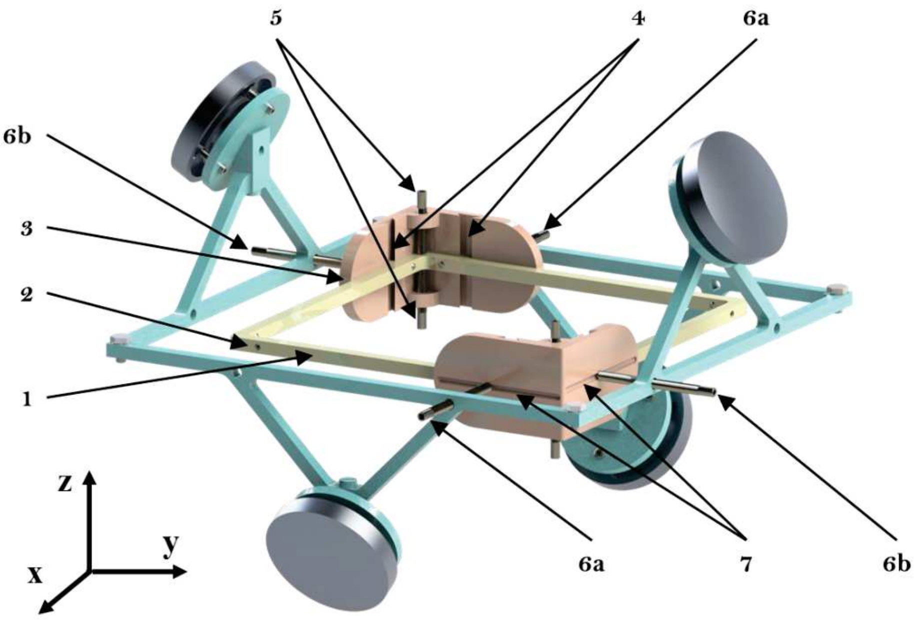

Figure 2.2-4 Fastening and adjustment mechanism

2.2.3 Robotic Gimbal

The robotic gimbal is engaged in the AirBall testbed to move the Outer Sphere in the way that it follows motion of the CubeSat and the active and passive parts of the air bearings remain aligned. The gimbal needs to have only 3 rotational DoF, because the motion shall be executed around the fixed CoR and translations are excessive. However, at certain angles the kinematic singularities occur and the gimbal loses its ability to move the end effector in the desired direction. In order to eliminate this inconvenient, the gimbal is designed to have 4 DoF. An additional DoF is employed to solve the redundancy in the desirable way, namely, to deal with a gimbal lock. The geometrical model of the robotic gimbal is shown in Figure 2.2-5.

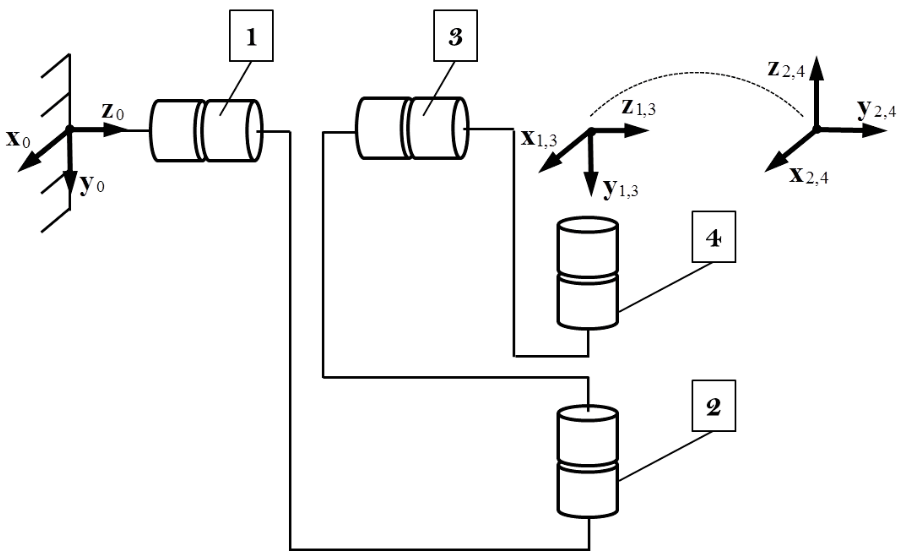

Figure 2.2-5 Geometrical model of the robotic gimbal

Table 5 Denavit-Hartenberg parameters for the robotic gimbal

Denavit-Hartenberg parameters				
Joint	α_i	d_i	r_i	q_i
1	0°	0	l	0
2	90°	0	0	0
3	-90°	0	0	0
4	90°	0	0	0

The Denavit-Hartenberg conventions have been used (Table 5) to specify the direct kinematics of the gimbal. The gimbal can be modeled through the homogeneous transformations matrices which are obtained as following:

$$^{i-1}\mathbf{T}_i = \mathbf{Tr}\left(\mathbf{x}_{i-1}, d_i\right)\mathbf{Rot}\left(\mathbf{x}_{i-1}, \alpha_i\right)\mathbf{Tr}\left(\mathbf{z}_i, r_i\right)\mathbf{Rot}\left(\mathbf{z}_i, d_i\right) \tag{2.6}$$

The entire relation is obtained multiplying these matrices in ascending order:

$$^{0}\mathbf{T}_n = {}^{0}\mathbf{T}_1 {}^{1}\mathbf{T}_2 {}^{2}\mathbf{T}_3 \ldots {}^{n-1}\mathbf{T}_n \tag{2.7}$$

The entire transformation matrix for the gimbal is below:

$$\mathbf{T}(q) = {}^{0}\mathbf{T}_1{}^{1}\mathbf{T}_2{}^{2}\mathbf{T}_3{}^{3}\mathbf{T}_4 = \begin{bmatrix} c_1c_2c_3c_4 - s_1s_3c_4 - c_1s_2s_4 & -c_1c_2c_3s_4 + s_1s_3s_4 - c_1s_2c_4 & c_1c_2s_3 + s_1c_3 & 0 \\ s_1c_2c_3c_4 + c_1s_3c_4 - s_1s_2s_4 & -s_1c_2c_3s_4 - c_1s_3s_4 - s_1s_2c_4 & s_1c_2s_3 - c_1c_3 & 0 \\ s_2c_3c_4 + c_2s_4 & -s_2c_3s_4 + c_2c_4 & s_2s_3 & l \\ 0 & 0 & 0 & 1 \end{bmatrix}, \tag{2.8}$$

where $c_i = \cos q_i, s_i = \sin q_i$.

The differential kinematic equation for the robotic gimbal can be written as

$$\dot{\mathbf{x}} = \mathbf{J}\dot{\mathbf{q}}, \tag{2.9}$$

where $\dot{\mathbf{x}}$ is the vector of the end effector velocities, $\mathbf{J}$ is the Jacobian matrix and $\dot{\mathbf{q}}$ is the vector of the joint velocities. Being given the transformation matrix (2.8), the Jacobian is

$$\mathbf{J} = \begin{bmatrix} 0 & s_1 & -c_1s_2 & c_1c_2s_3 + s_1c_3 \\ 0 & -c_1 & -s_1s_2 & s_1c_2s_3 - c_1c_3 \\ 1 & 0 & c_2 & s_2s_3 \end{bmatrix} \tag{2.10}$$

To find at which joint angles the singularity might occur, we have to find when the Jacobian matrix has not full rank, in this case < 3. A square matrix has full rank when its determinant is not zero. In case of redundant mechanism the Jacobian matrix is rectangular (in our case [3x4]) and its determinant cannot be found. To define when the rectangular matrix has deficient rank, the properties of the rank and the determinant are considered. Since the matrix is composed of real values, following equality is true:

$$\operatorname{rank}(\mathbf{A}) = \operatorname{rank}(\mathbf{A}\mathbf{A}^T). \tag{2.11}$$

For the rectangular matrix, the term $\mathbf{A}\mathbf{A}^T$ is a square matrix. Thus, $\det(\mathbf{A}\mathbf{A}^T)$ defines whether the rank of the matrix $\mathbf{A}$ is deficient.

Having the Jacobian (2.10) and applying the trigonometric identities, the determinant of $\mathbf{J}\mathbf{J}^T$ is following:

$$\det(\mathbf{J}\mathbf{J}^T) = 2\left(1 - \cos(q_2)^2 \cos(q_3)^2\right) \tag{2.12}$$

Setting the right-hand part of the equation (2.12) to zero, values q_2 and q_3 which lead to rank deficiency of $\mathbf{J}$ are found:

$$1 - \cos(q_2)^2 \cos(q_3)^2 = 0 \tag{2.13}$$

Solution of (2.13) gives:

$$\left[\begin{array}{l} q_2 = \pi n, n \in \mathbb{N} \\ q_3 = \pi n, n \in \mathbb{N} \end{array}\right. \tag{2.14}$$

Correctness of (2.14) can be checked by substituting obtained angles in (2.10) that gives:

$$\mathbf{J}(q_1, \pi, \pi) = \begin{bmatrix} 0 & s_1 & 0 & s_1 \\ 0 & -c_1 & 0 & -c_1 \\ 1 & 0 & 1 & 0 \end{bmatrix} \tag{2.15}$$

From (2.15) can be easily seen, that 1st and 3rd columns, as well as 2nd and 4th columns, are linearly dependent and the maximum rank of $\mathbf{J}$ is no more then 2 that shows the rank deficiency of the matrix and, consequently, a singular configuration of the gimbal.

The redundancy of the robotic gimbal can be used to avoid singularity. To this end, the concept of task decomposition proposed by Yoshikawa [107] is employed in the control algorithm. There are two tasks, which shall be distinguished for the robotic gimbal: the first task is to track the desired end effector trajectory; the second task is to avoid singularities. The general solution for (2.9) is given by:

$$\dot{\mathbf{q}} = \mathbf{J}^{+}\dot{\mathbf{q}}^{*} + \left(\mathbf{I} - \mathbf{J}^{+}\mathbf{J}\right)\dot{\mathbf{q}}_{\mathbf{0}}, \tag{2.16}$$

where $\mathbf{I}$ is the [4x4] identity matrix, $\mathbf{J}^{+}$ is the Moore-Penrose pseudoinverse of the Jacobian matrix defined as $\mathbf{J}^{+} = \mathbf{J}^{T}\left(\mathbf{J}\mathbf{J}^{T}\right)^{-1}$ and $\dot{\mathbf{q}}_0$ is an arbitrary joint velocity vector. The operator $\mathbf{I} - \mathbf{J}^{+}\mathbf{J}$ projects $\dot{\mathbf{q}}_0$ in the null space of $\mathbf{J}$, so that this term generates only internal motion of the robot and does not change the end-effector posture. The first term in the right hand part of (2.16) is the simple pseudoinverse control law that corresponds to the first task, while the second term represents the redundancy left after completing the first task.

A typical function to set $\dot{\mathbf{q}}_0$ in case of singularity avoidance is [108]:

$$\dot{\mathbf{q}}_{\mathbf{0}} = k_0 \left(\frac{\partial w(\mathbf{q})}{\partial \mathbf{q}}\right)^{T}, k_0 > 0 \tag{2.17}$$

where w is manipulability measure defined as:

$$w(\mathbf{q}) = \sqrt{\det(\mathbf{J}\mathbf{J}^{T})} \tag{2.18}$$

In other words, (2.17) and (2.18) tend to keep the ability of manipulation as much as possible, when the main task (desired trajectory tracking) is performed.

The inverse kinematics algorithm is illustrated in Figure 2.2-6. Since the end effector trajectory includes only rotations, the desired rotation matrix $\mathbf{R}_d$ is considered as input. The operator $F_{\Delta R}$ is used to define the orientation error between $\mathbf{R}_d$ and the real end effector orientation $\mathbf{R}$, as it is proposed in [109]:

$$F_{\Delta R}(\mathrm{R}, \mathrm{R}_d) = \mathbf{R}_d\left(\ln\left(\mathbf{R}^{-1}\mathbf{R}_d\right)\right)^{\vee}, \tag{2.19}$$

where $\left(\ln\left(\mathbf{A}\right)\right)^{\vee}$ is logarithmic map operator, defined as following:

$$\left(\ln\left(\mathbf{A}\right)\right)^{\vee} = \begin{cases} \begin{bmatrix} 0 & 0 & 0 \end{bmatrix}^{T}, & \text{if } \mathbf{A} = \mathbf{I} \\ \dfrac{\phi}{2\sin\phi}\begin{bmatrix} a_{32} - a_{23} \\ a_{13} - a_{31} \\ a_{21} - a_{12} \end{bmatrix}, & \text{if } \mathbf{A} \neq \mathbf{I} \end{cases} \tag{2.20}$$

and

$$\phi = \cos^{-1}\left(\frac{\mathrm{trace}\left(\mathbf{A}\right) - 1}{2}\right) \tag{2.21}$$

The operator F_{qq0} realizes (2.17) and (2.18).

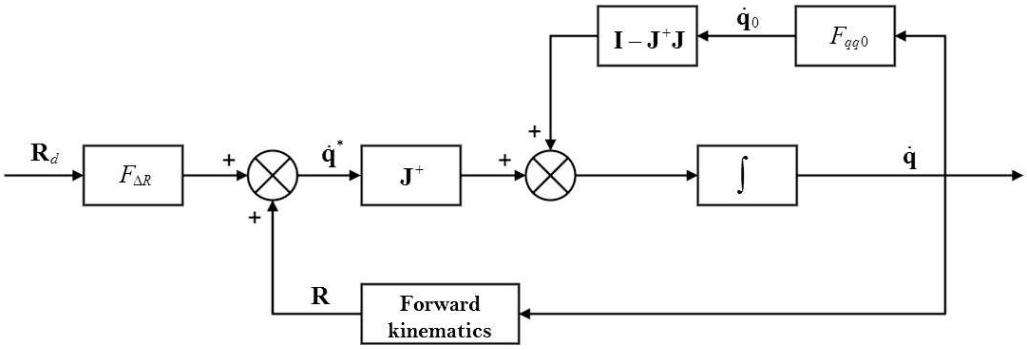

Figure 2.2-6 Inverse kinematics algorithm for the 4 DoF robotic gimbal

2.2.4 Measurement system

For the proper AirBall performance, the parts of the air bearings must be always aligned. Thus, the desired rotation matrix $\mathbf{R}_d$ has to be formed based on actual data about the Inner Sphere orientation. As the main goal of the ADCS tests is to study the natural dynamics of the CubeSat, which might depend on unknown factors, the motion of the Inner Sphere cannot be predicted.

Common solution for this task consists in using different kinds of vision systems (3D, 2D, acoustic, IR) [110]–[114] or IMU [115], [116]. However, these approaches are not sufficient enough for certain applications. In the framework of the AirBall testbed development, the rigid body angular orientation determination should be dealt with taking into account the following constraints:

- Fine accuracy;
- No wiring between the rotating rigid body and the fixed base;
- Enough speed to use resulting data in real time control;
- Minimum elements attached to the observed body;
- Low cost of the overall system.

Analysis of the aforementioned solutions has shown that they do not satisfy these criteria. Motion capture cameras either are not accurate enough, or require bulky and sometimes wired markers. Precise vision systems are quite expensive. IMU need to be placed directly on the observed body and be wired to the fixed base. Otherwise, IMU shall be equipped with an autonomous power source and a transmitter that results in non-negligible mass attached to the body [117].

An alternative technique to acquire the information about the Inner Sphere orientation is proposed in order to better match constrains above. This technique employs sensors to measure linear distances between certain points on the Inner and Outer Spheres. Thus, the knowledge of the orientation is obtained by means of indirect measurements. Two variations of this approach are developed; they differ in the measurement methods (with and without a reference target) and in the number of required measurements.

The target-free method involves the distance sensors mounted on the air bearings. There are four pairs of the air bearing passive and active parts onto the testbed and each of them can be equipped with two distance meters to estimate the center of each air bearing passive element, as shown in Figure 2.2-7. While the Inner and Outer Spheres are considered as rigid bodies and the CubeSat is considered to rotate around a fixed center, only two pairs of distance meters are enough to determine the current orientation of the CubeSat. The two other pairs are used to improve accuracy of the measurements and avoid a possible particular case (rotation around the axis of one of the observed air bearing).

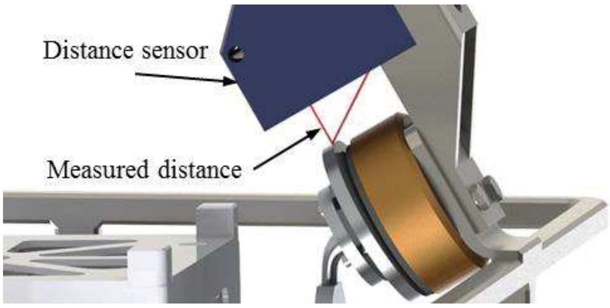

Figure 2.2-7 Air bearing with a micro distance sensor (only one shown)

The three sensors method requires a reference target, with respect to which distance sensors make measurements. The regular Y-shape has been chosen to be the reference. The key idea of this approach is to deal with the determination of a body orientation by means of 3 distance meters, the minimum number of measurements required to define a 3 DoF orientation, and obtain linear equations using the small angle approximation.

Detailed discussions of the approaches proposed for the use in the testbed measurements systems are is given in Section 3.3.

2.2.5 Discussions on the design

The overall structure of the AirBall testbed presented in Figure 2.2-8 comprises some elements, which have been developed from scratch, and their performance has to be verified. Feasibility of several concepts has to be checked before they are implemented in the testbed:

- Air bearings assembled in a sphere

The concept of the rotating air bearing sphere is new and it requires some theoretical and experimental studies. The behavior of the air bearings is a complex process that depends not only on the bearings orientation and applied loads, but also on aerodynamics. In the literature, there is no available information about the spherical air bearings involved in the systems as AirBall. Thus, there are certain concerns about their performance as a part of the air bearing sphere: (i) normal and tangential lift force of the air bearing as function of the tilt angle; (ii) stiffness as a function of tilt angle; (iii) disturbances caused by the air flow when the active and passive parts of the air bearings are not perfectly aligned.

- Mass balancing system

Mass balancing is a key technique allowing low-torque environment simulations. The required level of the acceptable disturbance torques on the testbed (Table 4) is highly demanding, thus, the performance of both the balancing algorithm and the mechanical part shall be tested in order to verify its compliance with the requirements.

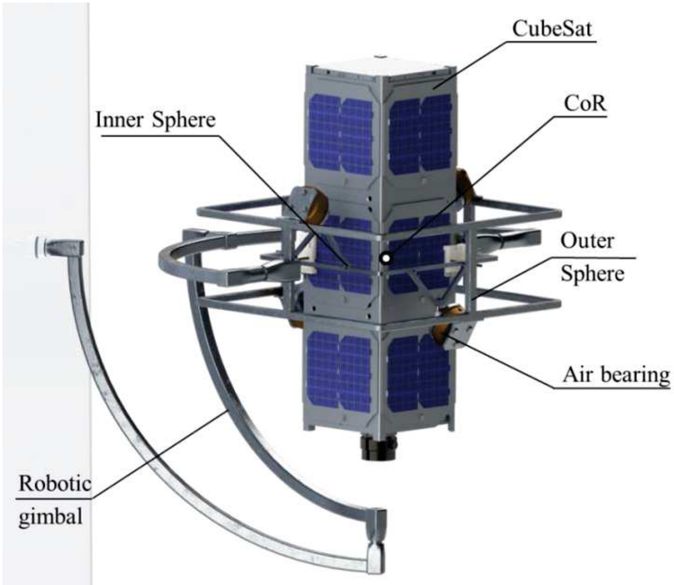

Figure 2.2-8 AirBall testbed

- Measurement system

The proposed approach to the contactless measurement of the CubeSat orientation is different from methods that typically used for such purposes. So, verifications of the measurement method in terms of efficiency and robustness are a subject of the preliminary experimentation work.

Thus, the prototype of the testbed with reduced performance was intended to be built in order to verify performance of the essential testbed elements mentioned above. It will help to diminish the risk of failures and to simplify the analysis of probable malfunctions.

2.3 AirBall prototype and employed components

2.3.1 Configuration

In comparison with the AirBall testbed design described in details previously in this chapter, the prototype includes several modifications. The chart flow in Figure 2.3-1 illustrates the subtasks, which have been handled to develop the prototype. Some steps of the development process, mostly related to the hardware part, are discussed below, while others are detailed in Chapter 3.

Modifications accepted in the prototype design are aimed to simplify its structure and reduce the development expenses. Thus, it was decided to replace the newly designed robotic gimbal with a 6 DoF robotic arm available in the laboratory. The CubeSat and its adjustment mechanism were interchanged with a CubeSat mock-up rigidly fixed to the Inner Sphere. These changes certainly influence the functionality of the system:

- While having two excessive DoF, the geometry of the involved articulated robot is not optimal for the current task so that it constrains the motion of the Outer Sphere;

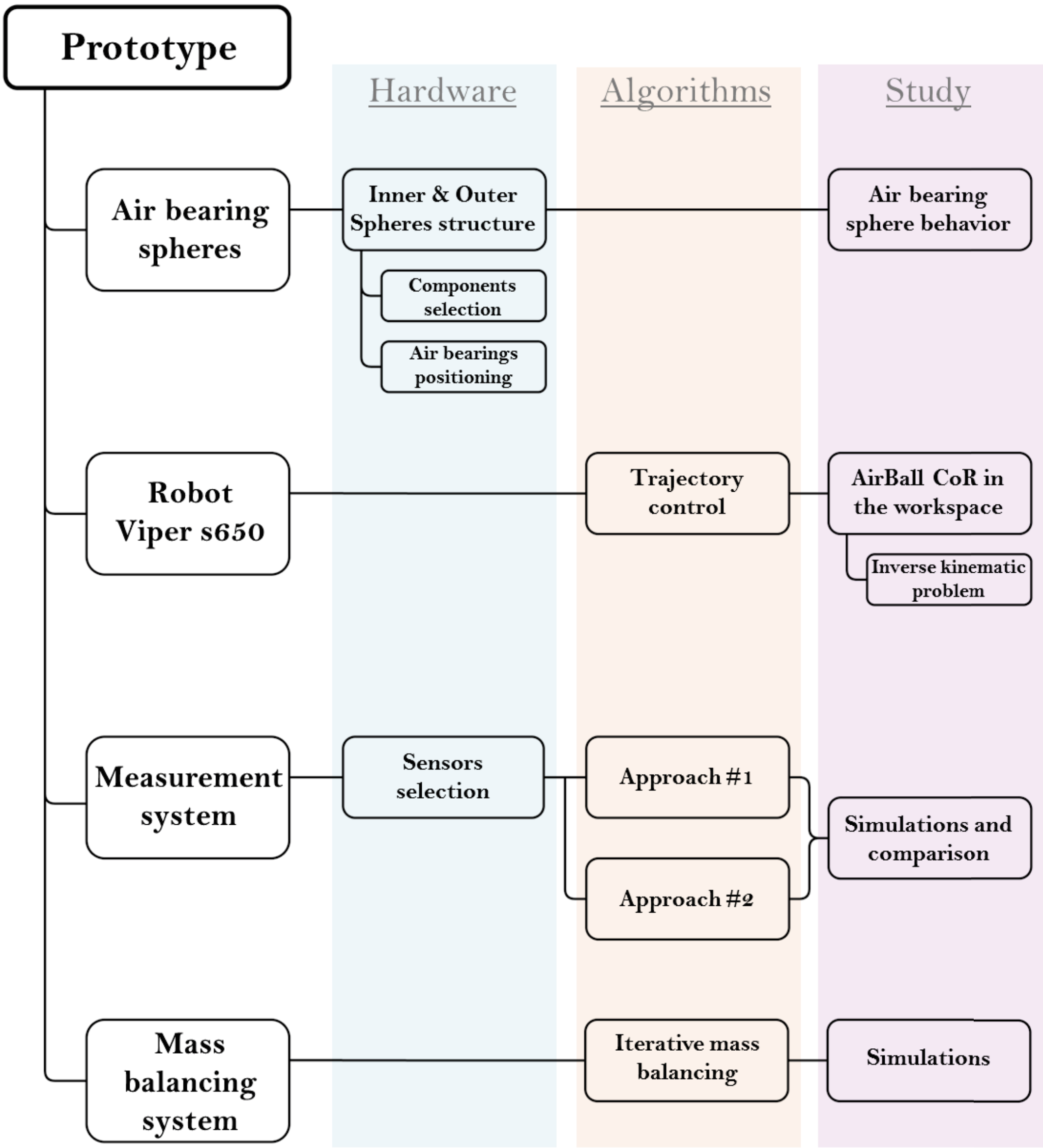

Figure 2.3-1 Chart flow of the AirBall prototype development

- The Inner Sphere CoM position is adjusted by shifting small masses, but not by moving the CubeSat. Thus, the CubeSat adjustment mechanism shall be tested separately.

2.3.2 Air bearing Spheres with CubeSat mock-up

The spherical porous media air bearings were purchased from New Way Air Bearings to be used in the prototype. They are accompanied with ∅40 mm light spherical caps designed specifically for this project. At first, the active parts of the air bearings have been selected to be same diameter as the passive part. However, in this case, the acceptable range of misalignments between the parts of the air bearing is very narrow that causes some difficulties for the implementation of the desired experimental works. The active parts with smaller diameter (∅25 mm) have been selected as a replacement, because of this issue. All characteristics of the employed air bearings are presented in Table 6.

The air bearings performance is greatly affected by the shape and dimensions tolerance of the structure. The nominal air bearing fly height is 5 μm and this value defines the required sphericity tolerance of the Inner and Outer Sphere. Difference of the Spheres diameters shall be within 10-50 μm. The larger difference of the diameters will cause significant translations of the Inner Sphere inside the Outer Sphere while they rotate. Thus, the structure of the Spheres has to allow accurate positioning for four air bearings, considering both distances from CoR (Figure 2.3-2, center) and concentricity (Figure 2.3-2, right), so that all four of them belong to one sphere. This requirement is very demanding, considering the tolerances.

Table 6 Spherical porous media air bearings

	Diameter, mm	Radius of the sphere, mm	Load at 5μm fly height, N	Stiffness, N/μm	Air flow, SLPM	Mass, g
S3625	40	120	49	18	1.04	14
S3640	25	120	178	28	1.79	35

Analyzing the geometry of the Spheres, it is easy to see, that the shape of the desired virtual sphere with its center at certain CoR is over constrained by the air bearings, when they are rigidly fixed to the frames. Indeed, three points in space are enough to define a sphere, but in the given system each of four air bearings is secured in place with 3 points at least, that gives 12 linkages in total (Figure 2.3-3, left). Thus, a position of every air bearing is obliged to be adjusted with enormous precision that affects the cost of the system. In order to deal with this issue, number of constrains of the Outer Sphere must be reduced. To this end, it was decided to use spherical joints to keep the active parts of the air bearings in place, as result, there are only 4 constraints left (Figure 2.3-3, right). In this case angular tilt of the active part is able to get adapted to the orientation of the corresponding passive part, so that the possible inaccuracy of the Inner Sphere shape does not cause the critical misalignment. Additionally, one of the joints has a spring along its axis. This solution helps to deal with the last exceeding constraint and allows one of the air bearings to adjust its distance from CoR to match the sphere built of three fixed bearings. Detailed discussions on the using a spring for the air bearing fastening are given in Section 3.1.

Thus, it was decided that the passive parts of the air bearings are rigidly fixed to the frame of the Inner Sphere with available precision. Meanwhile, being connected to the frame of the Outer Sphere, the active parts have some freedom to adjust themselves to the Inner Sphere. Due to this solution, possible inaccuracy of the passive parts positioning is compensated by means of the active parts placing.

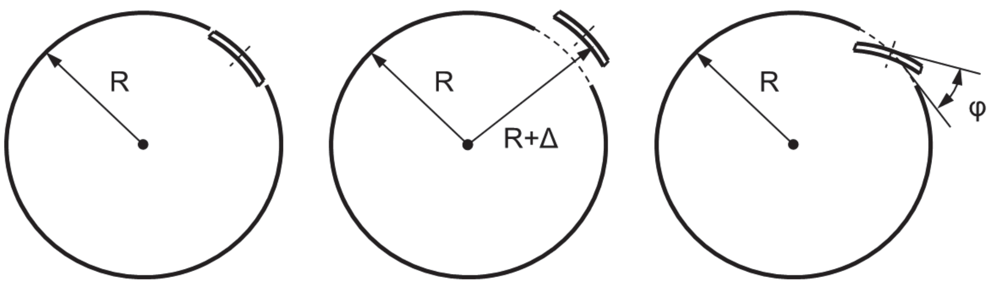

Figure 2.3-2 Correct position of an active part of the air bearing (left) and its misalignment due to distance from CoR (center) and non-concentricity (right)

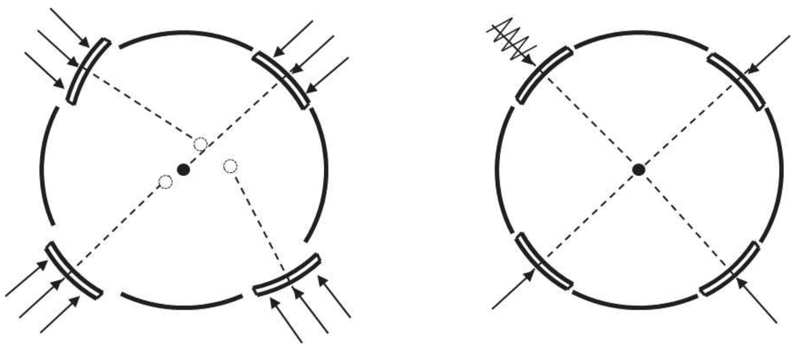

Figure 2.3-3 Sphere constrained by the air bearing linkages

In order to reduce the prototype assembling and adjustment requirements, the CubeSat mock-up is made to be an essential part of the Inner Sphere frame, so that it impossible to remove or to shift it. Obviously, this design solution cannot be implemented on the testbed, but it is suitable for the prototype. The technique of the mass balancing in this case must be reconsidered: The CoM translation is provided by means of 6 small shifting masses. This does not require significant changes in the mass balancing algorithm (Section 3.4), while it was initially designed to be used with the CubeSat position adjustment mechanism.

The elements required for the CubeSat orientation identification, which are 3 laser distance sensors purchased from Keyence, the light 3D printed target for measurements and its counterweight, are installed in their places. While the Inner Sphere of the AirBall prototype does not have a detached supporting frame, the target and counterweight are fixed directly to the CubeSat mock-up.

The AirBall prototype (Figure 2.3-4), comprising the CubeSat mock-up, Inner and Outer Spheres, was manufactured and assembled by Symétrie.

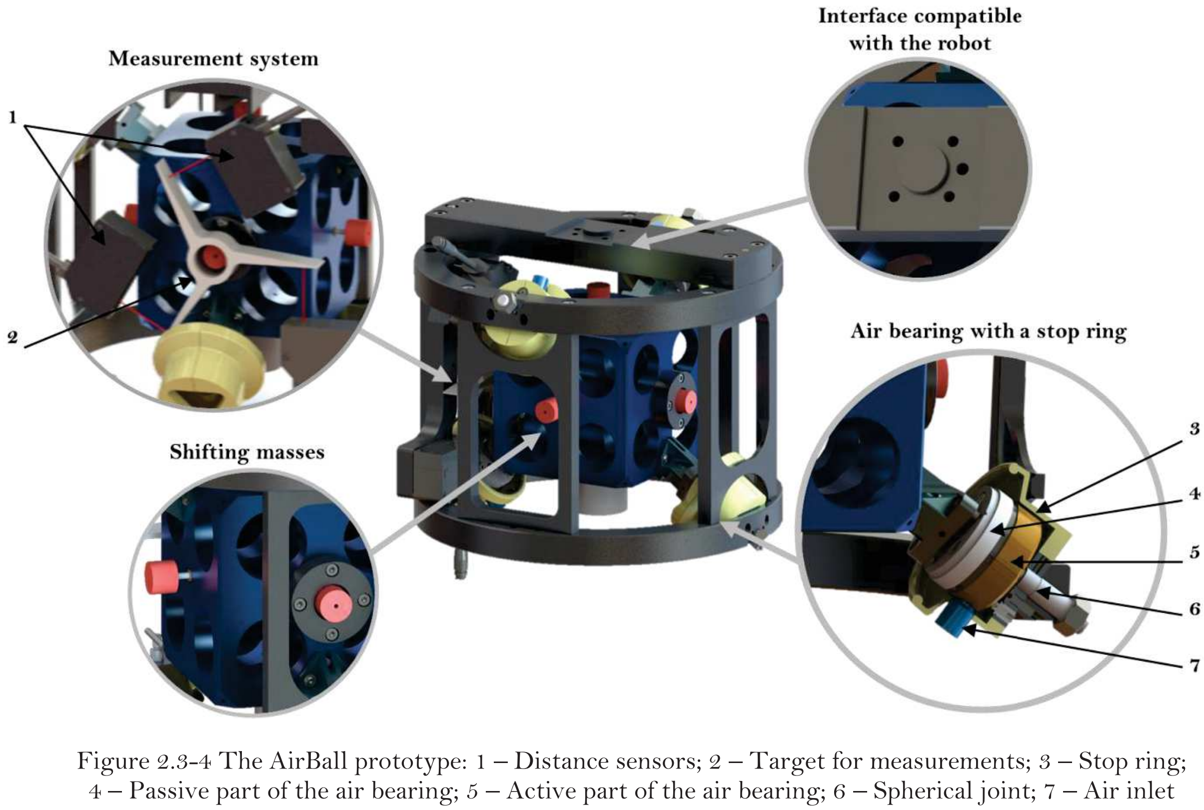

Figure 2.3-4 The AirBall prototype: 1 – Distance sensors; 2 – Target for measurements; 3 – Stop ring; 4 – Passive part of the air bearing; 5 – Active part of the air bearing; 6 – Spherical joint; 7 – Air inlet

2.3.3 Adept Viper s650

The Adept Viper s650 is a 6 DoF articulated robot designed for applications such as assembly, material handling, packaging, machine tending and other operations that require fast and precise automation [118]. In this project the Viper s650 is involved to hold the AirBall External Sphere that follows rotation of the Inner Sphere. The most important for this task information from the Viper specification is presented in Table 7.

As it was described earlier, the center of the Spheres is static and the External Sphere has only rotational degrees of freedom. The most suitable robot to perform this task would be a spherical wrist (as that proposed in Section 2.2.3) that has all joint axes intersected at one point. Having only 4 DoF such wrist can provide unconstrained rotation of the External Sphere. However, the 6 DoF Viper robot cannot allow a full turn of the External Sphere due to its anatomy. Indeed, the work envelope of the Viper (Figure 2.3-5) is large enough to embrace the AirBall prototype attached to its end effector, but the required orientation of the end effector shall be taken into consideration. In order to support rotation of the External Sphere around the fixed CoR, the robot's end effector must keep J6 axis pointed at the CoR. For this task all 6 DoF must be engaged and still there are some sectors of the sphere, which are unattainable for the robot. The unattainable area depends on the position of the External Sphere CoR in the Viper workable space.

Table 7 Adept Viper s650 specification

Motion range	Maximum joint speed	Maximum composite speed	Position repeatability	Maximum payload	Maximum allowable MoI
J1 ±170° J2 -190°, +45° J3 -29°, +256° J4 ±190° J5 ±120° J6 ±360°	J1 328°/sec J2 300°/sec J3 375°/sec J4 375°/sec J5 375°/sec J6 600°/sec	8200 mm/s	±0.02 mm	5 kg	Around J4 and J5 0.295 kgm² Around J6 0.045 kgm²

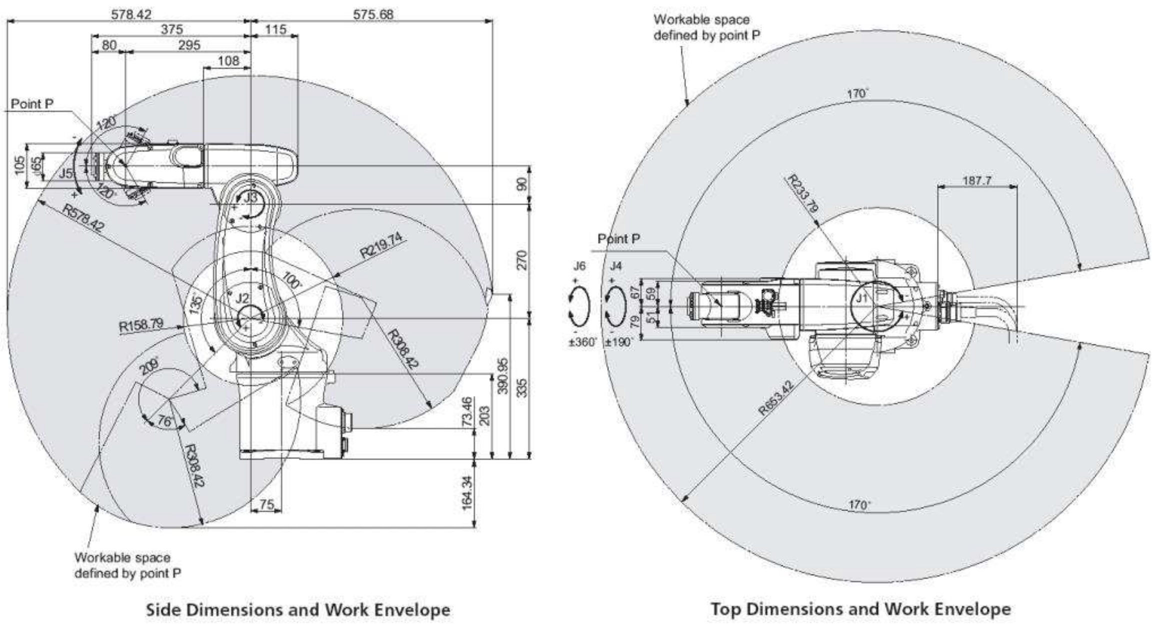

Figure 2.3-5 Viper s650 anatomy and work envelope [118]

2.3.3.1 Position for the External Sphere CoR in the work envelope

In order to reduce the unattainable area, an exhaustive search of the most convenient CoR position was done. Analysis of the work envelope in only one plane is enough, because the workable space is transversely isotropic around the $\mathbf{z}_6$ axis. The work envelope of the Viper robot is divided into smaller sections with a constant step (100 mm). Every node of the acquired grid is considered as a possible CoR of the AirBall. A number of points evenly spread on the sphere with a center at the presumed CoR are examined in order to find whether they can be reached by the robot end effector. For every point P_i on the sphere, the transformation matrix $\mathbf{T}_{des\_i}$ of the desired end effector pose is computed so that the $\mathbf{z}_6$ axis is pointed at the CoR. If at least one admissible solution of the inverse kinematics problem exists for the desired end effector pose denoted by $\mathbf{T}_{des\_i}$, it is concluded that the point P_i can be achieved by the Viper. Then, next point P_{i+1} on the sphere is studied following the same steps as they are shown on the scheme in Figure 2.3-6.

Being given the knowledge of the existence of the Viper postures for all selected points of the sphere, the attainable area is calculated as the ratio of admissible points to all selected points. Then the next node of the grid is picked to be studied.

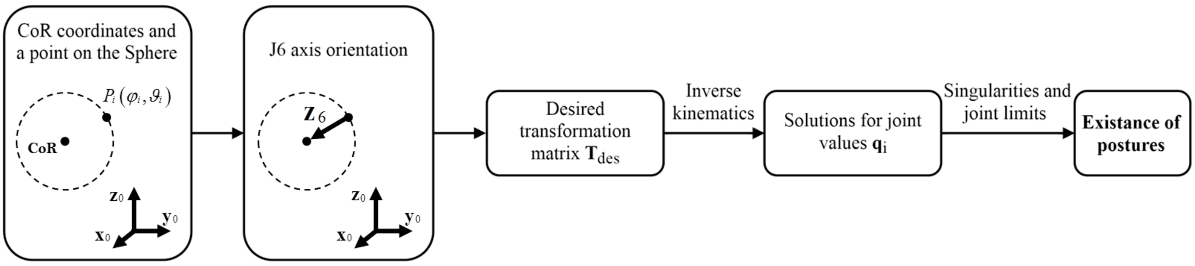

Figure 2.3-6 Selected point on the sphere with its center at the desired CoR is examined to find the inverse kinematics solutions for the corresponring end effector posture

It is convenient to select the CoR position that yields the maximum possible ratio of the attainable area. Besides that, two other criteria are considered:

- The area shall be continuous;
- Upper hemisphere is preferable.

Thus, after the analysis of the number of the points preselected in the work envelope, the area most convenient for CoR location is defined. Within this area one point with coordinates [435, 0, 94] is selected as the CoR of the AirBall. The attainable area featured by this point is shown in Figure 2.3-7.

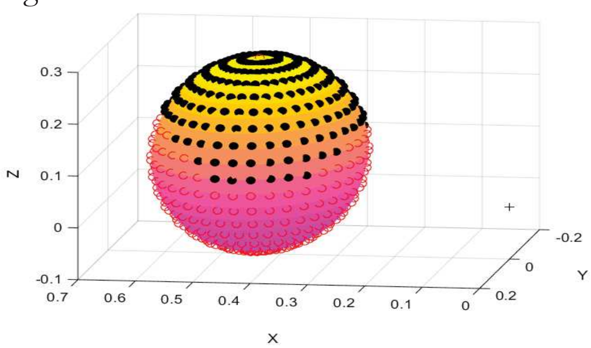

Figure 2.3-7 Attainable area (black dots) of the sphere with a center at coordinates [435, 0, 94]

2.3.3.2 Inverse kinematics problem

The solution for the inverse kinematics problem has to be found in order to determine joint variables corresponding to the desired end effector pose. It is an essential step in the exhaustive search for the optimal CoR position in the Viper work envelope. Typically Denavit–Hartenberg parameters are used to describe the robot geometric structure in kinematic calculations, but this notation is not unique. Thus, the geometry based technique proposed in [119] was implemented to describe the robot structure. With a strong focus on practicability, it allows easy and rapid calculating both the forward and inverse kinematics. Only seven parameters, called OPW-parameters, are needed to describe an ortho-parallel basis with a spherical wrist. Using them, the analytical solution for the inverse kinematic problem can be obtained. At first, solutions for the ortho-parallel substructure are calculated. To this end, the desired position of point C (in Figure 2.3-8) has to be known.

Being given the transformation matrix $\mathbf{T}_{des}$ composed of a position vector $\mathbf{t}_{des}$ and a rotation matrix $\mathbf{R}_{des}$, such that

$$\mathbf{R}_{des} = \begin{bmatrix} r_{11} & r_{12} & r_{13} \\ r_{21} & r_{22} & r_{23} \\ r_{31} & r_{32} & r_{33} \end{bmatrix}, \tag{2.22}$$

the desired position of point C is calculated below:

$$\mathbf{p}^T = \mathbf{t}_{des}^T - c_4 \mathbf{R}_{des} \begin{bmatrix} 0 & 0 & 1 \end{bmatrix}^T \tag{2.23}$$

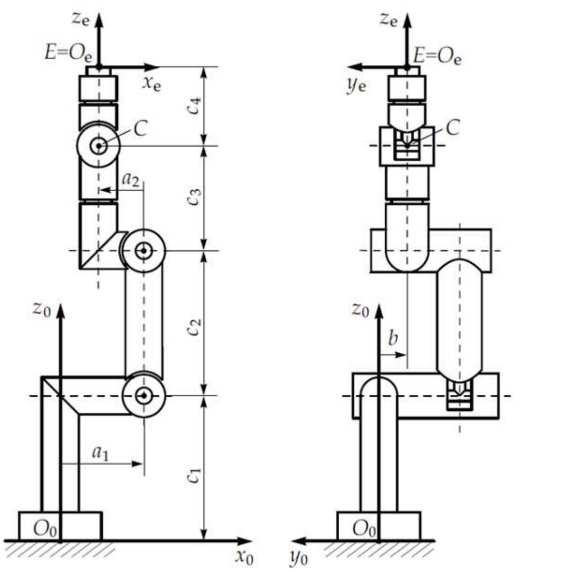

Adept Viper s650 OPW-parameters, mm	
a_1	75
a_2	-90
b	0
c_1	335
c_2	270
c_3	295
c_4	80

Figure 2.3-8 6 DoF manipulator geometry described by the OPW-parameters [119] and table of those for the Adept Viper s650

Then using geometrical representation of the substructure postures, four possible solutions of the inverse kinematics problem are found. The joint values for the ortho-parallel basis are given below:

$$\begin{aligned} q_{1(1)} &= \operatorname{atan2}(p_2, p_1) - \operatorname{atan2}(b, n_1 + a_1), \\ q_{1(2)} &= \operatorname{atan2}(p_2, p_1) - \operatorname{atan2}(b, n_1 + a_1) - \pi \end{aligned} \tag{2.24}$$

$$
\begin{aligned}
q_{2(1,2)} &= \mp\arccos\left(\frac{c_2^2+n_2^2-n_4^2}{2n_2c_2}\right)+\operatorname{atan2}\left(n_1, p_3-c_1\right),\\
q_{2(3,4)} &= \mp\arccos\left(\frac{c_2^2+n_3^2-n_4^2}{2n_3c_2}\right)-\operatorname{atan2}\left(n_1+2a_1, p_3-c_1\right)
\end{aligned}
\tag{2.25}
$$

$$
\begin{aligned}
q_{3(1,2)} &= \mp\arccos\left(\frac{-c_2^2+n_2^2-n_4^2}{2n_4c_2}\right)-\operatorname{atan2}\left(a_2, c_3\right),\\
q_{3(3,4)} &= \mp\arccos\left(\frac{-c_2^2+n_3^2-n_4^2}{2n_4c_2}\right)-\operatorname{atan2}\left(a_2, c_3\right)
\end{aligned}
\tag{2.26}
$$

For simplification in the equations (2.24) – (2.26), the following notations are used:

$$
\begin{aligned}
n_1 &= \sqrt{p_1^2+p_2^2-b^2}-a_1,\\
n_2^2 &= n_1^2+\left(p_3-c_1\right)^2,\\
n_3^2 &= \left(n_1-2a_1\right)^2+\left(p_3-c_1\right)^2,\\
n_4^2 &= a_2^2+c_3^2
\end{aligned}
\tag{2.27}
$$

Using the four previously obtained solutions for the positioning part, the joint angle of the spherical wrist are calculated as following:

$$
\begin{aligned}
q_{4(j)} &= \operatorname{atan2}\left(r_{23}\hat{c}_{1(j)}-r_{13}\hat{s}_{1(j)}, r_{13}\hat{c}_{23(j)}\hat{c}_{1(j)}+r_{23}\hat{c}_{23(j)}\hat{s}_{1(j)}-r_{33}\hat{s}_{23(j)}\right),\\
q_{4(k)} &= q_{4(j)}+\pi
\end{aligned}
\tag{2.28}
$$

$$
\begin{aligned}
q_{5(j)} &= \operatorname{atan2}\left(\sqrt{1-m_{(j)}^2}, m_{(j)}\right),\\
q_{5(k)} &= -q_{5(j)}
\end{aligned}
\tag{2.29}
$$

$$
\begin{aligned}
q_{6(j)} &= \operatorname{atan2}\left(r_{12}\hat{s}_{23(j)}\hat{c}_{1(j)}+r_{22}\hat{s}_{1(j)}\hat{s}_{23(j)}+r_{32}\hat{c}_{23(j)}, -r_{11}\hat{s}_{23(j)}\hat{c}_{1(j)}-r_{21}\hat{s}_{23(j)}\hat{s}_{1(j)}-r_{31}\hat{c}_{23(j)}\right),\\
q_{6(k)} &= q_{6(j)}-\pi
\end{aligned}
\tag{2.30}
$$

where

$$
\begin{aligned}
&j=\{1,2,3,4\},\ k=\{5,6,7,8\}\\
&m_{(j)} = r_{13}\hat{s}_{23(j)}\hat{c}_{1(j)}+r_{23}\hat{s}_{23(j)}\hat{s}_{1(j)}+r_{33}\hat{c}_{23(j)},\\
&\hat{c}_{1(j)} = \cos\left(q_{1(j)}\right),\ \hat{c}_{23(j)} = \cos\left(q_{2(j)}+q_{3(j)}\right),\\
&\hat{s}_{1(j)} = \sin\left(q_{1(j)}\right),\ \hat{s}_{23(j)} = \sin\left(q_{2(j)}+q_{3(j)}\right),
\end{aligned}
\tag{2.31}
$$

Thus, there are eight possible solutions for the inverse kinematics problem stated in (2.24) – (2.31), but number of admissible solutions can be reduced by the kinematic singularities and mechanical joint limits. There are two possible singular configurations of the Viper, they are caused by the alignment of joints J1 and J6 or J4 and J6. The mechanical joint limits are indicated in Table 7.

2.3.4 Summary

The prototype of the AirBall testbed is designed in order to verify functionality of the key systems as integral parts of the air bearing based platform. The prototype structure comprises the AirBall Spheres, which include with 4 air bearings and the CubeSat mock-up, three laser distance sensors and the Adept Viper s650 robot. The 3D prototype model is shown in Figure 2.3-9. Being compared with the testbed concept, the prototype features several functional constraints. They are caused by the simplified design of the Inner Sphere and the use of the robot, which geometry is not optimized for the assigned task.

Summarizing all the changes of the previously defined testbed performance, the AirBall prototype allows following functions:

- 1U CubeSat mock-up is accommodated (a bigger CubeSat does not match the maximum allowable payload of the Viper s650);
- Free CubeSat rotation in roll axis and the rotational freedom in yaw and pitch axes constrained to ±25° and ±45°, respectively;
- Manual mass balancing system, CoM position is adjusted by moving 6 small shifting masses;
- Measurement system to find CubeSat orientation in real time is contactless, but requires a target fixed to the Inner Sphere structure;
- Added MoI is below 50% of 1U CubeSat (including the Inner Sphere structural elements, the target for measurements and its counterweight);

Total disturbing torque induced by the testbed prototype is to be defined in the experimentations.

Figure 2.3-9 The AirBall prototype comprising the Inner and Outer Spheres with 4 air bearings, 3 laser sensors and 1U CubeSat mock-up, and the Adept Viper s650

2.4 Conclusion

In this chapter the search for a new concept of the air bearing testbed was done. The testbed shall allow improvements of the functionality, namely, the enlargement of the CubeSat rotational freedom while having the same level of residual disturbance torques. Three approaches have been discussed: The dynamic compensation of the additional MoI; the air-levitated whole sphere; and the sphere built of 4 small air bearings, called AirBall. The first of the approaches is based on providing the CubeSat with unconstrained rotation by means of the gimbal mechanism. It intends to compensate the large MoI of the mechanism by the motors in the gimbal joints. The second approach can be considered as a natural next step of the air bearing platform evolution: The classical table, which has a hemisphere in the base, is replaced by a full hollow sphere. This yields the unrestricted rotation of the CubeSat lodged in the center of the sphere. However, this design solution yields large added MoI that cannot be compensated or eliminated. The AirBall is a fusion of the other two approaches. The CubeSat is accommodated by the structure built of several small air bearing. They are aligned in such a way that their surfaces form a common sphere. The part of the structure, called the Inner Sphere, holds the CubeSat and the passive parts of the air bearings. The Outer Sphere supports the active parts of the air bearings. The robotic gimbal is involved to rotate the Outer Sphere so that it follows the Inner Sphere motion and parts of the air bearings are aligned by two. This concept of the air bearing testbed was selected for implementing as the most feasible and promising one.

The AirBall concept has some design solutions, which were not tested before. Thus, the air bearings assembled in one rotating sphere were not described in any literature known for the author and they behavior is difficult to intuitively predict. It was decided to build a prototype of the AirBall testbed, which allows experimental verification of the selected concept. The prototyping causes several limitations of the initially promoted testbed performance. That is explained by two factors: The simplification of the Inner Sphere design; and the use of the Adept Viper s650 manipulator. This robot is available at the laboratory, but its geometry is not optimal for the assigned task. These changes in the AirBall design allowed to decrease time and expenses required for the prototyping stage.

Besides the prototype design, there are several problems that have to be studied for the successful experimentations, which are:

- Behavior of the sphere built of the air bearings;
- A mass balancing technique;
- Determination of the CubeSat orientation.

Chapter 3 is dedicated to solve the aforementioned problems.

Chapter 3. AIRBALL MODELING

3.1 INTRODUCTION

The AirBall testbed for CubeSat ADCS and its prototype are designed to provide an extended range of operation angles and an acceptable level of disturbance torques. These features require implementation of some design solutions and techniques that have been developed within the research of this thesis and have to be checked by modeling prior to experimental works.

The air bearing Spheres are an essential part of the testbed and its prototype. Their design is based on a completely new approach to the application of spherical air bearings and their assembling is very sensitive to the imprecisions of the elements. Thus, a study of the Spheres (Section 3.2) was undertaken to learn the behavior of the presented configuration of the air bearing assembly and to find a permissible range of the dimension tolerances.

The measurement system dedicated to the determination of the CubeSat orientation was designed to match the precision and budget constraints. Two approaches to implement the laser distance sensors are developed. The simulations used to evaluate efficiency of these approaches and to compare their pros and cons are presented in the Section 3.3.

The designed testbed is intended to provide a low-torque environment. One of the disturbing torques is caused by the gravity force, when the center of mass (CoM) of the rotating body and the center of rotation (CoR) are misaligned. In order to lower an effect from this torque, the mass balancing is essential. A technique developed for the manual mass balancing is discussed in the Section 3.4 and is illustrated with results obtained from the modeling.

3.2 AIR BEARING SPHERES BEHAVIOR STUDY

Air bearings are widely used in different engineering applications, such as measuring and precision machines, space-oriented facilities, and other clean room, high speed, and precise applications. Air bearings allow zero static and minimized dynamic friction, zero wear, silent and smooth operation, high speed and high acceleration. In satellite testbeds, air bearings are chosen primarily because of reduced friction that allows free rotation of the structure containing the satellite and leads to realistic simulation of the satellite dynamics in space.

One of the concerns about air bearings is their stiffness. They provide high dynamic stiffness, which however depends on the lift force. The theoretical plot of the lift force as function of the payload fly height for the air bearing selected for the AirBall is shown in Figure 3.2-1. It has been identified on the statistical data of air bearings and the local stiffness value taken from the data sheet of the chosen air bearing. The curve is nonlinear

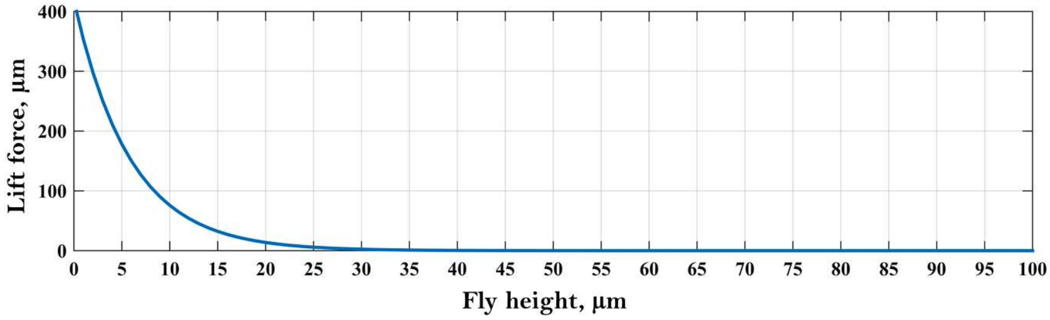

Figure 3.2-1 Fly height – lift force curve for the 40mm porous carbon air bearing. Local slope represents the local stiffness

and as the air film gets thinner the stiffness gets higher. Pressure and surface area both affect stiffness proportionately.

According to the design of the AirBall testbed, the air bearings have some geometrical restrictions. The Inner Sphere is placed inside the Outer Sphere such that the sphere formed by the passive parts of the air bearings is smaller than the one formed by the active parts. For normal operation of the testbed, the Inner Sphere can move inside the Outer Sphere, but the minimum clearance between them shall always be greater than 0 µm, in other words, the Spheres shall not collide. If the air bearing assembly was a complete sphere, the Inner Sphere would fall a little onto the Outer Sphere, till equilibrium for the lift force that counteract the Inner Sphere weight is found. This vertical deviation would be constant, independent from the angular positions of the Spheres. However, the AirBall Spheres are composed of 4 separated air bearings, as described above, and the total lift force of the Outer Sphere onto the Inner Sphere depends on their relative orientation. Thus, the study of the relative Inner Sphere - Outer Sphere motion shall be done. It will help to understand how the size of the clearance between the Spheres affects the character of the CubeSat motion and, consequently, what is the acceptable range of this clearance size.

3.2.1 Assumptions and modelling

The geometry of the air bearing assembly comprises 4 spherical air bearings evenly distributed in space as it was illustrated in Figure 2.2-2. The active parts of the air bearings are mounted on the Outer Sphere by means of spherical joints, thus the linear displacements are constrained while the angular tilts are possible. Due to this fastening system the active parts of the air bearings can be represented by a force directed toward the geometrical center (GC) of the Outer Sphere.

The free body diagram of the Inner Sphere in Figure 3.2-2 is used to represent the geometry described above, where $\mathbf{F}_i$ is the lift force of an air bearing, $\mathbf{u}_i$ is the unit vector directing $\mathbf{F}_i$ (it starts at the center of the air bearing and is pointed towards the center of the Inner Sphere O_{inn}, assuming the lift force is normal to the air bearing passive element), and $\mathbf{u}_i^0$ is the unit vector pointed towards the center of the Outer Sphere O_{out}. Vector $\mathbf{d}$ stands for the displacement vector of O_{inn} with respect to O_{out}. Vector $m\mathbf{g}$ corresponds to the weight of the Inner Sphere.

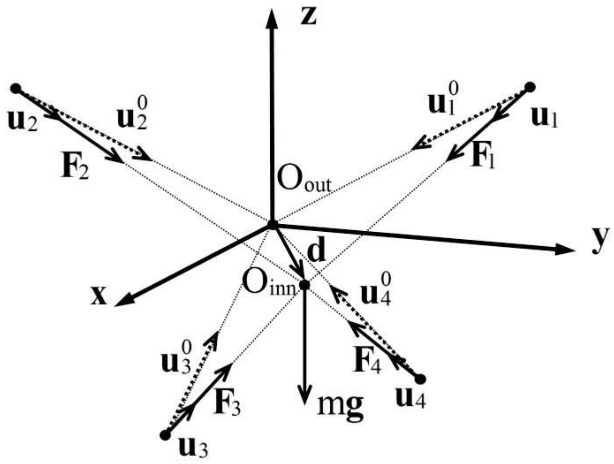

Figure 3.2-2 Free body diagram of the Inner Sphere

In this model, the following assumptions are made:

1. The Inner Sphere is considered to be a rigid body with its GC coincident with its CoM at point O_{inn}.
2. The active and passive parts of the air bearings are mounted at an equal distance from O_{inn} and O_{out}, respectively.
3. Vectors $\mathbf{u}_i$ and $\mathbf{u}_i^0$ are collinear. Indeed, displacement $\mathbf{d}$ is a few orders of magnitude smaller than the radius of the Spheres, that causes negligibly small misalignment of vectors $\mathbf{u}_i$ and $\mathbf{u}_i^0$.
4. As a consequence of Assumption 3, if at any orientation, the Inner and Outer Spheres are not concentric, this does not affect noticeably the direction of the forces generated by the air bearings and they are assumed to be pointed towards O_{out}.
5. The tangent component of the air bearing force is assumed to be negligible compared to the normal component.

Note: Practically, when the Spheres are not concentric, the vector of the force changes its orientation, because it is pointed towards O_{inn} and this might affect the dynamics of the Spheres. Based on further experimentations, Assumption 4 can be changed in the future studies.

Considering the modelled system as quasi-static, the equilibrium of the Inner Sphere is can be written:

$$\sum_{i=1..4} \mathbf{F}_i + m\mathbf{g} = 0 \tag{3.1}$$

As it was shown in Figure 3.2-1, the lift force of the air bearing is a function of the fly height. The shape of the curve is modelled by the exponential function $f(x) = 0.843^x$ based on identification. Thus, the lift force is estimated by:

$$\mathbf{F}_i = F_0 \cdot 0.843^{h_i - 5}\mathbf{u}_i \tag{3.2}$$

where the nominal lift force F_0 is the force at 5 μm fly height (default value from the air bearing data sheet). For the chosen air bearing $F_0 = 178N$; h_i is a fly height along the direction $\mathbf{u}_i$ in μm:

$$h_i = h_a + \mathbf{d} \cdot \mathbf{u}_i \tag{3.3}$$

where h_a is a sphere clearance found as $h_a = r_{out} - r_{inn}$; r_{out} and r_{inn} are radii of the Outer and Inner Spheres (μm) respectively.

Substituting (3.2) - (3.3) into (3.1), the following system of equations is obtained:

$$F_0 \cdot 0.843^{h_a-5}\left(0.843^{\mathbf{d}\cdot\mathbf{u}_1}\mathbf{u}_1 + 0.843^{\mathbf{d}\cdot\mathbf{u}_2}\mathbf{u}_2 + 0.843^{\mathbf{d}\cdot\mathbf{u}_3}\mathbf{u}_3 + 0.843^{\mathbf{d}\cdot\mathbf{u}_4}\mathbf{u}_4\right) + m\mathbf{g} = 0 \tag{3.4}$$

Considering $\mathbf{u}_i(\alpha,\beta,\gamma)$ as a function of three rotation angles α,β,γ, and $\mathbf{d}$ as an unknown vector, the system in (3.4) has 3 equations and 3 unknowns. It contains non-linear (exponential) dependencies that can be linearized in short ranges of h_i. Thus, the usage of a numerical solver is required to obtain the solution of the wider range of h_i.

3.2.2 Mounting with a spring

Since the clearance between the Spheres is of the order of microns, the assembling and setting of the Spheres shall be done very accurately, that might be difficult to achieve. In order to minimize the requirements of setting the Spheres, a spring is used in the mounting of one of the four air bearings on the Outer Sphere. In order to provide translational freedom for this air bearing, a prismatic joint is used in addition to the spherical joint used in the fastening of every active part of the air bearings.

Considering only the Inner Sphere, the free body diagram is similar to that in Figure 3.2-2 and the equation of the equilibrium of the Inner Sphere is (3.1). The forces provided by three rigidly connected active parts of the air bearings $\mathbf{F}_{i=1..3}$ are assigned according to (3.2). Force $\mathbf{F}_4$, associated with the air bearing with a spring, is given by the following equation:

$$\mathbf{F}_4 = F_0 \cdot 0.843^{h_a + \mathbf{d}\cdot\mathbf{u}_4 - h_{sp} - 5}\mathbf{u}_4 \,, \tag{3.5}$$

where h_{sp} is the spring deformation. The corresponding free body diagram is shown in Figure 3.2-3.

Forces $\tilde{\mathbf{F}}_4$ and $\mathbf{F}_4$ have the same amplitude and opposite directions. The spring is modelled as follows:

$$F_{sp} = F_{sp}^0 + kh_{sp} \,, \tag{3.6}$$

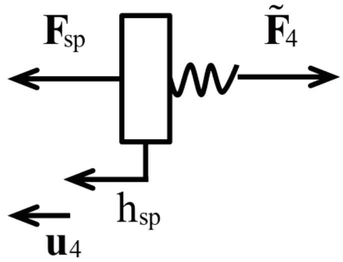

Figure 3.2-3 Free body diagram of the air bearing active element with a spring

where F_{sp}^0 is the force that the spring provides at its initial deformation (corresponding to the case where the active part of the air bearing with a spring belongs to the same sphere as the other active parts); k is the spring stiffness coefficient; k is equal to zero when a constant force spring is chosen.

Combining equations (3.4) – (3.6), the following system of equations is obtained:

$$\begin{cases} F_0 \cdot 0.843^{h_a-5}\left(0.843^{\mathbf{d}\cdot\mathbf{u}_1}\mathbf{u}_1 + 0.843^{\mathbf{d}\cdot\mathbf{u}_2}\mathbf{u}_2 + 0.843^{\mathbf{d}\cdot\mathbf{u}_3}\mathbf{u}_3 + 0.843^{\mathbf{d}\cdot\mathbf{u}_4 - h_{sp}}\mathbf{u}_4\right) + m\mathbf{g} = 0 \\ F_{sp} = F_{sp}^0 + kh_{sp} \end{cases} \tag{3.7}$$

Here, the forces can be decoupled from the displacement $\mathbf{d}$, because only 3 forces are left independent. Then (3.7) is easier to solve with respect to $\mathbf{F}_i$:

$$F_1\mathbf{u}_1 + F_2\mathbf{u}_2 + F_3\mathbf{u}_3 + F_{sp}\mathbf{u}_4 + m\mathbf{g} = 0 \tag{3.8}$$

Being given the spring force, system of equations (3.8) contains 3 unknown forces F_1, F_2, F_3 and 3 linear equations that uniquely define these forces.

3.2.3 Discussion on the simulation results

Equations (3.4) and (3.8) are used to simulate the behavior of the air bearing assembly. Figure 3.2-4 and Figure 3.2-5 show lift forces, fly heights and the Inner Sphere CoM trajectory as functions of the Spheres orientation for the rigidly connected air bearings and the system with a spring, respectively. The magnitude of the CoM trajectory represents the norm of the vector $\mathbf{d}$. The plots represent functions of the angular coordinate of the Inner Sphere in the fixed frame, unless otherwise stated.

The following parameters are used in the simulations:

Radius of the Inner Sphere	105 mm
Mass of the Inner Sphere	3 kg
Air bearing force at 5µm fly height	178 N
Spring force (selected according to the payload mass)	50 N
Spring stiffness coefficient	0 N/µm (constant force spring)
Motion of the Inner Sphere	Rotation around Y, 1°/sec

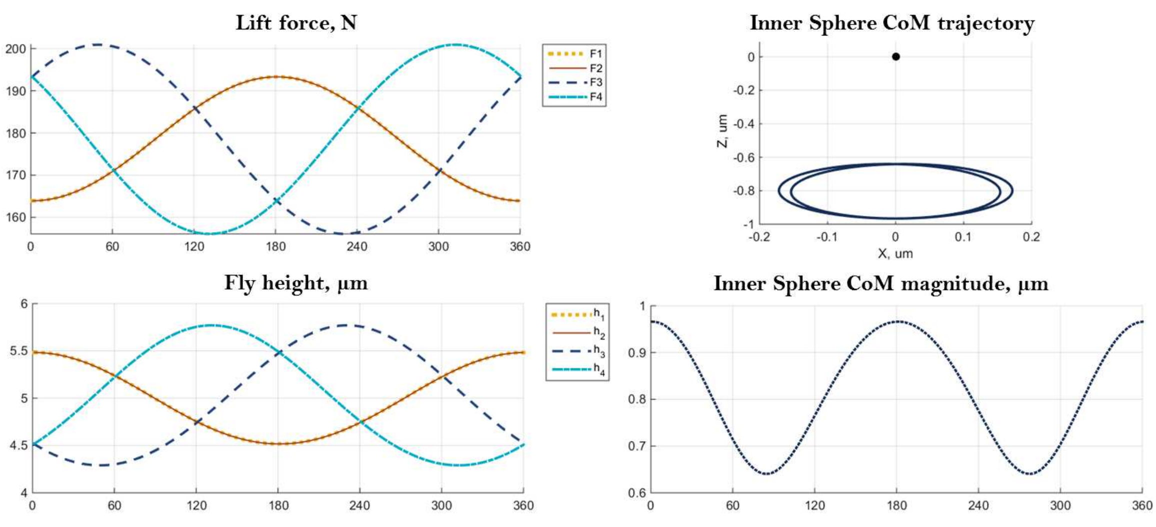

Figure 3.2-4 Lift force, fly height and Inner Sphere CoM trajectory diagrams for the system with rigidly fixed air bearings. Sphere clearance 5 µm

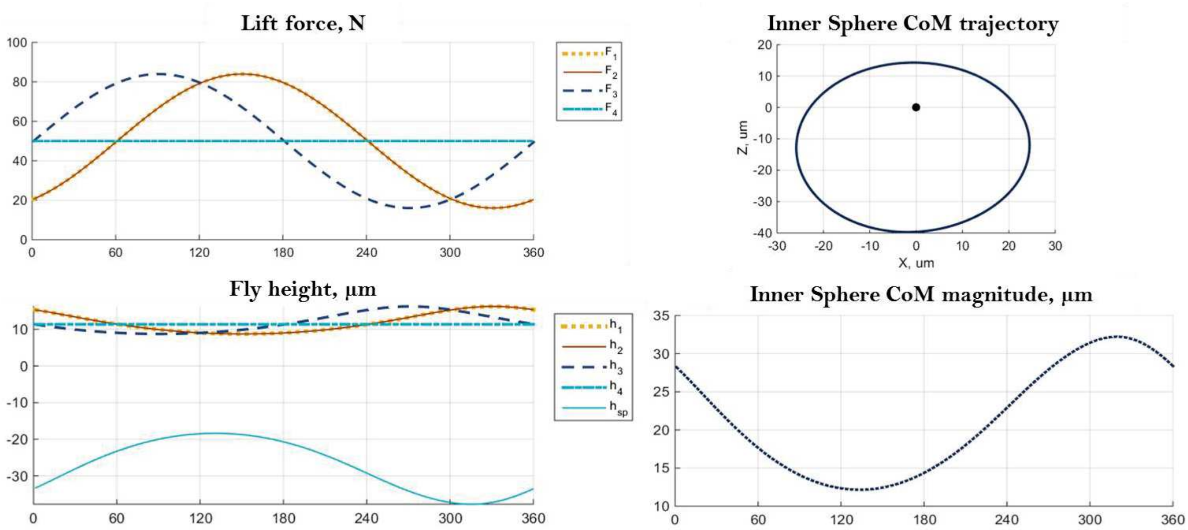

Figure 3.2-5 Lift force, fly height and Inner Sphere CoM trajectory diagrams for the system where one air bearing is adjusted by a spring. Sphere clearance 5 μm

When all air bearings are rigidly connected, their fly heights (and, consequently, lift forces as it follows from (3.2)) are coupled and depend on the sphere clearance. The equation (3.3) shows that the Inner Sphere CoM displacement $\mathbf{d}$ is a function of the fly height and the sphere clearance. Consequently, the position of the Inner Sphere CoM in the Outer Sphere coordinates largely fluctuates, when the spheres rotate, and the magnitude of this fluctuation is increasing as a function of the sphere clearance. This statement is well illustrated in Figure 3.2-6 (left) for CoM trajectories with 3 different sphere clearance sizes.

Analyzing equations (3.7) and (3.8) for the system with a spring, it is easy to see that the system is not over constrained anymore and it has only three variable forces to define three coordinates. Then, the lift forces are functions of the mass, spring force and angular coordinated of the spheres $F_{i=1..3} = f\left(F_{sp}, m, \alpha, \beta, \gamma\right)$, but it is independent of other parameters, which are the fly height and clearance. It means that the spring force distinctively defines lift forces provided by the three fixed air bearings and these forces are constant for any sphere clearance.

The fly height for the system with a spring can be calculated from (3.2) as follows:

$$h_i = \log_{0.843}\left(F_i / F_0\right) + 5, \ i = 1..4 \tag{3.9}$$

Thus, the fly heights is the following function $h_i = f\left(F_0, F_{sp}, m, \alpha, \beta, \gamma\right)$, and it can be uniquely calculated for these parameters.

The displacement $\mathbf{d}$ is linearly coupled with the sphere clearance:

$$\mathbf{d} \cdot \mathbf{u}_i = h_i - h_a \tag{3.10}$$

Considering (3.9), the displacement is the function $\mathbf{d} = f\left(h_a, F_0, F_{sp}, m, \alpha, \beta, \gamma\right)$. Thus, being given the required parameters of the system and the range of the sphere clearance from 5μm to 100μm, the resulting Inner Sphere CoM motion is shown in Figure 3.2-6 (right).

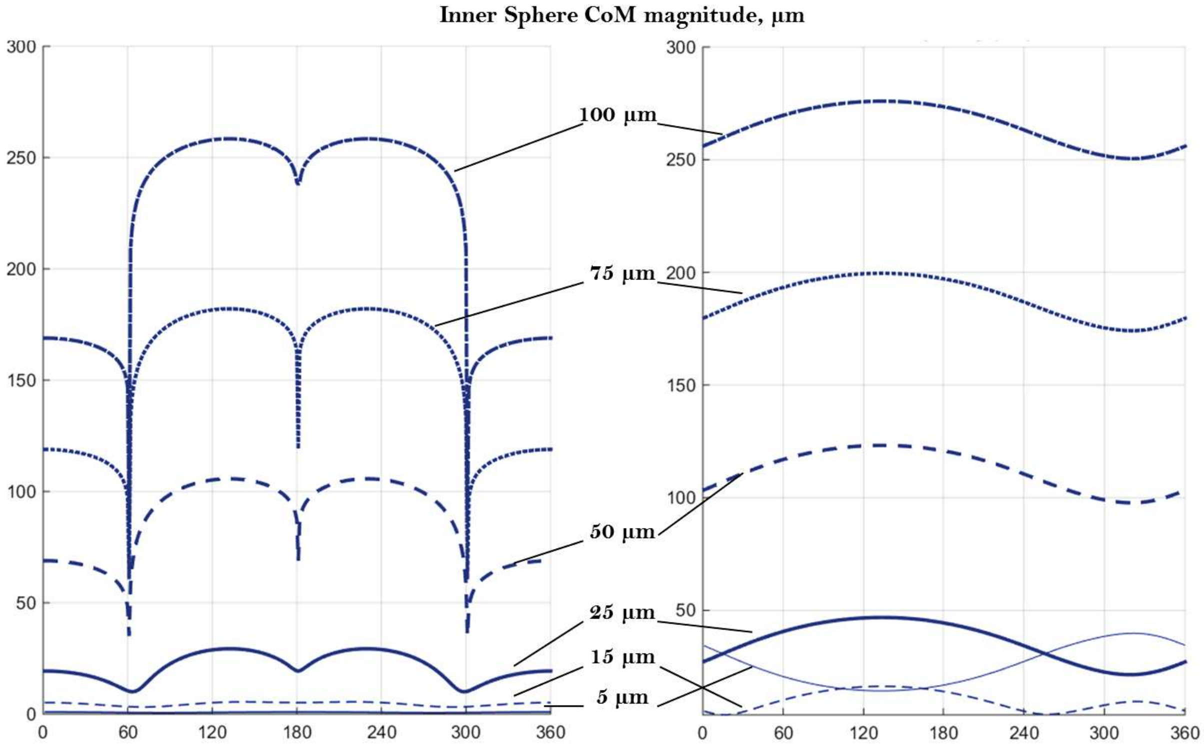

Figure 3.2-6 Magnitude of the Inner Sphere CoM fluctuations: left – all air bearings are rigidly fixed; right - one air bearing is adjusted by a spring. Sphere clearance 5…100 μm

Comparison of the simulation results for the system with 4 rigidly fixed air bearings and the system with an air bearing adjusted by a spring show that in the latter case the Inner Sphere CoM motion is much smoother for larger sphere clearance (>25 μm). This effect of using a spring is especially important for the testbed design: The spring (i) allows reduction of the tolerance requirements for the Spheres assembling; (ii) features smoother Inner Sphere motion for large sphere clearance (it is essential for the case of low tolerance requirements). Indeed, if the micron-scale of the assembling accuracy cannot be reached, the AirBall system takes advantage of using a spring adjustment in one of the air bearing.

3.3 DETERMINATION OF THE CUBESAT ORIENTATION

Determination of the CubeSat and the Inner Sphere orientation is the purpose of the measurement system employed in the AirBall testbed and its prototype. Knowledge of the orientation is very important for two tasks: (i) control of the robotic arm, which adjusts the orientation of the Outer Sphere with respect to the Inner Sphere; (ii) evaluation of the CubeSat trajectory induced by the ADCS operation. For the first task, information about the relative orientation of the Inner and Outer Spheres is enough, while for the second task, absolute orientation of the CubeSat in the fixed reference frame is desired.

In the determination techniques presented below, the orientation of the Outer Sphere is considered to be known. Indeed, it corresponds to the robotic arm end effector pose, which can be computed knowing the joint values. Thus, the relative orientation of the Inner and Outer Spheres is of interest since it is enough for both aforementioned tasks.

According to the discussions in Section 2.2.4, it was decided to build the measurement system using laser sensors. They allow contactless measuring with reliable accuracy and frequency. Two possibilities to adapt sensors for the determination of the CubeSat and the Inner Sphere orientation have been reviewed and evaluated by means of simulations. These approaches and results of the simulations are presented in the following sections.

3.3.1 Approach with redundant measurements

This approach is based on the estimation of the relative positions of the air bearing parts. The sensors are placed by two on the active part of each air bearing as it was shown in Figure 2.2-7, so that they measure distances to the edge of the passive part in two orthogonal planes. Thus, this approach requires 8 sensors in total.

There are several coordinate frames involved to the determination of the Inner Sphere orientation (Figure 3.3-1): The inertial fixed frame $\mathcal{F}_{\text{fix}}$, the frames fixed to the Inner Sphere $\mathcal{F}_{\text{inn}}$ and to the Outer Sphere $\mathcal{F}_{\text{out}}$. There are also frames associated with the air bearing active elements on the Outer Sphere $\mathcal{F}_{\text{out\_i}}$ and $\mathcal{F}_{\text{inn\_i}}$ which are associated with the passive elements, where index i designates one of the four air bearings. All frames are centered at the center of rotation of the testbed O. The axis $\mathbf{x}$ of $\mathcal{F}_{\text{out\_i}}$ is pointed at the center $\text{O}_{\text{out\_i}}$ of the i th air bearing active element, the axis $\mathbf{x}$ of $\mathcal{F}_{\text{inn\_i}}$ is pointed at the center $\text{O}_{\text{inn\_i}}$ of the i th air bearing passive element.

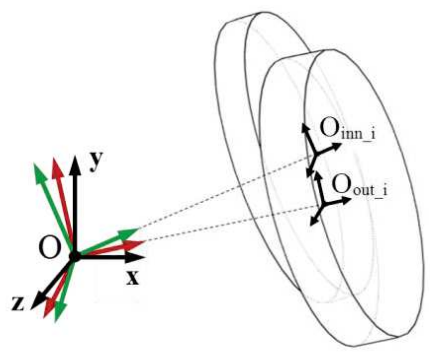

Figure 3.3-1 Frames involved in the tracking process. At point O : the fixed frame $\mathcal{F}_{\text{fix}}$ (black), the Outer Sphere frame $\mathcal{F}_{\text{out}}$ (red), the Inner Sphere frame $\mathcal{F}_{\text{inn}}$ (green). The frames $\mathcal{F}_{\text{inn\_i}}$ and $\mathcal{F}_{\text{out\_i}}$ are centered at points $\text{O}_{\text{inn\_i}}$ and $\text{O}_{\text{out\_i}}$, respectively.

Since the orientations of $\mathcal{F}_{\text{inn\_i}}$ in $\mathcal{F}_{\text{inn}}$ and $\mathcal{F}_{\text{out\_i}}$ in $\mathcal{F}_{\text{out}}$ are known a priori, the positions of the points $\text{O}_{\text{inn\_i}}$ in $\mathcal{F}_{\text{out\_i}}$ are enough to describe the orientation of the Inner Sphere with respect to $\mathcal{F}_{\text{out}}$ of the Outer Sphere. Then, the absolute orientation of the CubeSat and of the Inner Sphere can also be found, because the orientation of $\mathcal{F}_{\text{out}}$ in $\mathcal{F}_{\text{fix}}$ can be identified by means of the encoders and the direct kinematics of the robot arm.

Let the vector pointed to $\text{O}_{\text{inn\_i}}$ with an origin at O be denoted as $\mathbf{q}_i$ and the vector pointed to $\text{O}_{\text{out\_i}}$ be denoted as $\mathbf{x}_i$. Then in the frame $\mathcal{F}_{\text{out}}$, vectors $\mathbf{q}_i$ and $\mathbf{x}_i$ satisfy the following relation:

$$\mathbf{x}_i = f\left(\phi_1, \phi_2, \phi_3, \mathbf{q}_i\right), \tag{3.11}$$

where ϕ_k are angles that uniquely define the orientation of $\mathcal{F}_{\text{inn}}$ in $\mathcal{F}_{\text{out}}$, e.g. Euler angles. In this work, the rotation matrices are rather used. Then (3.11) is written as follows:

$$\mathbf{x}_i = {}^{\mathbf{out}}\mathbf{R}_{\mathbf{inn}}\,{}^{\mathbf{inn}}\mathbf{R}_{\mathbf{inn\_i}}\mathbf{q}_i\,, \tag{3.12}$$

where ${}^{\mathbf{inn}}\mathbf{R}_{\mathbf{inn\_i}}$ defines the orientation of $\mathcal{F}_{\mathrm{inn\_i}}$ in $\mathcal{F}_{\mathrm{inn}}$ and, respectively, ${}^{\mathbf{out}}\mathbf{R}_{\mathbf{inn}}$ denotes the orientation of the Inner Sphere in the Outer Sphere, accordingly, this matrix is to be determined. As it is a rotation matrix, it contains 9 components, but and only three of them are independent. To keep (3.12) linear, independencies between components of ${}^{\mathbf{out}}\mathbf{R}_{\mathbf{inn}}$ are not introduced at this step. For i=1..4, the system of equations (3.12) consists of 12 equations, which is more than the number of unknowns. It thusly can be solved by the Least Squares (LS) method. To this end, (3.12) is written as follows:

$$\mathbf{x}_i = \mathbf{A}\mathbf{b}_i\,, \tag{3.13}$$

where $\mathbf{A} = {}^{\mathbf{out}}\mathbf{R}_{\mathbf{inn}}$ and $\mathbf{b}_i = {}^{\mathbf{inn}}\mathbf{R}_{\mathbf{inn\_i}}\mathbf{q}_i$.

The system of equations (3.13) can be rewritten with the matrix $\mathbf{A}$ replaced by a vector $\mathbf{a}$ having the same components:

$$\mathbf{a} = \begin{bmatrix} A_{11} & A_{12} & A_{13} & A_{21} & A_{22} & A_{23} & A_{31} & A_{32} & A_{33} \end{bmatrix}^T \tag{3.14}$$

and the vector $\mathbf{b}_i$ is written as a 3 by 9 matrix $\mathbf{B}_i$:

$$\mathbf{B}_i = \begin{bmatrix} b_1 & b_2 & b_3 & 0 & 0 & 0 & 0 & 0 & 0 \\ 0 & 0 & 0 & b_1 & b_2 & b_3 & 0 & 0 & 0 \\ 0 & 0 & 0 & 0 & 0 & 0 & b_1 & b_2 & b_3 \end{bmatrix} \tag{3.15}$$

Then, the solution of (3.13) is found as follows:

$$\mathbf{a} = \mathbf{B}^{+}\mathbf{x}\,, \tag{3.16}$$

where $\mathbf{B}^{+}$ is pseudoinverse of the concatenated matrices $\mathbf{B}_i$ for i=1..4, $\mathbf{x}$ is concatenated vectors $\mathbf{x}_i$ for $i = 1...4$. Using this LS solution, the matrix ${}^{\mathbf{out}}\mathbf{R}_{\mathbf{inn}}$ can be composed from the components of the vector $\mathbf{a}$. Thus, being given (3.12), the solution for the desired rotation matrix ${}^{\mathbf{out}}\mathbf{R}_{\mathbf{inn}}$ is calculated using (3.16) but, since the obtained matrix is generally not an orthogonal matrix, the Gram-Schmidt orthogonalization shall be applied.

The vector $\mathbf{q}_i$, included in (3.12), depends on the orientation of the Inner Sphere and it can be found using sensor measurements. To this end, the air bearings and the measurement rays of the sensors are estimated by simple geometrical shapes to find their intersections. The passive part of the air bearing is represented by cylinders with radius r and axis $\mathbf{q}_i$, as it is shown in Figure 3.3-2.

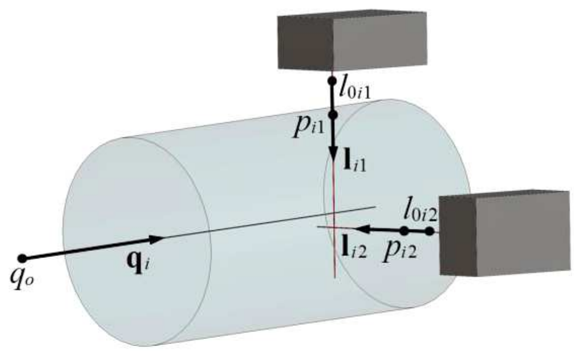

Figure 3.3-2 Geometrical model of the passive part of the air bearing and the measurement rays

Then, the equation defining each cylinder:

$$\left(\left(\mathbf{p}_{ci}-\mathbf{q}_0\right)-\left(\left(\mathbf{p}_{ci}-\mathbf{q}_0\right)\cdot\mathbf{q}_i\right)\cdot\mathbf{q}_i\right)^2=r^2\,, \tag{3.17}$$

where $\mathbf{p}_{ci}$ is a point on the cylinder surface and $\mathbf{q}_0$ is the coordinate vector of a point on the axis $\mathbf{q}_i$. In this case, the point with coordinates $\mathbf{q}_0$ is defined at the point O. The measurement ray is represented by a straight line:

$$\mathbf{l}_{0ij}+a_{ij}\mathbf{l}_{ij}=\mathbf{p}_{ij}\,, \tag{3.18}$$

where $\mathbf{p}_{ij}$ is the coordinate vector of a point on the line, $\mathbf{l}_{0ij}$ is the coordinate vector of a fixed point on the line of the measurement ray, $\mathbf{l}_{ij}$ is a vector collinear with the ray, a_{ij} is the measured distance from point $\mathbf{l}_{0ij}$ to $\mathbf{p}_{ij}$, j is the index of the sensor (two sensors per air bearing). The intersection points of a cylinder and a line are given by the solutions of the following equation:

$$\left(\left(\mathbf{l}_{0ij}+a_{ij}\mathbf{l}_{ij}-\mathbf{q}_0\right)-\left(\left(\mathbf{l}_{0ij}+a_{ij}\mathbf{l}_{ij}-\mathbf{q}_0\right)\cdot\mathbf{q}_i\right)\cdot\mathbf{q}_i\right)^2=r^2 \tag{3.19}$$

The vectors used in (3.17) and (3.18) can be easily described in their respective local frames and then be expressed in $\mathcal{F}_{\text{out}}$. In (3.19), all terms are already defined in $\mathcal{F}_{\text{out}}$.

There are two problems that could be solved using the equation (3.19): determination and simulation problems. In the determination problem, the orientation of the Inner Sphere is the unknown, so that all variables are known except $\mathbf{q}_i$. In this case the system (3.19) contains 2 equations for $j=1,2$ and the 3 unknown components of the vector $\mathbf{q}_i$. Solutions can be obtained if the equation (3.19) is complemented by a third equation, which stems from the unity of vector $\mathbf{q}_i$ ($|\mathbf{q}_i|=1$).

In the simulation problem, there are only two unknowns a_{ij}, which are sensor measurements corresponding to the given Inner Sphere orientation. Two equations of (3.19) are enough to find them. However, there are two possible solutions for every a_{ij}, which correspond to the two possible intersection points of a cylinder and a straight line. The correct solution shall be defined based on the actual geometry of the system.

3.3.2 Approach based on small angles approximation

The motion of the Inner Sphere with respect to the Outer Sphere has 3 rotational DoF, thus the minimum required number of measurements is three. However, the approach presented in the previous section requires at least 6 measurements that are obviously excessive. In order to reduce the number of employed sensors, and thereby reduce cost, another approach is proposed. It consists in using only three sensors and a reference shape, with respect to which measurements are made. As neither the Inner Sphere structure nor the CubeSat has a suitable geometry, the additional regular Y-shape element has been chosen to be the reference (Figure 3.3-3).

For the modeling of this measurement method, the distance from the center of rotation O to the center of the reference shape O_1 is considered to be R, the distance from O_1 to the sensor beam is d. Assuming the rotation angles are small, the relations between $\Delta x_1, \Delta x_2, \Delta x_3$,

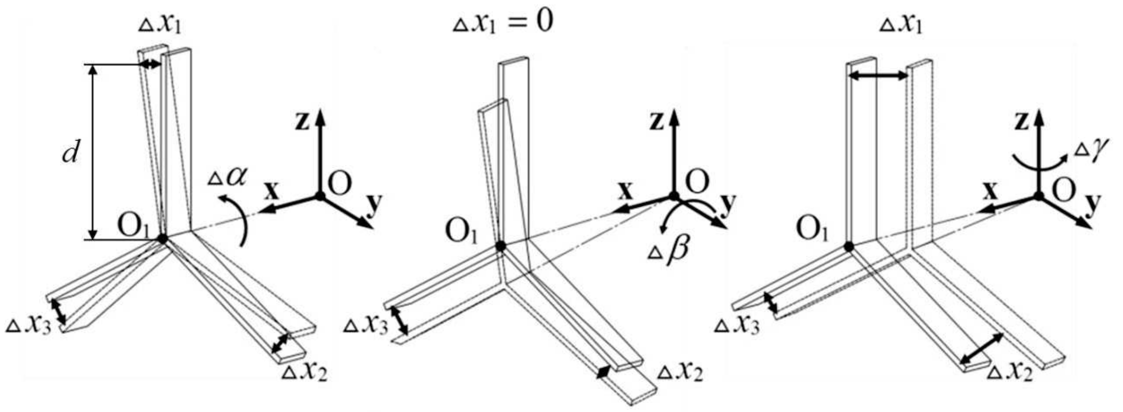

Figure 3.3-3 Orientation of the reference shape before and after a small angle rotation

which are linear displacements of the points on the distance d from the center of the Y-shape, and the small rotations $\triangle\alpha, \triangle\beta, \triangle\gamma$ around each axis of $\mathcal{F}_{out}$ are found.

For $\triangle\alpha$ around X:

$$\triangle x_1 = \triangle x_2 = \triangle x_3 = d\triangle\alpha \tag{3.20}$$

For $\triangle\beta$ around Y:

$$\begin{aligned} \triangle x_1 &= 0, \\ \triangle x_2 &= -\frac{\sqrt{3}}{2}R\triangle\beta, \\ \triangle x_3 &= \frac{\sqrt{3}}{2}R\triangle\beta \end{aligned} \tag{3.21}$$

For $\triangle\gamma$ around Z:

$$\begin{aligned} \triangle x_1 &= -R\triangle\gamma, \\ \triangle x_2 &= \frac{1}{2}R\triangle\gamma, \\ \triangle x_3 &= \frac{1}{2}R\triangle\gamma \end{aligned} \tag{3.22}$$

All relations between small angles and small displacements (3.20) - (3.22) can be combined into one system of linear equations:

$$\begin{bmatrix} \triangle x_1 \\ \triangle x_2 \\ \triangle x_3 \end{bmatrix} = \begin{bmatrix} d & 0 & -R \\ d & -\frac{\sqrt{3}}{2}R & \frac{1}{2}R \\ d & \frac{\sqrt{3}}{2}R & \frac{1}{2}R \end{bmatrix} \begin{bmatrix} \triangle\alpha \\ \triangle\beta \\ \triangle\gamma \end{bmatrix} \tag{3.23}$$

Equation (3.23) gives the Inner Sphere orientation based on the small angle approximation. However, it is more convenient to work with rotation matrices. Standard linearization of small angles will result in a matrix, which is no longer a rotation. To approximate a correct rotation matrix, the Cayley transform can be used [120]:

$$ {}^{\mathbf{out}}\mathbf{R}_{\mathbf{inn}} = \left(\mathbf{I} + \frac{1}{2}[\mathbf{s}]_{\times}\right)\left(\mathbf{I} - \frac{1}{2}[\mathbf{s}]_{\times}\right)^{-1} , \tag{3.24} $$

where $[\mathbf{s}]_{\times}$ is a skew-symmetric matrix of the vector composed of the small angles vector $\mathbf{s} = [\Delta\alpha \quad \Delta\beta \quad \Delta\gamma]^T$. The matrix obtained in (3.24) is orthogonal and has the same order of accuracy as a result of linearization.

The distance sensors are attached to the External Sphere structure and the reference shape moves together with the Inner Sphere. As result, the distance sensor is not pointed always at the same point of the reference shape. It measures distance to the point where measurement ray intersects with the side plane of the reference shape beam. For simulations of the measurements from the distance sensors, this intersection point shall be found for each sensor. The side plane of the reference shape beam is geometrically described as following:

$$ (\mathbf{p}_i - \mathbf{p}_{0i}) \cdot \mathbf{n}_i = 0 , \tag{3.25} $$

where $\mathbf{p}_{0i}$ is a known point on the plane , $\mathbf{n}_i$ is a normal to the plane, $\mathbf{p}_i$ is any point of the plane. The point and normal are easily defined in $\mathcal{F}_{\mathrm{inn\_i}}$ and shall be translated to $\mathcal{F}_{ext}$ with help of ${}^{\mathbf{fix}}\mathbf{R}_{\mathbf{inn}}{}^{\mathbf{inn}}\mathbf{R}_{\mathbf{inn\_i}}$, which are inputs for simulations. In (3.25) $\mathbf{p}_{0i}$, $\mathbf{n}_i$ and $\mathbf{p}_i$ are already expressed in $\mathcal{F}_{ext}$.

The line of the measurement ray is described by (3.18). The distance from $\mathbf{l}_{0i}$ to the intersection point is found as follows:

$$ a_i = \frac{(\mathbf{p}_{0i} - \mathbf{l}_{0i}) \cdot \mathbf{n}_i}{\mathbf{l}_i \cdot \mathbf{n}_i} \tag{3.26} $$

To check efficiency of the small angle approach and to find feasible limits of its applicability, simulation have been done for the range of angles $-10°...10°$.

3.3.3 *Discussion on the simulation results*

In order to compare the relative efficiency of the approaches presented in Sections 3.3.1 and 3.3.2, numerical simulations have been implemented. Sensor measurements have been imitated by solving the simulation problem of (3.19) for method with redundant measurements and by (3.26) for the method based on small angles approximation. The first method can be realized within a strictly limited range for each angle. This range is defined by the geometry of the system, namely by the radius and height of the passive parts of the air bearings. In the simulations, the study has been done for a cylinder with the radius 40mm and infinite length that resulted in the efficient angle range [-6°; 6°]. Beyond this range the measurement beam does not intersect the cylinder. However, for practical applications, limitations caused by the length of the cylinder, i.e., height of the passive part of the air bearing shall be considered.

In Figure 3.3-4, the absolute errors of the results obtained by the approach with the small angles approximation are shown. In case of the method with redundant number of measurements, the absolute errors do not exceed 0.01° for all angles within the valid range (plots are not presented due to even distribution of the errors). Summarizing obtained simulation results, this method provides the finest accuracy. However, for the given geometry, the method with small angles approximation is valid in a wider range of angles [-10°; 10°], being constrained by the applicability of the small angles approximation. Another important issue for the evaluation of the methods is the cost of the system: The method of redundant measurements requires at least 6 sensors, while the other method works with only 3 sensors.

Thus, comparison shows that the first does not requires any elements attached to the Inner Sphere, while the second method has the advantage of lower cost and wider operation range. Considering these factors, the method based on small angles approximation has been selected to be implemented on the AirBall testbed prototype.

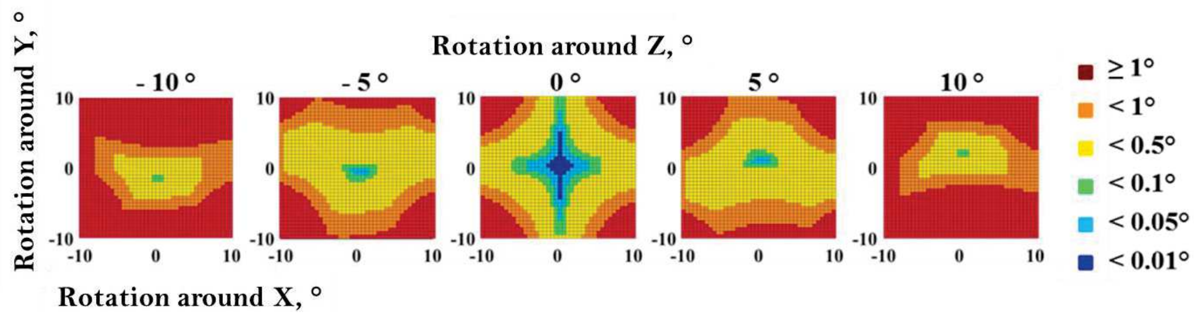

Figure 3.3-4 The simulation results of the CubeSat orientation determination for the approach with the small angles approximation. 3DoF rotation of the Inner Sphere with respect to the Outer Sphere in range [-10°; 10°] is considered.

3.4 Mass balancing technique

A fundamental problem of using the air bearing platforms for ADCS testing is to avoid disturbance torques due to mass unbalance. These torques appear when there is an offset between the payload (a CubeSat with all attached elements) CoM and the testbed CoR. A mass balancing is provided to eliminate this offset and to diminish the disturbing gravity torque. To this end, the position of the payload CoM together with its inertial parameters has to be identified. In the sequel, the inertial parameters and the CoM position are referred to as the dynamic parameters.

The identification of dynamic parameters is a well-known technique in robotics and related fields. Several approaches have been proposed in the literature to solve the dynamic parameter identification problem concerning robots [108], [121]–[126] and specifically for spacecrafts [95], [127]–[130]. Some common features of these approaches can be found, namely [122]:

- Use of inverse dynamic or energy model to form the identification equations;
- Use of an optimal exciting trajectory for efficient model sampling;
- Use of an over-determinate linear system of equations resulting from the model sampling;
- Solving the linear system by the LS method to estimate the parameters.

In all the aforementioned approaches, the identification of the dynamic parameters is done for systems subjected to external actuation (usually, joint forces/torques). For example in [128] and [130], where the identification and balancing of spacecraft simulators are done, the testbeds use reaction wheels for actuation. In [95], actuation is created by means of automatically sliding small masses. The identification equations can be written in the following general form:

$$\mathbf{y}(\mathbf{\Gamma}) = \mathbf{W}\,\mathbf{x}\,, \tag{3.27}$$

where $\mathbf{\Gamma}$ is an external torque, $\mathbf{W}$ is an observation matrix, and $\mathbf{x}$ is the vector of the dynamic parameters to be identified. However, the mass balancing system for the AirBall testbed was designed to be a passive one. In this case there is no possibility to provide actuation and the right-hand side of (3.27) is always equal to zero. The testbed is not subjected to any external influences apart from the torque due to gravity. A method of the dynamic parameter identification suitable to the passive case and based on the sampling of free oscillating rotations is presented below.

3.4.1 Kinematics and dynamics

The payload of the test bench is considered to comprise the CubeSat together with the Inner Sphere and the adjusting mechanism, which are rigidly connected and move as one body. In the sequel, "body" refers to the payload. The frames involved in the identification are described below.

The inertial fixed frame $\mathcal{F}_{\text{fix}}$ is defined by the basis $\mathcal{B}_{\text{fix}}$, denoted $(\mathbf{x}_{\text{fix}}, \mathbf{y}_{\text{fix}}, \mathbf{z}_{\text{fix}})$, and its origin centered at the CoR (point CR). Vector $\mathbf{z}_{\text{fix}}$ is aligned with the local vertical (Figure 3.4-1). Let the basis $\mathcal{B}_{bf}$, denoted $(\mathbf{x}, \mathbf{y}, \mathbf{z})$, be attached to the body, and let the body-fixed reference frame $\mathcal{F}_{bf}$ consist of $\mathcal{B}_{bf}$ centered at a given point O of the body. The choice of O will be discussed in the following section.

The frame $\mathcal{F}_{BF}$ shown has the same orientation as $\mathcal{B}_{bf}$ but its origin is CR. As shown in the sequel, the frame $\mathcal{F}_{BF}$ is introduced to simplify the writing of the equations of motion, suitable for identification. The position of the point CM (coincident with the CoM of the body) in $\mathcal{F}_{BF}$ is defined by the column vector $\boldsymbol{\rho}$. As shown in Figure 3.4-1, it can be written as the sum of the vectors $\boldsymbol{\rho}^{\mathbf{O}}$ and $\mathbf{r}$ expressed in $\mathcal{B}_{bf}$

$$\boldsymbol{\rho} = \mathbf{r} + \boldsymbol{\rho}^{\mathbf{O}} \tag{3.28}$$

It should be noted that the vector $\mathbf{r}$ is related to the position of the body in $\mathcal{F}_{BF}$ and the vector $\boldsymbol{\rho}^{\mathbf{O}}$ is constant for the given body.

The orientation of $\mathcal{F}_{BF}$ with respect to $\mathcal{F}_{\text{fix}}$ is given by the rotation matrix ${}^{\mathbf{fix}}\mathbf{R}_{\mathbf{BF}}$. In $\mathcal{B}_{\text{fix}}$, the angular velocity vector of the body ${}^{\mathbf{fix}}\boldsymbol{\omega}$ can be found as follows

$$\left[{}^{\mathbf{fix}}\boldsymbol{\omega}\right]_{\times} = {}^{\mathbf{fix}}\dot{\mathbf{R}}_{\mathbf{BF}}\,{}^{\mathbf{fix}}\mathbf{R}_{\mathbf{BF}}^{T}\,, \tag{3.29}$$

where $\left[{}^{\mathbf{fix}}\boldsymbol{\omega}\right]_{\times}$ is the skew-symmetric matrix associated to the vector ${}^{\mathbf{fix}}\boldsymbol{\omega}$. The following operation can be used to express the angular velocity vector $\boldsymbol{\omega}$ in $\mathcal{B}_{bf}$

$$\boldsymbol{\omega} = {}^{\mathbf{BF}}\mathbf{R}_{\mathbf{fix}}\,{}^{\mathbf{fix}}\boldsymbol{\omega} \tag{3.30}$$

In the sequel, all vectors without a left superscript are expressed in $\mathcal{B}_{bf}$.

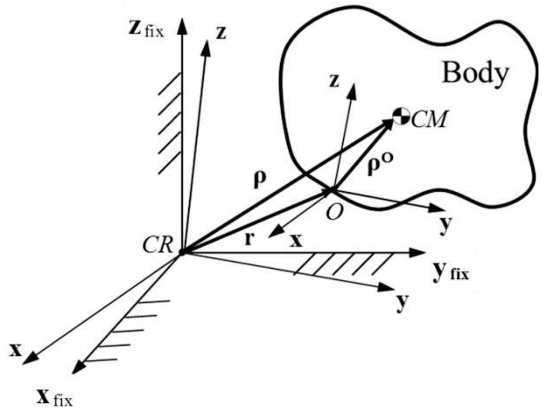

Figure 3.4-1 Frames involved in the identification process

The Euler's equation of motion traditionally describes the rotational dynamics of a body with respect to a coordinate frame whose origin is the body's CoM. The testbed payload is subjected to the action of a gravity torque (when the points CR and CM are not perfectly coincident) and to the reaction forces at the air bearings. The reaction forces are pointing towards the CoR. They can be represented by a resulting force passing through CR. The magnitude and direction of this force are unknown. However, the equations of motion does not include this unknown resulting force if the Euler's equations of motion are expressed in $\mathcal{F}_{BF}$

$$\mathbf{I}^{\mathbf{CR}}\,\dot{\boldsymbol{\omega}}+\boldsymbol{\omega}\times\mathbf{I}^{\mathbf{CR}}\,\boldsymbol{\omega}=\mathbf{T}^{\mathbf{CR}}, \tag{3.31}$$

where $\mathbf{I}^{\mathbf{CR}}$ is the inertia matrix of the body at CR, $\mathbf{T}^{\mathbf{CR}}$ is the torque induced at CR by the weight $m\mathbf{g}$ of the body

$$\mathbf{T}^{\mathbf{CR}}=\boldsymbol{\rho}\times m\,\mathbf{g}=-m\left[\mathbf{g}\right]_{\times}\boldsymbol{\rho}=-m\left[{}^{\mathbf{BF}}\mathbf{R}_{\mathbf{fix}}\,{}^{\mathbf{fix}}\mathbf{g}\right]_{\times}\boldsymbol{\rho} \tag{3.32}$$

Substituting (3.32) into (3.31) results in

$$\mathbf{I}^{\mathbf{CR}}\,\dot{\boldsymbol{\omega}}+\boldsymbol{\omega}\times\mathbf{I}^{\mathbf{CR}}\,\boldsymbol{\omega}+m\left[{}^{\mathbf{BF}}\mathbf{R}_{\mathbf{fix}}\,{}^{\mathbf{fix}}\mathbf{g}\right]_{\times}\boldsymbol{\rho}=\mathbf{0} \tag{3.33}$$

Equation (3.33) describes the dynamics of the testbed payload in $\mathcal{B}_{bf}$. This equation can be used to obtain the identification equations in the form $\boldsymbol{\Phi}\mathbf{x}=\mathbf{b}$, where vector $\mathbf{x}$ contains the body dynamic parameters to be identified.

3.4.2 Dynamic parameters identification

The goal of the identification process is to find the dynamic parameters of the body. The dynamic model (3.33) in the current formulation is a function of the parameters taken with respect to the CoR ($\mathbf{I}^{\mathbf{CR}}$ and $\boldsymbol{\rho}$) so that the vector $\mathbf{b}$ is always equal to zero. Moreover, $\mathbf{I}^{\mathbf{CR}}$ and $\boldsymbol{\rho}$ are related to the position of the body in $\mathcal{F}_{BF}$, hence the result of the identification depends on the initial position of the body with respect to the CoR. Such an objectionable situation can be avoided, if the dynamic parameters are defined at a point attached to the body. The points CM and O are two candidate points (Figure 3.4-1). Choosing CM yields nonlinearities in the dynamic parameters. On the contrary, choosing O leads to a linear system. $\mathbf{I}^{\mathbf{CR}}$ and $\boldsymbol{\rho}$ shall thus be expressed with respect to O and substituted into (3.33).

The inertia matrix $\mathbf{I}^{\mathbf{CM}}$ taken at CM and expressed in $\mathcal{B}_{bf}$ is:

$$\mathbf{I}^{\mathbf{CM}} = \begin{bmatrix} I_{xx}^{CM} & I_{xy}^{CM} & I_{xz}^{CM} \\ I_{xy}^{CM} & I_{yy}^{CM} & I_{yz}^{CM} \\ I_{xz}^{CM} & I_{yz}^{CM} & I_{zz}^{CM} \end{bmatrix} \tag{3.34}$$

Then, $\mathbf{I}^{\mathbf{CR}}$ can be found by applying the Huygens-Steiner theorem:

$$\mathbf{I}^{\mathbf{CR}} = \mathbf{I}^{\mathbf{CM}} + m\left(\boldsymbol{\rho}^T \boldsymbol{\rho}\, \mathbf{1} - \boldsymbol{\rho}\, \boldsymbol{\rho}^T\right), \tag{3.35}$$

where $\mathbf{1}$ is the 3×3 identity matrix. Substituting (3.28) into (3.35) gives

$$\mathbf{I}^{\mathbf{CR}} = \mathbf{I}^{\mathbf{CM}} + m\left(\left(\boldsymbol{\rho}^{\mathbf{O}} + \mathbf{r}\right)^T \left(\boldsymbol{\rho}^{\mathbf{O}} + \mathbf{r}\right) \mathbf{1} - \left(\boldsymbol{\rho}^{\mathbf{O}} + \mathbf{r}\right)\left(\boldsymbol{\rho}^{\mathbf{O}} + \mathbf{r}\right)^T\right) = \mathbf{I}^{\mathbf{O}} + \mathbf{C}(\mathbf{r}) + m\left(2\boldsymbol{\rho}^{\mathbf{O}T}\mathbf{r}\,\mathbf{1} - \left(\boldsymbol{\rho}^{\mathbf{O}}\mathbf{r}^T + \mathbf{r}\,\boldsymbol{\rho}^{\mathbf{O}T}\right)\right), \tag{3.36}$$

where the inertia matrix of the body taken at O and expressed in $\mathcal{B}_{bf}$ is

$$\mathbf{I}^{\mathbf{O}} = \mathbf{I}^{\mathbf{CM}} + m\left(\boldsymbol{\rho}^{\mathbf{O}T}\boldsymbol{\rho}^{\mathbf{O}}\,\mathbf{1} - \boldsymbol{\rho}^{\mathbf{O}}\boldsymbol{\rho}^{\mathbf{O}T}\right), \tag{3.37}$$

and $\mathbf{C}(\mathbf{r})$ is a value depending only on the position of the body in $\mathcal{F}_{BF}$ and on the body's mass m:

$$\mathbf{C}(\mathbf{r}) = m\left(\mathbf{r}^T\mathbf{r}\,\mathbf{1} - \mathbf{r}\,\mathbf{r}^T\right) \tag{3.38}$$

The decomposition of the inertia matrix presented in (3.36) is convenient for further simplification and transformation of (3.33).

Taking into account the relations obtained in the previous section, (3.33) can be rewritten as a linear equation in the dynamic parameters. The product of the inertia matrix and the angular velocity becomes

$$\mathbf{I}^{\mathbf{CR}}\boldsymbol{\omega} = \mathbf{I}^{\mathbf{O}}\boldsymbol{\omega} + \mathbf{C}(\mathbf{r})\boldsymbol{\omega} + m\mathbf{B}(\boldsymbol{\omega},\mathbf{r})\boldsymbol{\rho}^{\mathbf{O}}, \tag{3.39}$$

where matrix $\mathbf{B}(\boldsymbol{\omega},\mathbf{r})$ is defined as

$$\mathbf{B}(\boldsymbol{\omega},\mathbf{r}) = \begin{bmatrix} -r_2\omega_2 - r_3\omega_3 & 2r_2\omega_1 - r_1\omega_2 & 2r_3\omega_1 - r_1\omega_3 \\ 2r_1\omega_2 - r_2\omega_1 & -r_1\omega_1 - r_3\omega_3 & 2r_3\omega_2 - r_2\omega_3 \\ 2r_1\omega_3 - r_3\omega_1 & 2r_2\omega_3 - r_3\omega_2 & -r_1\omega_1 - r_2\omega_2 \end{bmatrix} \tag{3.40}$$

Equation (3.39) can be modified to highlight the fact that it is linear in the unknown values $\mathbf{I}^{\mathbf{O}}$ and $\boldsymbol{\rho}^{\mathbf{O}}$. The first term on the right-hand side can be written

$$\mathbf{I}^{\mathbf{O}}\boldsymbol{\omega} = \boldsymbol{\Omega}(\boldsymbol{\omega})\mathbf{j}^{\mathbf{O}}, \tag{3.41}$$

where $\mathbf{j}^{\mathbf{O}}$ is a 6×1 vector composed of the elements of the inertia matrix $\mathbf{I}^{\mathbf{O}}$ and $\boldsymbol{\Omega}(\boldsymbol{\omega})$ is 3×6 matrix composed of the elements of the vector $\boldsymbol{\omega}$ as following:

$$\mathbf{j}^{\mathbf{O}} = \begin{bmatrix} I_{xx}^{O} & I_{yy}^{O} & I_{zz}^{O} & I_{xy}^{O} & I_{xz}^{O} & I_{yz}^{O} \end{bmatrix}^T \tag{3.42}$$

$$\boldsymbol{\Omega}(\boldsymbol{\omega}) = \begin{bmatrix} \omega_1 & 0 & 0 & \omega_2 & \omega_3 & 0 \\ 0 & \omega_2 & 0 & \omega_1 & 0 & \omega_3 \\ 0 & 0 & \omega_3 & \omega_1 & \omega_2 & 0 \end{bmatrix} \tag{3.43}$$

Accordingly, the expression of $\mathbf{I}^{\mathbf{CR}}\,\dot{\boldsymbol{\omega}}$ can be written

$$\mathbf{I}^{\mathbf{CR}}\,\dot{\boldsymbol{\omega}} = \boldsymbol{\Omega}(\dot{\boldsymbol{\omega}})\,\mathbf{j}^{\mathbf{O}} + m\,\mathbf{B}(\dot{\boldsymbol{\omega}},\mathbf{r})\boldsymbol{\rho}^{\mathbf{O}} + \mathbf{C}(\mathbf{r})\dot{\boldsymbol{\omega}} \tag{3.44}$$

Collecting all dynamic parameters on the left-hand side, the equation (3.33) is finally written in matrix form

$$\left[\boldsymbol{\Omega}(\dot{\boldsymbol{\omega}})+[\boldsymbol{\omega}]_\times\boldsymbol{\Omega}(\boldsymbol{\omega}) \;\vdots\; m\left(\mathbf{B}(\dot{\boldsymbol{\omega}},\mathbf{r})+[\boldsymbol{\omega}]_\times\mathbf{B}(\boldsymbol{\omega},\mathbf{r})+[\mathbf{g}]_\times\right)\right]\begin{bmatrix}\mathbf{j}^{\mathbf{O}}\\ \cdots\\ \boldsymbol{\rho}^{\mathbf{O}}\end{bmatrix} = -m[\mathbf{g}]_\times\mathbf{r} - [\boldsymbol{\omega}]_\times\mathbf{C}(\mathbf{r})\boldsymbol{\omega} - \mathbf{C}(\mathbf{r})\dot{\boldsymbol{\omega}} \tag{3.45}$$

Thus, the proposed identification of the components of the inertia matrix and of the position of the CoM is based on the knowledge of the angular position of the body-fixed frame with respect to $\mathcal{F}_{\text{fix}}$. A LS solution requires data obtained from p experiments each having a duration of N_i sec or n_i time steps. During the experiments, the body is moving freely under the influence of the gravity torque created by the body weight when the CoM is not coincident with the CoR. In each experiment, the initial conditions, i.e. the offset between the points CR and O, described by the vector $\mathbf{r}_i$, the initial orientation of the body in $\mathcal{F}_{\text{fix}}$ and its initial angular velocity could be different.

For the j^{th} measurement of the i^{th} experiment, (3.45) is

$$\left[\boldsymbol{\Omega}(\dot{\boldsymbol{\omega}})_{ij}+[\boldsymbol{\omega}_{ij}]_\times\boldsymbol{\Omega}(\boldsymbol{\omega})_{ij} \;\vdots\; m\left(\mathbf{B}(\dot{\boldsymbol{\omega}}_{ij},\mathbf{r}_i)+[\boldsymbol{\omega}_{ij}]_\times\mathbf{B}(\boldsymbol{\omega}_{ij},\mathbf{r}_i)+[\mathbf{g}_{ij}]_\times\right)\right]\begin{bmatrix}\mathbf{j}^{\mathbf{O}}\\ \cdots\\ \boldsymbol{\rho}^{\mathbf{O}}\end{bmatrix} = -m[\mathbf{g}_{ij}]_\times\mathbf{r}_i - [\boldsymbol{\omega}_{ij}]_\times\mathbf{C}(\mathbf{r}_i)\boldsymbol{\omega}_{ij} - \mathbf{C}(\mathbf{r}_i)\dot{\boldsymbol{\omega}}_{ij}\,, \tag{3.46}$$

where $i = 1 \ldots p$, $j = 1 \ldots n_i$.

Finally, gathering all the measurements of all the experiments in a single equation gives

$$\boldsymbol{\Phi}\,\mathbf{x} = \mathbf{b}\,, \tag{3.47}$$

where $\boldsymbol{\Phi}$ is a $3np \times 9$ observation matrix, $\mathbf{x}$ is the 9×1 vector of dynamic parameters and $\mathbf{b}$ is a $3np \times 1$ observation vector. Since there are more equations than unknowns, this problem can be solved computing the LS solution

$$\mathbf{x} = \boldsymbol{\Phi}^{+}\,\mathbf{b}\,, \tag{3.48}$$

where $\boldsymbol{\Phi}^{+}$ is the pseudo-inverse of the observation matrix. This LS solution is an estimation of the dynamic parameters $\mathbf{x}$. The Huygens-Steiner theorem can finally be applied to find the inertia matrix of the body at its CM :

$$\mathbf{I}^{\mathbf{CG}} = \mathbf{I}^{\mathbf{O}} - m\left(\boldsymbol{\rho}^{\mathbf{O}T}\boldsymbol{\rho}^{\mathbf{O}}\,\mathbf{1} - \boldsymbol{\rho}^{\mathbf{O}}\boldsymbol{\rho}^{\mathbf{O}T}\right) \tag{3.49}$$

3.4.3 Iterative mass balancing

The equations in the previous subsections are given for a single rigid body. Practically, in the testbed, the "body" consists of the CubeSat, the Inner Sphere and the adjusting mechanism (Figure 2.2-4). However, in the mass balancing, the CubeSat is expected to move with respect to the Inner Sphere frame. Consequently, the dynamic parameters of the whole payload are variables and cannot be correctly identified. Thus, the identification shall be done separately for the CubeSat's dynamic parameters, which are constant since the CubeSat shape does not change during the experiments. The parameters of the other elements are assumed to be well known. While they are not a subject of interest here, they influence the motion and shall thus be taken into account. Accordingly, (3.28) becomes

$$\boldsymbol{\rho} = \mathbf{r} + \frac{m}{m + \sum_{k=1}^{l} m_k} \boldsymbol{\rho}^{\mathbf{O}} + \frac{1}{m + \sum_{k=1}^{l} m_k} \sum_{k=1}^{l} m_k \boldsymbol{\rho}_k^{\mathbf{O}}, \tag{3.50}$$

where m and $\boldsymbol{\rho}^{\mathbf{O}}$ refer now to the CubeSat while m_k and $\boldsymbol{\rho}_k^{\mathbf{O}}$ refer to the elements attached to the CubeSat, $k = 1 \ldots l$. Moreover, (3.38) becomes

$$\mathbf{C}(\mathbf{r}) = m\left(\mathbf{r}^T \mathbf{r} \mathbf{1} - \mathbf{r} \mathbf{r}^T\right) + \sum_{k=1}^{l} \mathbf{I}_k^{\mathbf{CR}} \tag{3.51}$$

The resulting identification equations can be obtained by substituting (3.50) and (3.51) into (3.46). Before a direct application of this equation to the identification of dynamic parameters, it should be mentioned that the vector $\mathbf{x}$ is not homogeneous. The components of $\mathbf{x}$ have different units (unit of $\boldsymbol{\rho}^{\mathbf{O}}$ is m and unit of $\mathbf{j}^{\mathbf{O}}$ is kg·m²). For CubeSats, the values of $\boldsymbol{\rho}^{\mathbf{O}}$ can be up to 2 orders of magnitude larger than the diagonal components of the inertia matrix, depending on the position of the CoM and on the choice of the point O on the body. An accurate identification can be reached when all the components of the vector $\mathbf{x}$ are of the same order of magnitude. To this end, an iterative approach aiming to minimize the magnitude of $\boldsymbol{\rho}^{\mathbf{O}}$ can be considered. The following sequence of operations is suggested:

- Initialization: Choose the origin O of $\mathcal{F}_{bf}$ at the geometric center of the CubeSat (as a first approximation of the CoM position) and select the initial position of the CubeSat in $\mathcal{F}_{\text{fix}}$ (i.e. vector $\mathbf{r}$) for each of the p experiments;
- Run p experiments in order to form an over-determinate linear system of equations (3.47);
- Derive $\mathbf{x}$ using the LS method;
- Update the position of O in $\mathcal{F}_{\text{fix}}$ according to the identified value $\boldsymbol{\rho}^{\mathbf{O}}$;
- Update $\mathbf{r}$ based on given scaling coefficients;
- Repeat the operations until the required accuracy is reached

This iterative approach results in decreasing the magnitude of $\boldsymbol{\rho}^{\mathbf{O}}$ at every step. It can be seen in (3.37) that the contribution of $\mathbf{I}_0^{\mathbf{CG}}$ in $\mathbf{I}^{\mathbf{O}}$ is larger than the term depending on $\boldsymbol{\rho}^{\mathbf{O}}$, because $\boldsymbol{\rho}^{\mathbf{O}}$ is small and squared. While $\boldsymbol{\rho}^{\mathbf{O}}$ decreases fast, $\mathbf{j}^{\mathbf{O}}$ changes slowly. Accordingly, after a few iterations, the values of $\boldsymbol{\rho}^{\mathbf{O}}$ and $\mathbf{j}^{\mathbf{O}}$ will be of the same order of magnitude and the identification error should be minimized. Besides, when $\boldsymbol{\rho}^{\mathbf{O}}$ is decreasing, the oscillation period increases and the experiment duration N_i might not be large enough to capture the character of the motion. Consequently, a scaling of N_i after each iteration is recommended to avoid this issue.

3.4.4 Discussion on the simulation results

The identification algorithm proposed above shall be tested and, if required, improved before its application to the test bench. Thus, simulations of the identification process in

MATLAB are used to verify the algorithm efficiency. The MATLAB model consists of two parts: The simulation of the body dynamics and the identification of the dynamic parameters that is illustrated in Figure 3.4-2.

The rotating body dynamics is described by the equation of motion (3.33). The simulation of the body motion requires to solve this equation to determine the angular position of the body, described by the rotation matrix ${}^{\mathbf{fix}}\mathbf{R}_{\mathbf{BF}}$. Finding ${}^{\mathbf{fix}}\mathbf{R}_{\mathbf{BF}}$ emulates data about the payload orientation during experiments.

The part of the MATLAB model, dedicated to the identification of the inertial parameters, is similar to the one that will be used during the real experiments. The accuracy of the identification process can be estimated by comparing the "real" values $\mathbf{I}^{\mathbf{CR}}$ and $\boldsymbol{\rho}^{\mathbf{O}}$, chosen by the user for the current model run, and the values $\hat{\mathbf{I}}^{\mathbf{CR}}$ and $\boldsymbol{\rho}^{\mathbf{O}}$ obtained by the identification process.

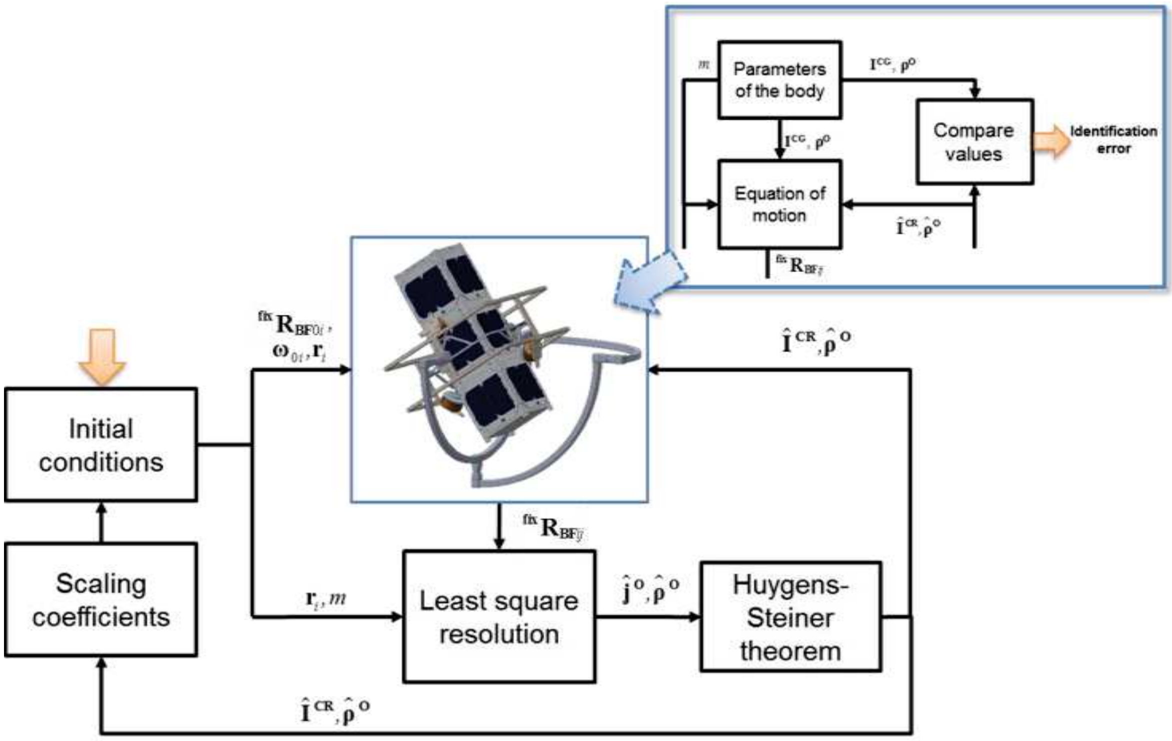

Figure 3.4-2 Simulation scheme of the identification of dynamic parameters

Equation of motion (3.33) shall be written in the following form to be solved by the MATLAB Ordinary Differential Equation (ODE) solver

$$\dot{\mathbf{y}} = f(\mathbf{y}), \tag{3.52}$$

Equation (3.33) contains first and second order derivatives of the angular position of the body. Moreover, the angular velocity is not linearly dependent on the sought-for rotation matrix ${}^{\mathbf{fix}}\mathbf{R}_{\mathbf{BF}}$. The following solution is proposed to deal with this issue.

Let $\mathbf{y}$ to be the vector composed of the components of ${}^{\mathbf{fix}}\mathbf{R}_{\mathbf{BF}}$ and ${}^{\mathbf{fix}}\boldsymbol{\omega}$

$$\mathbf{y} = \left[A_{11} \quad A_{21} \quad A_{31} \quad A_{12} \quad A_{22} \quad A_{32} \quad A_{31} \quad A_{32} \quad A_{33} \;\vdots\; \omega_1 \quad \omega_2 \quad \omega_3\right]^T \tag{3.53}$$

Using (3.29), the first 9 components of $\dot{\mathbf{y}}$ can be found from the equation

$$ {}^{\text{fix}}\dot{\mathbf{R}}_{\mathbf{BF}} = \left[{}^{\text{fix}}\boldsymbol{\omega}\right]_{\times} {}^{\text{fix}}\mathbf{R}_{\mathbf{BF}} \tag{3.54} $$

Equation (3.33) can be solved for ${}^{\text{fix}}\dot{\boldsymbol{\omega}}$, which are the last 3 components of $\dot{\mathbf{y}}$

$$ {}^{\text{fix}}\dot{\boldsymbol{\omega}} = {}^{\text{fix}}\mathbf{R}_{\mathbf{BF}}\left(\left(\mathbf{I}^{\mathbf{CR}}\right)^{-1}\left(-{}^{\mathbf{BF}}\mathbf{R}_{\mathbf{fix}}\, {}^{\text{fix}}\boldsymbol{\omega}\times\mathbf{I}^{\mathbf{CR}}\, {}^{\mathbf{BF}}\mathbf{R}_{\mathbf{fix}}\, {}^{\text{fix}}\boldsymbol{\omega} - m\left[{}^{\mathbf{BF}}\mathbf{R}_{\mathbf{fix}}\, {}^{\text{fix}}\mathbf{g}\right]_{\times}\boldsymbol{\rho}\right)\right) \tag{3.55} $$

Thereby, the equations of motion can be expressed in the form (3.52) which is required by the ODE solver.

Table 8 Initial conditions

Experiment number, p	**1**	**2**	**3**	**4**
Initial offset, r (m)	$\begin{bmatrix}0.02\\0.02\\0.02\end{bmatrix}$	$\begin{bmatrix}-0.02\\-0.02\\0.02\end{bmatrix}$	$\begin{bmatrix}0.02\\0.02\\-0.02\end{bmatrix}$	$\begin{bmatrix}-0.02\\-0.02\\-0.02\end{bmatrix}$

Table 9 Scaling coefficients

$\boldsymbol{\rho}^{\mathrm{O}}$ found at the previous iteration, m	**Scaling coefficient for r**	**Duration of each experiment N_i, sec**
≥ 0.01	1	5
≥ 0.001	0.5	10
≥ 0.0001	0.1	20
< 0.0001	0.05	25

Table 10 Comparison of the predefined and identified values

	1U CubeSat		**3U CubeSat**	
	CAD values	**Identified values (relative error)**	**CAD values**	**Identified values (relative error)**
ρ_1^{O} $(\mathrm{m}\cdot 10^{-3})$	-0.2560	-0.2558 (0.0008)	-1.6393	-1.6398 (0.0003)
ρ_2^{O} $(\mathrm{m}\cdot 10^{-3})$	-0.9320	-0.9317 (0.0003)	-1.2807	-1.2814 (0.0005)
ρ_3^{O} $(\mathrm{m}\cdot 10^{-3})$	-9.9570	-9.9572 (0.0000)	17.1741	17.1749 (0.0000)
$\mathrm{I}_{xx}^{\mathrm{CM}}$ $(\mathrm{kgm}^2\cdot 10^{-3})$	1.5460	1.5325 (0.0087)	30.6915	30.4716 (0.0072)
$\mathrm{I}_{yy}^{\mathrm{CM}}$ $(\mathrm{kgm}^2\cdot 10^{-3})$	1.5910	1.5797 (0.0071)	29.6998	29.4381 (0.0088)
$\mathrm{I}_{zz}^{\mathrm{CM}}$ $(\mathrm{kgm}^2\cdot 10^{-3})$	1.3840	1.3817 (0.0017)	4.5775	4.5399 (0.0082)
$\mathrm{I}_{xy}^{\mathrm{CM}}$ $(\mathrm{kgm}^2\cdot 10^{-3})$	0.0090	-0.0087 (1.9667)	0.0250	-0.2039 (9.1560)
$\mathrm{I}_{xz}^{\mathrm{CM}}$ $(\mathrm{kgm}^2\cdot 10^{-3})$	-0.0070	0.0030 (1.4286)	-0.1459	-0.0052 (0.9644)
$\mathrm{I}_{yz}^{\mathrm{CM}}$ $(\mathrm{kgm}^2\cdot 10^{-3})$	0.0060	0.0082 (0.3667)	0.0030	0.0021 (0.3000)
Number of iterations	4		4	

MATLAB simulations were run according to the proposed above sequence for CAD models of 1U and 3U CubeSats. One representative example of simulations is given here in details. The different dynamic characteristics of the payload and initial conditions are presented in Table 8. At the beginning of each experiment, the CubeSat is at rest and the axes of $\mathcal{F}_{bf}$ and $\mathcal{F}_{\text{fix}}$ are perfectly aligned. The scaling coefficients for $\mathbf{r}$ and the duration of each experiment, which depends on the magnitude of $\boldsymbol{\rho}^{\mathbf{o}}$ identified at the previous iteration, were found empirically and are given in Table 9. The sampling time for all iterations is 0.1 sec.

The results of the identification and the corresponding number of iterations, required to obtain $\boldsymbol{\rho}^{\mathbf{o}}$ with an accuracy of 1 μm (that is needed to meet disturbing torque requirements) are given in Table 10. Based on the conducted simulations of the identification process, better results are obtained when at least 4 experiments are made. In each experiment, the geometric center of the CubeSat is located in a different octant of $\mathcal{F}_{\text{fix}}$.

These simulations provide good results in the identification of the CoM location (largest error <0.1%) and of the moments of inertia (largest error <1%), but for the accurate identification of the products of inertia some additional measures might be needed. The latter can be explained by the small magnitudes of the products of inertia with respect to other identified values. However, the products of inertia should always be small due to the parallelepiped shape of the satellite and they are not important to the CubeSat balancing.

3.5 Conclusion

In this chapter three key topics of the AirBall testbed design were discussed: (i) the study of the air bearing Spheres motion; (ii) the determination of the Inner Sphere and CubeSat orientation by means of indirect measurements; (iii) the mass balancing technique. The developed techniques have been evaluated by means of numerical simulations, and their efficiency was presented. Summarizing the obtained results, several outcomes have to be highlighted:

- For the Inner and Outer Spheres assembly, the mounting of one of the air bearings with a constant force spring is a prospective design solution. It makes the relative motion of the Inner and Outer Spheres smoother even with large sphere clearance. Consequently, the requirements for the tolerances of the Spheres elements and for the precision of the assembly might be reduced that potentially simplifies the testbed manufacturing and lowers the required expenses.
- The determination of the Inner Sphere rotation is implemented by means of a measurement system composed of laser distance sensors. The sensors provide contactless measurements of the distances between certain elements of the "fixed" Outer Sphere and the rotating Inner Sphere. Between the two developed approached, the determination based on small angles approximation is selected. It requires only three sensors and provides acceptable accuracy of the determination in relatively large range of angles.
- The mass balancing system of the testbed is expected to be manual. Being free of actuators, it has small mass and dimensions. However, the system is not capable of providing actuation torques required for the payload CoM identification. The dynamic parameters identification using only a gravity torque was developed and verified my means of numerical simulations, which proved that efficiency of the identification techniques match the requirements on the residual testbed disturbances.

The developed mechanical design of the AirBall testbed and its prototype was presented within the previous chapter. In this chapter, the modeling required to prove the selected design is given. The following chapter is devoted to the experimental verification of the AirBall testbed prototype.

Chapter 4. AIRBALL EXPERIMENT

4.1 AIRBALL HARDWARE

The prototype of the AirBall testbed, shown in Figure 4.1-1, was manufactured as described in Section 2.3. However, several issues induced some necessary modifications to the previously described design.

- The active and passive parts of the air bearings were initially selected to be of the same diameter 40 mm. However, the amplitude of an acceptable misalignment (a range of the Inner Sphere rotation, where the air bearings keep their functions without any correction of the Outer Sphere orientation) is about 1° - 2°. This range is small and would make the experimental work more difficult. To deal with this issue, one of the air bearing parts has to be changed. It was decided to replace the 40 mm active part by another one with 25 mm diameter, as this modification is less costly than replacing the passive part. The maximum load for the new air bearings is smaller, but still enough for the selected payload.
- The first modification described above caused certain change in the fastening of the active parts of the air bearings: The new element does not have threaded holes that can be used for fixation. In order to prevent them from falling down, 3D printed holding cups have been involved, as shown in Figure 4.1-2.
- Once the AirBall was assembled, the influence of the air supply tubes appeared: The stiffness of the tubes affects angular position of the active part of the air bearing. Thus, the tension from the tubes prevails on the air bearing force, which was expected to auto-adjust the orientation of the passive parts. To deal with this issue, it was decided to adjust each passive part with 3 fine screws (Figure 4.1-2).

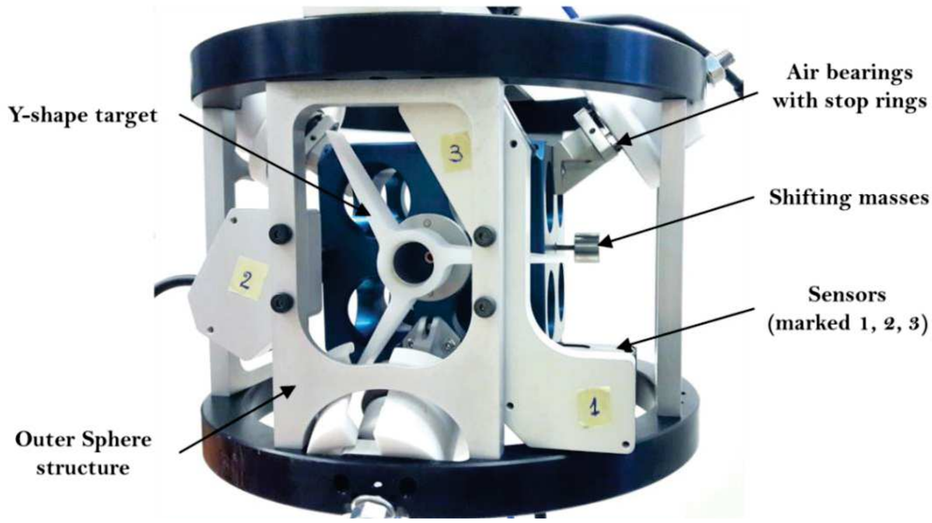

Figure 4.1-1 Assembled AirBall prototype

It shall be noted that due to this change in the design of the AirBall, the spring in one of the air bearing joint was removed. Indeed, when the passive parts are fixed with screws, their positioning requires manual adjusting with high accuracy. In this circumstance, using the spring in one of the air bearings is inconvenient since it brings more uncertainties than advantages.

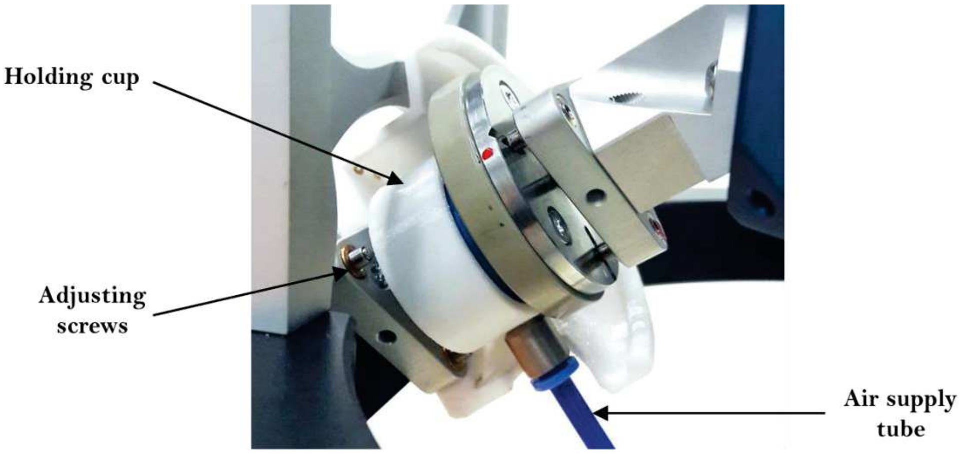

Figure 4.1-2 Air bearing close up

When the components were replaced, the adjustment of the air bearing positions has been done by hand. However, the achieved positioning accuracy was not enough for representative experimentations with the AirBall system and the system was sent back to the manufacturing company (Symétrie) for fine tuning.

At Symétrie, the AirBall was adjusted using precise measuring instruments. The position of each air bearing part was precisely tuned by means of 3 adjustment screws and controlled based on measurements obtained from dozens of points. Result of the positioning control for the Outer Sphere is shown in Figure 4.1-3. Despite the obvious complexity of this task, the AirBall was tuned with 13μm accuracy.

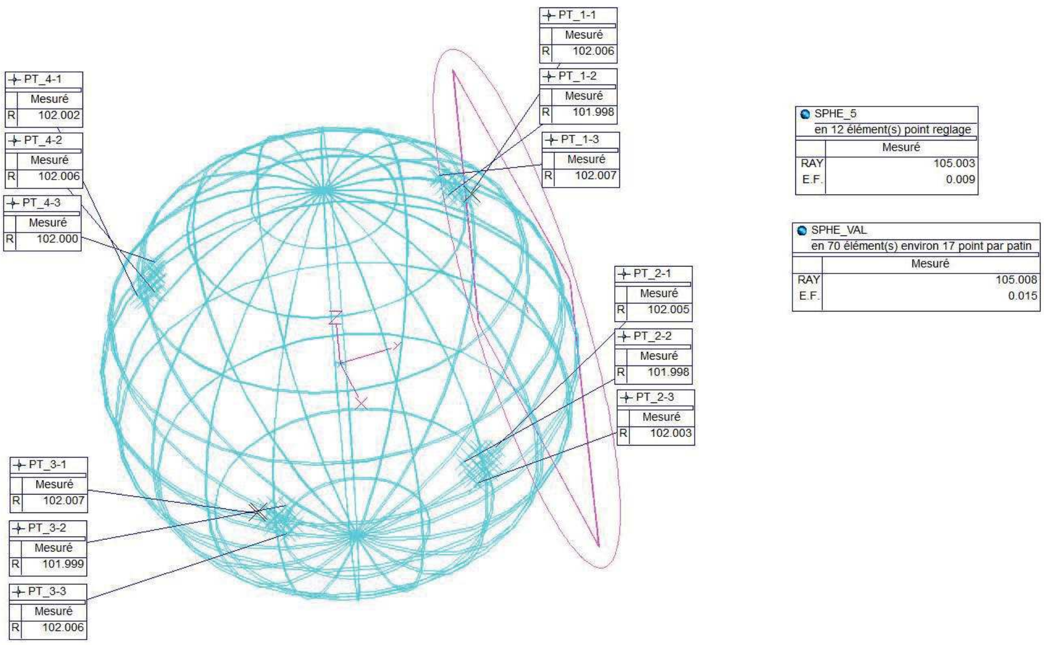

Figure 4.1-3 Fine tuning of the Outer Sphere. Nominal radius 105 mm (Note: Radius of the measuring probe 3 mm is subtracted)

While the air bearing spheres can potentially support unlimited rotations of the CubeSat mock-up, some constraints are caused by the robotic arm. According to the simulations presented in Section 2.3.3 and specified by preliminary tests, the Viper s650 provides the AirBall with the maximum rotation amplitude of ±90° around X; -30°, +40° around Y and ±360° around Z. Comparing to the desired unconstrained motion ranges, these values are relatively small, but they still allow the experimentations required to verify the AirBall concept.

The whole prototype of the AirBall testbed is shown in Figure 4.2-1. The masses and dimensions of the AirBall prototype components are summarized in Table 11.

Table 11 AirBall prototype characteristics

<table>
<tr><th></th><th></th><th>Dimensions, mm</th><th>Mass, kg</th><th>Comments</th></tr>
<tr><td rowspan="5">Air bearing Spheres</td><td>Structure</td><td>ø 238, h 194</td><td>2.62</td><td></td></tr>
<tr><td>Air bearings x 4</td><td>ø 25</td><td>0.014</td><td>Max. load 49 N</td></tr>
<tr><td>Passive parts x 4</td><td>ø 40</td><td>0.023</td><td></td></tr>
<tr><td>Stop rings x 4</td><td>ø 50, h 60</td><td>0.03</td><td></td></tr>
<tr><td>1U CubeSat Mock-up</td><td>100 x 100 x 100</td><td>1.00</td><td></td></tr>
<tr><td>Balancing system</td><td>Shifting masses x 6</td><td>ø 15, h 12</td><td>0.015</td><td>Max 15 mm shift</td></tr>
<tr><td rowspan="3">Measurement system</td><td>Laser Sensors x 3</td><td>48.5 x 33.5 x 22.6</td><td>0.06</td><td></td></tr>
<tr><td>Reference Y-shape Target</td><td>R72</td><td>0.025</td><td>3D printed plastic</td></tr>
<tr><td>Counter weight</td><td>ø 50, h 60</td><td>0.025</td><td></td></tr>
<tr><td>Total</td><td></td><td>ø 238, h 194</td><td>4.2</td><td></td></tr>
</table>

4.2 Robot Motion Control

4.2.1 Hardware architecture

Figure 4.2-2 shows an overview of the Viper robot control system, including its components, the AirBall sensors and communication protocols. The robot is directly connected to the dedicated controller Adept MotionBlox-60R (MB-60R). It is a distributed servo controller and amplifier, which is designed to power the motors of the Viper and to communicate, coordinate and execute servo commands. The MB-60R feature 6 AC servo motor amplifiers, the emergency stop circuitry, integral temperature sensors and status monitoring. The controller actuates the joint motors as 8 kHz and provides joint position control.

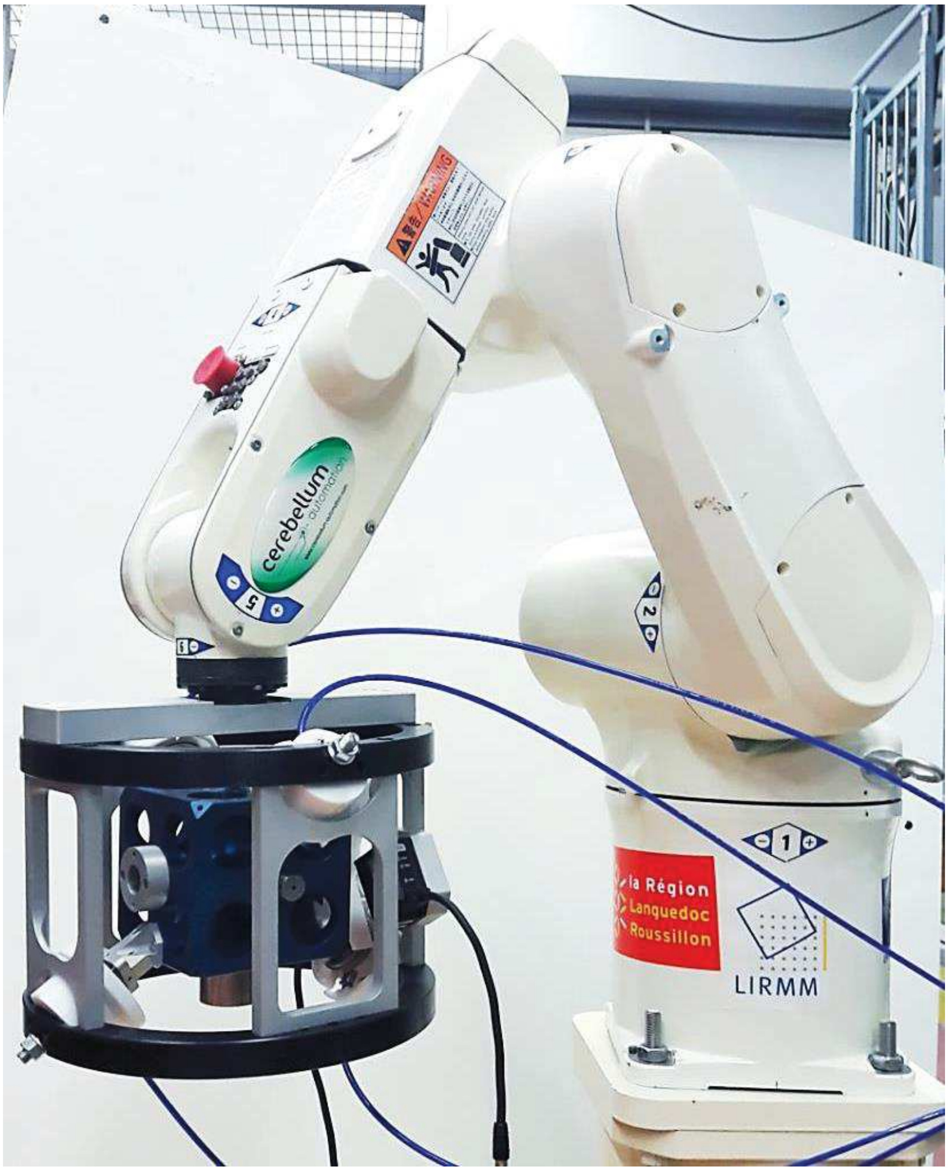

Figure 4.2-1 Complete view of the prototype: AirBall and Viper s650

The MB-60R must be connected to a user-supplied PC that provides setup, control and programming. In the current configuration of the system two PC are employed. The Viper is setup using a Windows PC with installed Cerebellum CIDE software. It allows loading the home configurations to the robot. Then, a PC with Linux RTAI provides the steering control in real time. It reads the Viper robot encoders and offers a new joint position reference at 1 kHz. Both PC are connected to the MB-60R by using the FireWire protocol.

The distance sensors are essential for implementing the control loop. Three Keyence IL-030 sensors are installed on the AirBall. Measurement data from them are collected by the data acquisition card (DAC) National Instruments 6220, which features up to 16 channels with ±10 V input range. The data is transmitted as analogue signal -5..+5 V that corresponds to the measurement range -5..+5 mm. The DAC is connected to the Linux PC by a PCI bus.

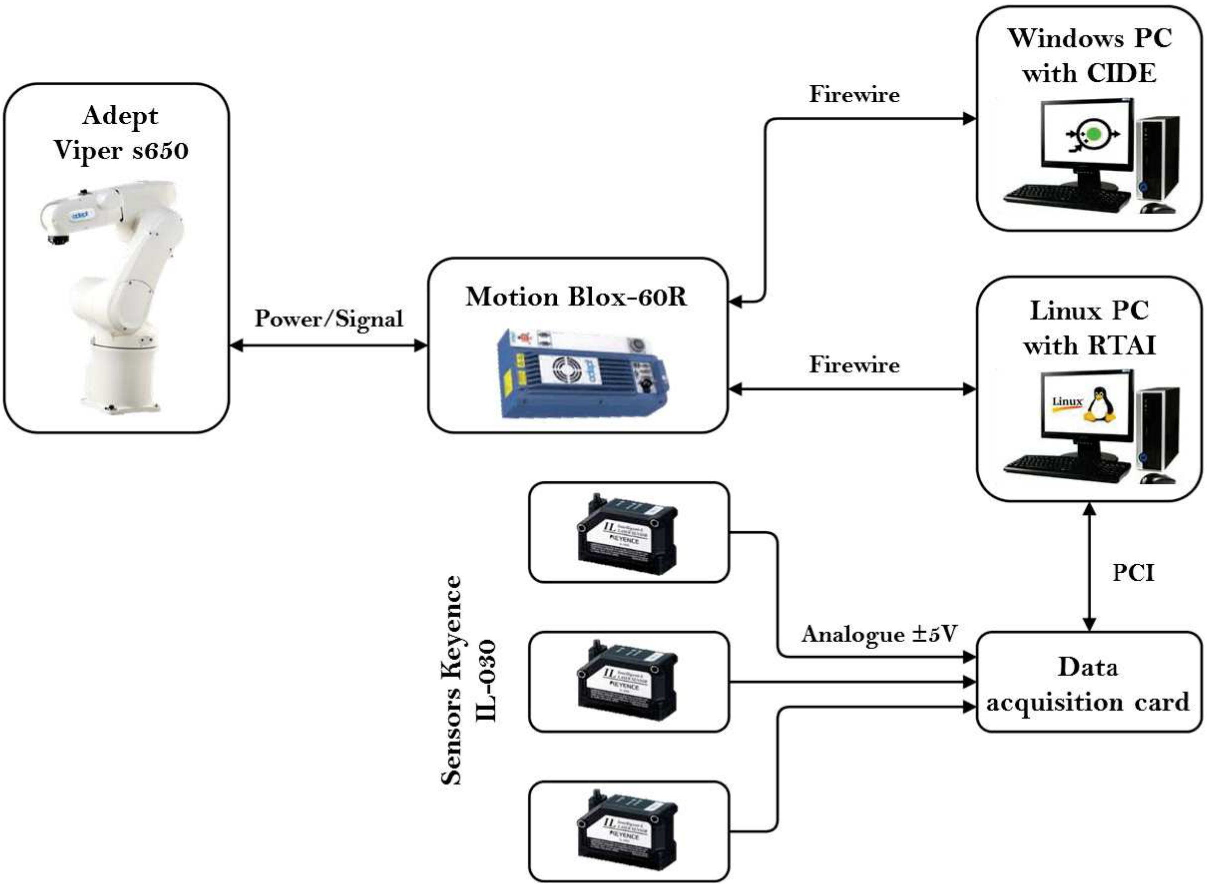

Figure 4.2-2 Robot control architecture

4.2.2 Control scheme

The main task of the Viper robot is to follow the rotation of the CubeSat mock-up in such a way that the passive and active parts of the air bearings are kept aligned. Because the trajectory of the desired motion cannot be predicted, the robot end-effector pose must be continuously updated based on the measurements from the sensors. The implemented control scheme is shown in Figure 4.2-3.

The Keyence IL-030 sensors measure the linear distances d_1, d_2 and d_3 to the related surfaces of the Y-shape reference target. These data are used to determine the relative orientation of the Inner and Outer Spheres, as it was described in Section 3.3.2. The orientation is represented by a rotation matrix ${}^{\mathbf{out}}\mathbf{R}_{\mathbf{inn}}$, which is further used in the robot end-effector pose planning.

The pose planning is intended to set a desired end effector position and orientation $\mathcal{X}_{des}$ in the Cartesian space. The robot has an embedded joint position controller, which receives output of the pose planning and directly actuates the torque-controlled robot joint motors. The current end-effector pose $\mathcal{X}$ is determined using encoder readings $\mathbf{q}_{encoder}$ and the forward kinematic model of the Viper. The knowledge of the current pose is required to calculate a desired pose $\mathcal{X}_{des}$.

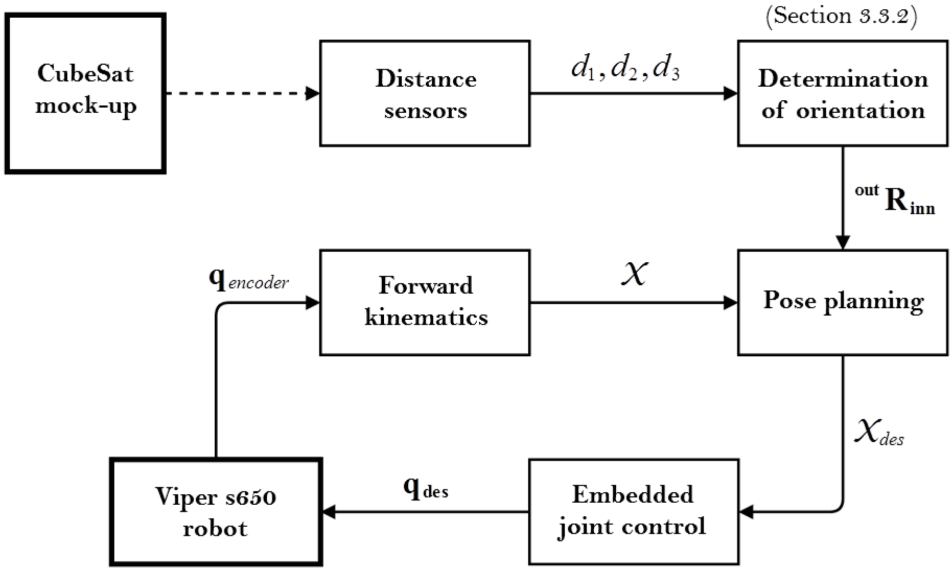

Figure 4.2-3 Steering control scheme

4.2.3 Pose planning

The pose planning part of the control routine implements the transformations between the involved coordinate frames in order to set a new pose of the end-effector. This pose has to ensure that the frames of the Inner and Outer Spheres remain coincident. Thus, getting the transformation from the Inner Sphere frame to the base frame is the goal of pose planning. All involved coordinate frames are shown in Figure 4.2-4.

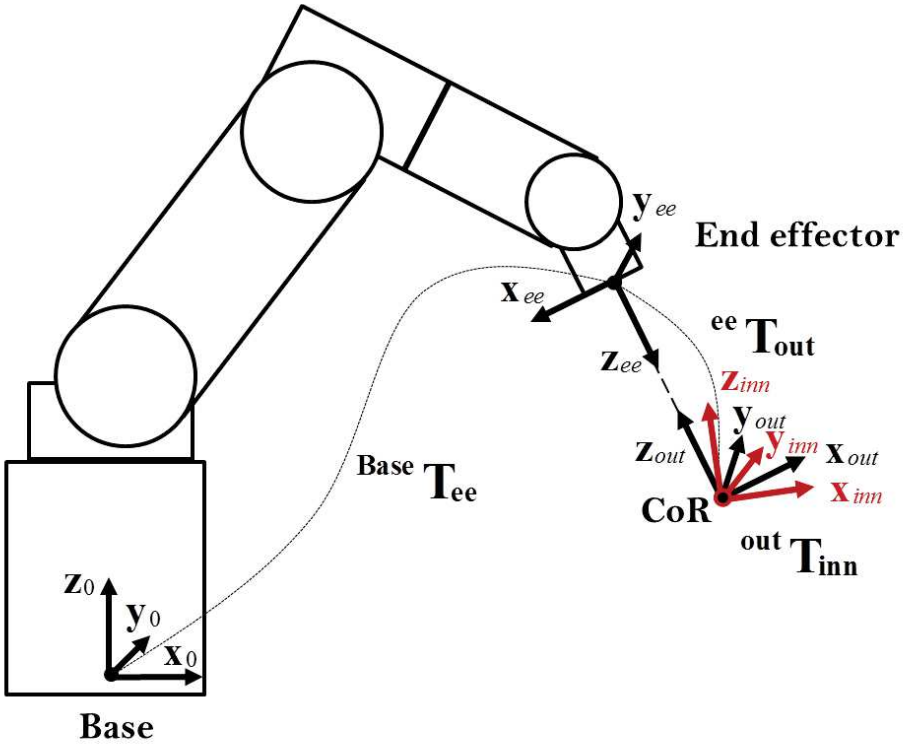

Figure 4.2-4 Coordinate frames and transformations

The current pose of the robot end effector X with respect to the base is described by the homogeneous transformation matrix [108]:

$$ {}^{\mathbf{Base}}\mathbf{T}_{\mathbf{ee}} = \begin{bmatrix} {}^{\mathbf{Base}}\mathbf{R}_{\mathbf{ee}} & {}^{\mathbf{Base}}\mathbf{p}_{\mathbf{ee}} \\ \mathbf{0} & 1 \end{bmatrix}, \tag{4.1} $$

where ${}^{\mathbf{Base}}\mathbf{R}_{\mathbf{ee}}$ is the rotation matrix defining the end-effector frame orientation and ${}^{\mathbf{Base}}\mathbf{p}_{\mathbf{ee}}$ is the vector of the end effector coordinates with respect to the base frame. The Outer Sphere is rigidly connected to the robot end-effector with an offset ${}^{ee}z_{CoR}$ along the $\mathbf{z}_{\mathbf{ee}}$ axis. Accordingly, the related transformation matrix is:

$$ {}^{\mathbf{ee}}\mathbf{T}_{\mathbf{out}} = \begin{bmatrix} {}^{\mathbf{ee}}\mathbf{R}_{\mathbf{out}} & {}^{\mathbf{ee}}\mathbf{p}_{\mathbf{CoR}} \\ \mathbf{0} & 1 \end{bmatrix}, \tag{4.2} $$

where ${}^{\mathbf{ee}}\mathbf{p}_{\mathbf{CoR}} = \begin{bmatrix} 0 & 0 & {}^{ee}z_{CoR} \end{bmatrix}^T$ is the vector of the aforementioned offset, ${}^{\mathbf{ee}}\mathbf{R}_{\mathbf{out}}$ is the rotation matrix written as:

$$ {}^{\mathbf{ee}}\mathbf{R}_{\mathbf{out}} = \begin{bmatrix} -1 & 0 & 0 \\ 0 & 1 & 0 \\ 0 & 0 & -1 \end{bmatrix} \tag{4.3} $$

The output from the determination of the Inner Sphere orientation with respect to the Outer Sphere (Section 3.3.2) is a rotation matrix ${}^{\mathbf{out}}\mathbf{R}_{\mathbf{inn}}$. Thus, the full transformation matrix for the Spheres is:

$$ {}^{\mathbf{out}}\mathbf{T}_{\mathbf{inn}} = \begin{bmatrix} {}^{\mathbf{out}}\mathbf{R}_{\mathbf{inn}} & \mathbf{0} \\ \mathbf{0} & 1 \end{bmatrix} \tag{4.4} $$

The desired pose of the robot end-effector must be such that the frames of both Spheres are coincident. Hence, the transformation between the desired end-effector pose and the base can be expressed as:

$$ \mathbf{T}_{\mathbf{des}} = {}^{\mathbf{Base}}\mathbf{T}_{\mathbf{ee}}\,{}^{\mathbf{ee}}\mathbf{T}_{\mathbf{out}}\,{}^{\mathbf{out}}\mathbf{T}_{\mathbf{inn}} \left[{}^{\mathbf{ee}}\mathbf{T}_{\mathbf{out}} \right]^{-1} \tag{4.5} $$

Thus, the homogeneous transformation matrix $\mathbf{T}_{\mathbf{des}}$ is further used in the embedded controller to generate the related joint coordinates and to move the Viper robot end-effector in the new pose.

4.3 RESIDUAL PERTURBATIONS

The main goal of the testbed is to provide a CubeSat with a low-torque environment. However, all perturbations caused by the testbed interaction with the environment of ground facility cannot be completely eliminated, but they can be estimated. The knowledge of the residual perturbations in the testbed will help to evaluate its performance.

4.3.1 Estimating perturbations

Perturbations that might occur on the testbed are notably caused by the following factors:

- Deformations of a CubeSat and its supporting structure due to internal forces that causes enlargement of the offset between CoM and CoR;
- Deformations of a CubeSat and its supporting structure due to changes in temperature;
- Aerodynamic flow due to CubeSat rotation;
- Friction in air bearings.

Deformations of testbed elements are considered negligible for the AirBall prototype. Indeed, the CubeSat mock-up and the elements of the Inner Sphere are stiff and do not experience large stresses. Moreover, the CubeSat mock-up does not generate energy, because it does not accommodate electrical components. Thus, the only heat source nearby the CubeSat mock-up is the distance sensors. According to the specification, each of them has 0.22 mW output of the light source. Assuming the total emitted energy is two orders of magnitude larger (in the worst case), three sensors provide 66 mW. This value is very small and it cannot yield any noticeable change in the mock-up temperature and, consequently, related deformations of the structure are small enough to be negligible.

For calculations of *the aerodynamic torque*, the following equation is used:

$$T_{aero} = S_{wetted} C_f \frac{\rho v^2}{2} r \tag{4.6}$$

where S_{wetted} is the wetted surface area (which is in contact with the aerodynamic flow) of a body, C_f is the coefficient for the laminar flow, ρ is the density of ambient air and v is the velocity of the body. Based on the CAD model, S_{wetted} for the Inner Sphere elements is $3 \cdot 10^{-2}$ m^2. Velocity v is 0.25m/s for $\omega = 5$ rad/s and $r = 0.05$ m. Air density is 1.225 kg/m^3. The coefficient C_f is assumed to be 2 (the worst case) that allows the compensation of potential errors caused by inaccuracies of values. The resultant aerodynamic torque is 0.45 mNm.

Compared with other types of bearings, air bearings provide an exceedingly low *friction force* due to contact-free motions. But the friction between the surfaces and the film of pressurized air still yields a minimized resisting force that shall be estimated for the AirBall prototype. Because analytical calculations of the friction torque in air bearings are very complex, experimentation data is more relevant to evaluate its magnitude.

Considering a body having one fixed point and oscillating due to gravity force, the energy dissipation is defined through the equation:

$$\Delta E = mg\Delta h \, , \tag{4.7}$$

where ΔE is the energy dissipation due to damping of the body motion for a certain time period, m is the mass of the body, Δh is the change in maximum elevation of the body for the same time period, and g is the acceleration due to gravity.

Applying equation (4.7) to the AirBall testbed prototype, the energy dissipation ΔE is used to estimate work done by the aerodynamic and friction torques as follows:

$$T_{aero}\Delta\alpha + T_{fr}\Delta\alpha = mg\Delta h\ , \tag{4.8}$$

where T_{fr} is the friction torque and $\Delta\alpha$ is the change in angular coordinate. Thus, in order to estimate the influence of the perturbation factors, the motion of the Inner Sphere shall be sampled for several oscillation periods. Details of the experimental estimation of the perturbation torques are given in the following sub-section.

4.3.2 Experiment planning

The experiment aimed at estimating the perturbations on the AirBall testbed prototype involves free oscillation motions of the Inner Sphere. Thus, an offset between the CoM of the Inner Sphere and the CoR shall be provided. Because the orientation of the vertical plane of motion does not contribute into results of the experiment, any plane containing the vertical axis can be selected.

For this experiment, the plane $\mathbf{Oy_0z_0}$ is selected and the CoM position is shifted along axis $\mathbf{y_{inn}}$ of the Inner Sphere (Figure 4.2-4). To this end, one shifting mass is added to the well balanced CubeSat mock-up. When the Inner Sphere is released, its motion is sampled by the sensors. The obtained rotation matrix is:

$${}^{\mathbf{0}}\mathbf{R}_{\mathbf{inn}} = \begin{bmatrix} {}^{\mathbf{0}}\mathbf{x}_{\mathbf{inn}} & {}^{\mathbf{0}}\mathbf{y}_{\mathbf{inn}} & {}^{\mathbf{0}}\mathbf{z}_{\mathbf{inn}} \end{bmatrix} \tag{4.9}$$

where the motion of the axis $\mathbf{y_{inn}}$ of the Inner Sphere is defined by the second component:

$${}^{\mathbf{0}}\mathbf{y}_{\mathbf{inn}} = \begin{bmatrix} \mathbf{y}_{\mathbf{inn}}\cdot\mathbf{x_0} & \mathbf{y}_{\mathbf{inn}}\cdot\mathbf{y_0} & \mathbf{y}_{\mathbf{inn}}\cdot\mathbf{z_0} \end{bmatrix} \tag{4.10}$$

Being given the Inner Sphere motion for n oscillation periods, equation (4.8) is used to find the perturbation torques. To this end, the change in the maximum elevation of the Inner Sphere is:

$$\Delta h = \left(\mathbf{y}_{\mathbf{inn}}\cdot\mathbf{z_0}\right)_{\max 1} - \left(\mathbf{y}_{\mathbf{inn}}\cdot\mathbf{z_0}\right)_{\max n} \tag{4.11}$$

The change in angular coordinates is:

$$\Delta\alpha = 4n\left(\pi - \cos^{-1}\left(\mathbf{y}_{\mathbf{inn}}\cdot\mathbf{z_0}\right)_{\max 1}\right), \tag{4.12}$$

if the CoM lies on the axis $\mathbf{y_{inn}}$, then $\Delta\alpha = 2\pi n$.

Being given the mass m of the Inner Sphere, the total perturbation torque is found as:

$$T_{aero} + T_{fr} = \frac{mg\Delta h}{\Delta\alpha} \tag{4.13}$$

And the friction torque is:

$$T_{fr} = \frac{mg\Delta h}{\Delta\alpha} - 0.45\cdot 10^{-3}[\mathrm{Nm}] \tag{4.14}$$

4.4 EXPERIMENT RESULTS AND DISCUSSIONS

4.4.1 Friction torque in the AirBall testbed prototype

In order to minimize the computational error and influences of the robot dynamics, it was decided to study the motion of the AirBall within a small range of angles (constrained by the stop rings), where the robot is not moving. The AirBall orientation in this experiment and the numbering of the sensors are shown in Figure 4.4-1.

The Inner Sphere has a certain misbalance: At the equilibrium state, the active and passive parts of the air bearings are misaligned, but the passive parts remain within the stop rings free space. The Inner Sphere is turned away from its equilibrium state by hand and released. The direction of the initial inclination is selected so that the passive parts of the air bearings do not reach the stop rings, when the Inner Sphere oscillates. The distance sensors sample the Inner Sphere motion and the obtained measurements are plotted in Figure 4.4-2. These plots well illustrate the periodic character of the motion and the presence of damping.

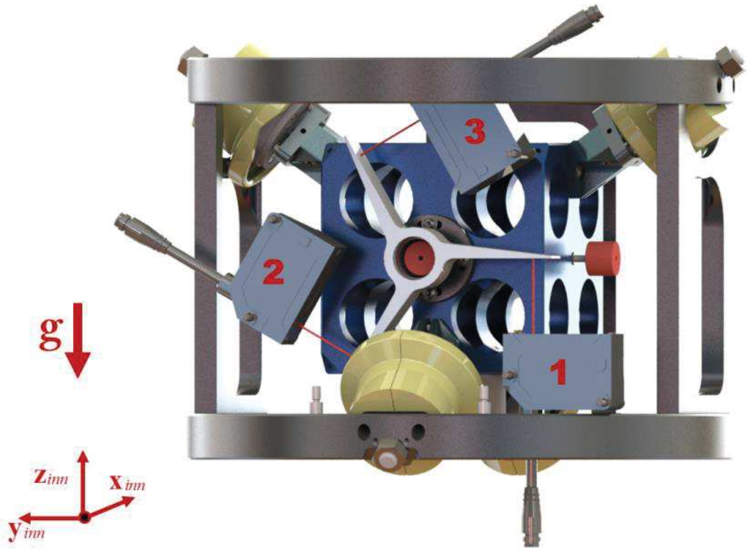

Figure 4.4-1 Numbering of the sensors arranged on the AirBall

In order to estimate the friction torque in the AirBall, equation (3.69) from Chapter 4 is used. The values obtained from the sensors cannot be directly substituted in (4.14), because they show linear motion of the Y-shape. Thus, at first, the Inner Sphere attitude shall be obtained in small angles, as it was described in Section 3.3, devoted to the determination of the CubeSat orientation:

$$\boldsymbol{\delta} = \mathbf{A}\mathbf{s} \tag{4.15}$$

where $\boldsymbol{\delta}$ is the vector composed of three measured distances, obtained by the sensors, $\mathbf{s}$ is the vector composed of three small angles, which describe the Inner Sphere orientation, and $\mathbf{A}$ is the matrix, which maps the small angles to the linear measurements. In order to fit the sensor layout in Figure 4.4-1, the matrix $\mathbf{A}$ given by equation (3.23) in Chapter 3 is modified as follows:

$$\mathbf{A} = \begin{bmatrix} d & -R & 0 \\ d & \frac{1}{2}R & -\frac{\sqrt{3}}{2}R \\ d & \frac{1}{2}R & \frac{\sqrt{3}}{2}R \end{bmatrix} \tag{4.16}$$

where d is the distance from the center of the Y-shape to the measurement beam and R is the distance from the center of the Inner Sphere to the plane of measurements. For the AirBall design $d = 53.455$ mm and $R = 73.31$ mm. In order to find the absolute elevation angle of the Inner Sphere, the transformation between the small angles and the angle-axis representation of orientation is applied.

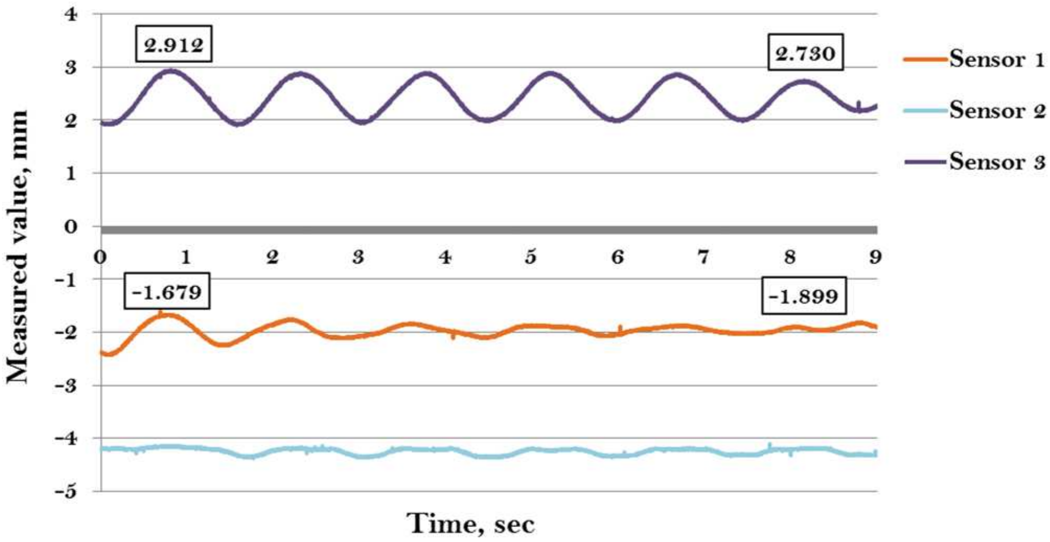

Figure 4.4-2 Measurements obtained from the sensors during the Inner Sphere oscillation

Thus, the elevation angle θ is found as follows:

$$\theta = 2\cos\left(c_1 c_2 c_3 - sn_1 sn_2 sn_3\right), \tag{4.17}$$

where $c_i = \cos\left(\frac{s_i}{2}\right)$ and $sn_i = \sin\left(\frac{s_i}{2}\right)$.

Then, the elevation of the Inner Sphere is:

$$h = R\sin(\theta) \tag{4.18}$$

and the change of the elevation is:

$$\Delta h = h_1 - h_n , \tag{4.19}$$

where h_1 and h_n are the values of the elevation at the 1st and nth oscillation periods, respectively.

Being given the mass of the Inner Sphere $m = 1.45$ kg, the number of the analyzed oscillation periods $n = 5$, $\Delta\alpha = 4\bar{\theta}n$ and the measurements in Figure 4.4-2, the friction torque is calculated. The estimated friction torque in the AirBall testbed prototype is 0.02 Nm.

4.4.2 AirBall testbed prototype functional tests

In order to prove the general operability of the whole prototype, comprising the AirBall and the Viper s650 robot, functional tests have been performed. The tests were conducted in two phases: Open-loop and closed-loop tests.

During the open-loop test, the AirBall is not connected physically to the robot. However, the sensor measurements are used to generate the synchronic end-effector trajectory. The AirBall is supplied by the air that allows a free motion of the Inner Sphere. Since the robot does not hold the Outer Sphere, this motion is possible within a small range of angles only. This range is defined by the dimensions of the stop rings. The goal of this experiment is to check the sensors data handling and the implemented robot control. In case of the appropriate performance of all components of the prototype, the robot end effector carefully repeats the trajectory of the motion manually applied to the Inner Sphere. In other words, the Inner Sphere can be used as a joystick to control the motion of the robot. The open-loop tests require minor modification in the robot control. Using the notion defined in Section 4.2, the transformation between the desired end-effector pose and the base for the open-loop tests is:

$$\mathbf{T}_{\mathbf{des}} = {}^{\mathbf{Base}}\mathbf{T}_{\mathbf{home}}\,{}^{\mathbf{ee}}\mathbf{T}_{\mathbf{out}}\,{}^{\mathbf{out}}\mathbf{T}_{\mathbf{inn}}\left[{}^{\mathbf{ee}}\mathbf{T}_{\mathbf{out}}\right]^{-1}, \tag{4.20}$$

where ${}^{\mathbf{Base}}\mathbf{T}_{\mathbf{home}}$ is the transformation matrix defining the home end-effector position in the base frame. The prototype successfully passed this phase of the experimentation (Figure 4.4-3 and Figure 4.4-4). As an extension of this test, the motion of the assembled system was tried for small ranges of motion.

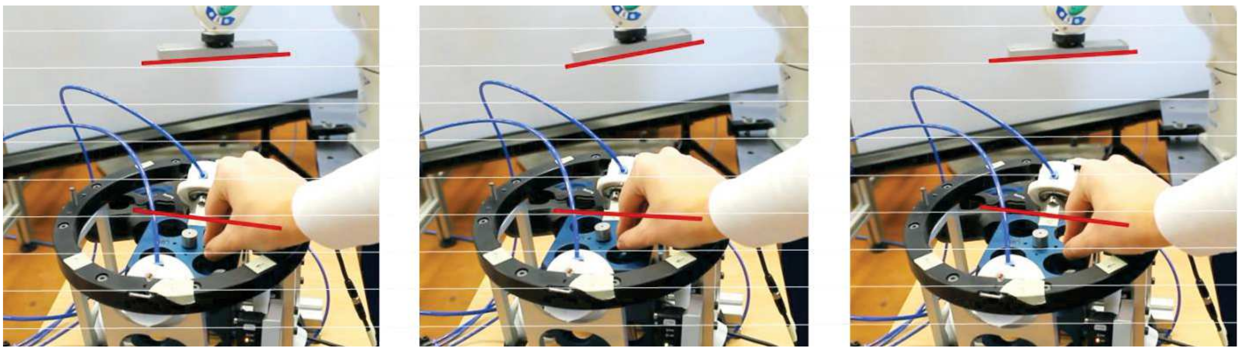

Figure 4.4-3 Open-loop test, camera 1

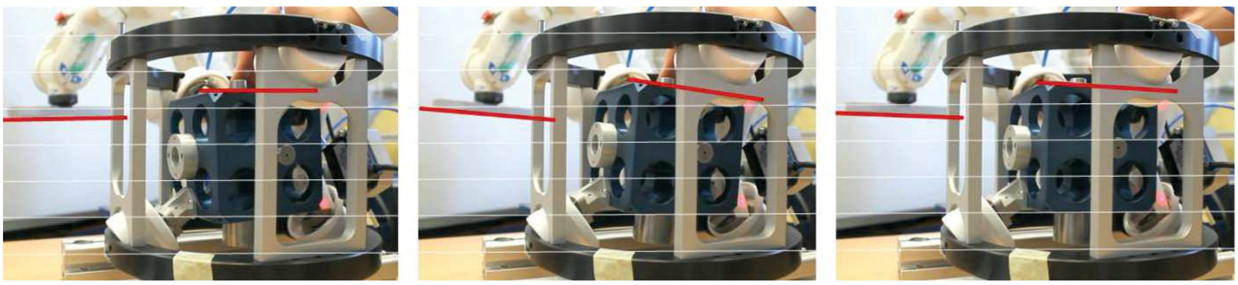

Figure 4.4-4 Open-loop test, camera 2

During the closed-loop test, the AirBall is attached to the Viper robot and the control is implemented as it was described in Section 4.2. The goal of this phase of the experiment is to prove the whole prototype operation in a wider range of angles. The closed-loop tests were successfully performed for different trajectories of the CubeSat mockup (Figure 4.4-5). It shall be noted, that in the experiments the maximum velocity of the robot was limited to 20% of maximum values due to safety reasons.

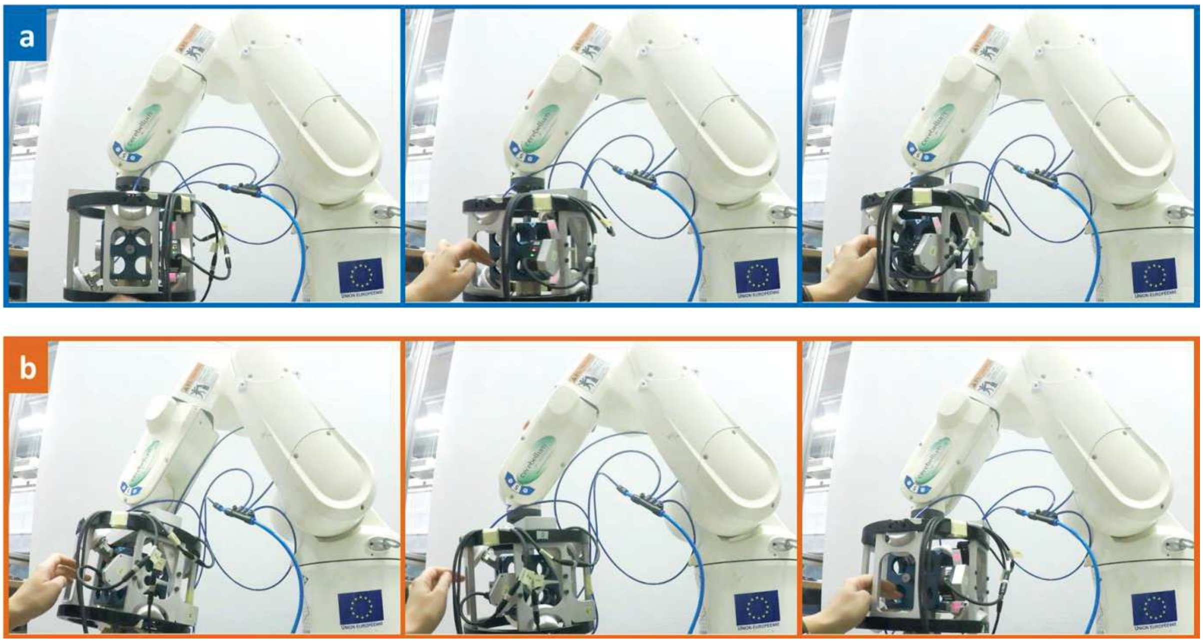

Figure 4.4-5 Closed-loop test. CubeSat mockup is pushed counterclockwise (a) and clockwise (b)

4.4.3 Discussions on the experiment results

The performed experiments with the AirBall testbed prototype prove the feasibility of the concept proposed in this thesis. However, there is room for further improvements. One of the aspects to be improved on future steps is the friction torque. Currently, the friction torque in the system achieves 0.02 Nm, which is higher than the expected value. The experiment used for the friction torque estimation was conducted in very small ranges of angles, when the oscillation is constrained by the stop rings. While the oscillation motion was carefully controlled, slight contact of the Inner Sphere with the stop rings could take place. This would obviously affect the resultant friction torque. In future works, it is thus recommended to estimate the friction based on the motions with the wider ranges of angles.

Another undesired effect was revealed during the experimentations: At certain angles, the AirBall experience noticeable vibrations. Three possible causes are guessed:

- Uncontrolled perturbations in the air flow
- Aerodynamic effects in the air bearing assembly
- Resonance of the frequencies of the Inner and Outer Spheres.

Fluctuations of the air flow can be a result of the imperfections in the air supply system at some level (in the tubing, filtration unit, pressure controller or the pump). Using a capacious air tank can help to deal with this problem. Aerodynamic effects in the AirBall may also be the source of the vibrations. The use of four spherical air bearings is an unusual design solution, and a detailed aerodynamic study will definitely contribute to the understanding of the AirBall behavior. Moreover, a comprehensive modal analysis of the structure is recommended to find the frequencies of the Inner and Outer Spheres that will help to avoid the resonance.

4.5 Conclusion

This chapter illustrated the recent progress in developing the AirBall testbed. The organization of the experiment aimed at evaluating the efficiency of the AirBall prototype is presented. Based on preliminary tests of the prototype, several modifications have been implemented in the design of the Spheres in order to keep their performance as expected. Additionally, the control architecture for the Viper s650 robot is presented. The proposed control strategy provides the robot with a proper motion to follow the CubeSat mock-up trajectory.

In order to evaluate the efficiency of the AirBall testbed against residual perturbations, the torques induced by the prototype and the related environment are estimated. The torques caused by the deformations of the Inner Sphere are neglected due to small sizes and sufficient stiffness of the structure. The torque due to the aerodynamic drag is calculated considering several approximations. The torque due to friction force in the air bearings is difficult to be assessed by means of calculations. However, experiments have been conducted to estimate the total perturbation torque. Results of the experiment help (i) to prove efficiency of the proposed testbed concept and (ii) to quantify the low-torque environment provided by the AirBall prototype that is critical for further development of the AirBall testbed.

CONCLUSION AND PERSPECTIVES

This thesis documents the design and development of the air bearing testbed for CubeSat ADCS HIL ground testing. This work is motivated by a review of the statistics on CubeSat class nanosatellites and a detailed State-of-Art of the systems for testing CubeSat ADCS. In the last years, the number of launched CubeSats has constantly grown, but not all of them succeed. Less than half of CubeSat missions achieved their goals (either partly or completely). Analysis of failures showed that the most evident cause was a lack of proper component-level and system-level CubeSat verification. The trend towards using CubeSats for a wide range of space missions led to a more complex architecture of CubeSat subsystems. As results, risks of CubeSat mission failure got larger.

The weakest point of CubeSat ground tests is the examination of ADCS performance, because it requires reliable simulations of the space environment and CubeSat dynamics at same time. First systems, which provided such conditions, were designed in the early 1960s for the needs of pioneer satellites. Since then, means of satellite ADCS ground testing did not advance greatly. Despite long history of the satellite testing, the overview of the literature about testbeds showed that there are only very few testbeds suitable for CubeSats and nanosatellites ADCS. Thus, the deficit of testbeds matching CubeSats needs stresses the necessity to develop a brand-new system for these purposes.

Being compared with the testbeds known in literature, the concept proposed in this thesis and called AirBall, features an extended range of rotation and a low level of disturbances. These characteristics are critically important for reliable experiments including CubeSat dynamics. The novelty of the AirBall design is using four air bearings instead of one. The air bearings are settled together to shape a common spherical surface that allows avoiding geometrical constrains of the CubeSat motion, usually featured by the air bearing platforms, and provides unconstrained rotation. However, this feature will not be achieved without keeping active and passive parts of the air bearings aligned, while the CubeSat rotates. To this end, using a robotic gimbal is suggested. Its goal is to move the active parts of air bearings and to keep this motion coordinated with the independent rotation of the CubeSat. The basic design of the 4DoF kinematically redundant robotic gimbal is presented.

A reasonable first step towards constructing such a complex system as a testbed is building a prototype. The prototype of the AirBall testbed was constructed and tested, involving the Viper s650 robot instead of the gimbal. The prototype does not provide full functionality of the proposed testbed, but it is still a great advance in its development. First experimentations with the AirBall prototype proved feasibility of the implemented concept and give a large prospect for further advances.

In order to complete the development of the AirBall testbed, several related subtasks are solved in the thesis:

- The behavior of the sphere built of four air bearings is studied. Related simulations are conducted in order to prove the feasibility of the designed solution. Based on the obtained results, it was recommended to use a spring for mounting of one of the air bearings. This allows reducing tolerance requirements applied to the air bearing assembly.

- Two approaches to the determination of CubeSat orientation by means of indirect measurements were proposed. Capability and constrains of the approaches are compared based on results of numerical simulations. One solution is implemented on the AirBall prototype.
- A mass balancing technique suitable for testbeds without actuators is designed and verified by means of numerical simulation. The results showed that due to iterative approach, sufficient accuracy of mass balancing can be achieved.

Summarizing the experience acquired in this thesis, some recommendations concerning future advances of the AirBall testbed can be formulated. The most obvious recommendation for further steps of work is to replace the Viper robot by the designed 4DoF robot or by other manipulator with a larger operational workspace. This will allow truly unconstrained rotation of the testbed payload. When the free rotation will be obtained, the testbed will achieve next technology readiness level, and the full scale technology demonstration could be performed. Within this demonstration, CubeSat mock-up will be equipped with actuators in order to generate trajectories more complex than a swing of a gravity pendulum.

Next step to improve the AirBall testbed is rebuilding the Inner Sphere in such a way that it is able to accommodate any CubeSat. Currently, the CubeSat mock-up is an integral part of the Inner Sphere. The related task is implementing the adjustment mechanism, which positions a CubeSat inside the Inner Sphere and allows mass balancing without shifting masses. The basic concept of the adjustment mechanism is proposed in this thesis, but it requires several improvements in order to satisfactorily perform.

When experimentations with AirBall are completed, the testbed will be used for CubeSat ADCS testing. To this end, space factors essential for ADCS sensor operations shall be simulated on the test facility. Typical solutions for simulating sun, starry sky and near-Earth magnetic field are also reviewed in this thesis.

In the thesis conclusion, it must be highlighted that the first-of-its-kind system was developed for CubeSat ADCS tests. The system merges an air bearing platform with a robotic gimbal in order to achieve a highly demanded performance. The prototype of the testbed successfully confirmed the novel concept. It gives a significant impulse for further work in this domain in order to create a full functional testbed with the capacity for unconstrained CubeSat rotation in a low-torque environment.

BIBLIOGRAPHY

[1] H. Heidt, P. J. Puig-suari, P. A. S. Moore, P. S. Nakasuka, and P. R. J. Twiggs, "SSC00-V-5 Experimentation."

[2] M. Swartwout, "CubeSat DataBase," *Saint Louis University*, 2015. [Online]. Available: https://sites.google.com/a/slu.edu/swartwout/home/cubesat-database. [Accessed: 19-May-2016].

[3] T. U. of Denmark, "DTUsat-1." [Online]. Available: http://dtusat1.dtusat.dtu.dk/. [Accessed: 19-May-2016].

[4] Michael Swartwout and M. Swartwout, "The First One Hundred CubeSats : A Statistical Look," *J. Small Satell.*, vol. 2, no. 2, pp. 213–233, 2013.

[5] JAXA, "Japan Aerospace Exploration Agency," 2011. [Online]. Available: http://iss.jaxa.jp/en/kiboexp/jssod/. [Accessed: 19-May-2016].

[6] NanoRacks, "NanoRacks CubeSat Deployer (NRCSD) Interface Control Document." [Online] Available: http://nanoracks.com/resources/documents/. [Accessed: 19-May-2016]

[7] CalPoly, "Cubesat design specification." [Online] Available: http://www.cubesat.org/resources/. [Accessed: 19-May-2016]

[8] A. Chin, R. Coelho, R. Nugent, R. Munakata, and J. Puig-Suari, "CubeSat: The Pico-Satellite Standard for Research and Education," in *AIAA SPACE 2008 Conference & Exposition*, American Institute of Aeronautics and Astronautics, 2008

[9] J. R. Wertz and W. Larson, *Space Mission Analysis and Design*. Springer, 1999.

[10] E. S. S. Foundation, "ESTCUBE-1." [Online]. Available: http://www.estcube.eu/en/estcube-1. [Accessed: 19-May-2016].

[11] K. Lori, "Lunar IceCube to Take on Big Mission From Small Package." [Online]. Available: http://www.nasa.gov/feature/goddard/lunar-icecube-to-take-on-big-mission-from-small-package [Accessed: 19-May-2016]

[12] Pumpkin Inc., "Cubesat Kit FAQ." [Online]. Available: http://www.cubesatkit.com/content/faq.html. [Accessed: 19-May-2016].

[13] "Clyde Space Products," 2016. [Online]. Available: https://ww.clyde.space/products.

[14] "CubeSatShop.com." [Online]. Available: http://www.cubesatshop.com/. [Accessed: 19-May-2016].

[15] "SpaceFlight101.com," *Flock 1/2 – Planet Labs Earth Observation Satellites.* [Online]. Available: http://spaceflight101.com/flock. [Accessed: 19-May-2016].

[16] F. Corporation, "Planet Labs," *Flock 1*, 2013. [Online]. Available: https://www.planet.com/flock1/. [Accessed: 19-May-2016].

[17] M. Buscher, "TUB Small Satellite Database," 2014. [Online]. Available: https://www.raumfahrttechnik.tu-berlin.de/menue/publikationen/small_satellite_database/parameter/en/.

[18] W. H. Jones, *The Design and Simulated Performance of the Attitude Determination and Control System of a Gravity Gradient Stabilized Cube Satellite*, Lulu.com, 2015.

[19] V. Yudintsev, "CubeSat separation dynamics: models and experiment," *2nd IAA Latin American CubeSat Workshop*, 2016.

[20] C. Bernal and M. Van Bolhuis, "Releasing the Cloud: A Deployment System Design for the QB50 CubeSat Mission," *Small Satell. Conf.*, pp. 1–6, 2012.

[21] "SwissCube story." [Online]. Available: http://swisscube.epfl.ch/pages/page23.html. [Accessed: 19-May-2016].

[22] "AAUSAT3." [Online]. Available: http://www.space.aau.dk/aausat3/index.php?n=Main.First100Days. [Accessed: 19-May-2016].

[23] "Launched from Vostochny satellite SamSat transmitted fragmentary signals" [Online]. Available: http://rbth.com/news/2016/05/04. [Accessed: 19-May-2016].

[24] A. Zak, "Soyuz completes historic first mission from Vostochny," *RussianSpaceWeb.com*, 2016.

[25] B. Howley, "Overview of Spacecraft Attitude Determination and Control." *Lockheed Martin Space Systems Company*

[26] F. L. Markley and J. L. Crassidis, *Fundamentals of Spacecraft Attitude Determination and Control.* Springer New York, 2014.

[27] J. Wertz, *Spacecraft Attitude Determination and Control.* Springer, 1990.

[28] P. Fortescue and J. Stark, *Spacecraft System Engineering.* Wiley, 2003.

[29] V. A. Chobotov, *Spacecraft Attitude Dynamics and Control.* Krieger, 1991.

[30] ECSS, "ECSS-E-ST-10-02C Verification," no. March, p. 45, 2009.

[31] M. Cho, H. Masui, T. Hatamura, K. Date, H. Shigekatsu, and O. Shoichi, "Overview of Nano-satellite Environmental Tests Standardization Project : Test Campaign and Standard Draft," *26th Annu. AIAA/USU Conf. Small Satell.*, p. 11, 2012.

[32] "ISO 15864 Space systems - General test methods for space craft, subsystems and units," vol. 08, 2004.

[33] National Aeronautics and Space Administration, "NASA-STD-7002A Payload Test Requirements," 2004.

[34] NASA Goddard Space Flight Center, "GSFC-STD-7000 General environmental verification standard," p. 203, 2013.

[35] JAXA, "JERG-2-002 General Engineering Requirement Guidance," 2012.

[36] Space and Missile Systems Center, "SMC-S-016 Test Requirements for Launch, Upper-Stage, and Space Vehicles," vol. 2004, no. March, pp. 1–14, 2014.

[37] "ISO/TC 20/SC 14 N 1004 Space systems —Design Qualification and Acceptance Tests of Small- scale Satellites and Units Seeking Low-cost and Fast-Delivery," 2014.

[38] ECSS, "ECSS-E-ST-10-04C Space environment," no. November, p. 198, 2008.

[39] S. Corpino and F. Stesina, "Verification of a CubeSat via hardware-in-the-loop simulation," *IEEE Trans. Aerosp. Electron. Syst.*, vol. 50, no. 4, pp. 2807–2818, 2014.

[40] F. Stesina, S. Corpino, and L. Feruglio, "STARSIM: A Stand-Alone Tool for 'In The Loop' Verification," *Iac-15*, pp. 1–12, 2015.

[41] A. Tambini, F. Antonini, A. Corbelli, and F. Rossi, "Solar Array Simulator for Microsatellites Power System Testing," *Espc2011*, vol. 2011, no. 2, pp. 1–4, 2011.

[42] P. Gavigan, "Design, Test, Calibration and Qualification of Satellite Sun Sensors, Power Systems and Supporting Software Development," M.A. thesis, University of Toronto, Canada, 2011.

[43] T. Bank, "Characterizing a star tracker with built in attitude estimation algorithms under the night sky," *SPIE Proc. Ser.*, pp. 264–274.

[44] G. Rufino, D. Accardo, M. Grassi, G. Fasano, A. Renga, and U. Tancredi, "Real-time hardware-in-the-loop tests of star tracker algorithms," *Int. J. Aerosp. Eng.*, vol. 2013, 2013.

[45] J. A. Tappe, "Development of star tracker system for accurate estimation of spacecraft attitude," M.A. thesis, Naval Postgraduate School, Monterey, California, 2009.

[46] "SPUTNIX - Facility for microsatellites." [Online]. Available: http://www.sputnix.ru/en/products/test-stands-system/item/365-sx-150. [Accessed: 15-Jun-2016].

[47] M. A. Samaan, S. R. Steffes, and S. Theil, "Star tracker real-time hardware in the loop testing using optical star simulator," *Adv. Astronaut. Sci.*, vol. 140, no. January, pp. 2233–2245, 2011.

[48] S. Voronkov, "The Dynamic Test Equipment for the Star trackers processing." [Online]. Available: http://www.dlr.de/Portaldata/49/Resources/dokumente/archiv5/1008P_Voronkov.pdf. [Accessed: 15-Jun-2016].

[49] A. E. Ruark and M. F. Peters, "Helmholtz Coils for Producing Uniform Magnetic Fields," *J. Opt. Soc. Am.*, vol. 13, no. 2, pp. 205–212, 1926.

[50] A. Balogh et al., "The magnetic field investigation on the ULYSSES mission - Instrumentation and preliminary scientific results," *Astron. Astrophys. Suppl. Ser. (ISSN 0365-0138)*, vol. 92, no. February, pp. 221–236, 1992.

[51] R. Vernier, T. Bonalksy, and J. Slavin, "Goddard Space Flight Center Spacecraft Magnetic Test Facility Restoration Project," 2004.

[52] M. Misakian, "Equations for the Magnetic Field Produced by One or More Rectangular Loops of Wire in the Same Plane," *J. Res. Natl. Inst. Stand. Technol.*, vol. 105, no. 4, pp. 557–564, 2000.

[53] F. M. Poppenk, R. Amini, and G. F. Brouwer, "Design and application of a Helmholtz cage for testing nano-satellites," *Eur. Sp. Agency, (Special Publ. ESA SP*, no. 639 SP, 2007.

[54] S. Kelley, "A Three Degrees of Freedom Test Bed for Nanosatellite Avionics." [Online]. Available: https://stemn.com/projects/a-three-degrees-of-freedom-test-bed-for-nanosatellite-avionics. [Accessed: 15-Jun-2016].

[55] A. Klesh, S. Seagraves, M. Bennett, D. Boone, J. Cutler, and H. Bahcivan, "Dynamically driven Helmholtz cage for experimental magnetic attitude determination," *Adv. Astronaut. Sci.*, vol. 135, pp. 147–160, 2010.

[56] S. Chesi, "A Dynamic Hardware-in-the-Loop Three-Axis Simulator of Nanosatellite Dimensions," vol. 4, no. 1, pp. 1–22, 2015.

[57] J. Li, M. Post, T. Wright, and R. Lee, "Design of Attitude Control Systems for CubeSat-Class Nanosatellite," *Journal of Control Science and Engineering*, vol. 2013, Article ID 657182, 15 pages, 2013

[58] M. K. Quadrino, D. Miller, and K. Cahoy, "Testing the Attitude Determination and Control of a CubeSat with Hardware-in-the-Loop," M.A. tesis, MIT, 2014.

[59] G. A. Smith, "Dynamic Simulators for Test of Space Vehicle Attitude Control Systems," *Proceedings of the Conference on the Role of Simulation in Space Technology*, Part C, Virginia Polytechnic Inst. & State University, Blacksburg, VA, 1964, pp. XV-1–XV-30.

[60] O. Han, D. Kienholz, P. Janzen, and S. Kidney, "Gravity-Offloading System for Large-Displacement Ground Testing of Spacecraft Mechanisms," pp. 119–132, 2010.

[61] "Active Response Gravity Offload System." [Online]. Available: http://www.nasa.gov/centers/johnson/engineering/integrated_environments/active_response_gravity/. [Accessed: 15-Jun-2016].

[62] S. A. Mirer and I. V Prilepsky, "Attitude Control of a Small Satellite Prototype on a String Suspension," 2nd *International Workshop Spaceflight Dynamics and Control*, 2006.

[63] M. Clarke, "Cost Effective Attitude Control Validation Test Methods for CubeSats Applied to PolarCube," pp. 1–183, 2016.

[64] M. F. Westgaard, "Hardware Testing of Attitude Control for the NTNU Test Satellite," Project Thesis, Department of Engineering Cybernetics Norwegian University of Science and Technology, 2014.

[65] "Experimental Facilities Tour. Space Propulsion Lab." [Online]. Available: http://web.mit.edu/aeroastro/labs/spl/facilities.html. [Accessed: 15-Jun-2016].

[66] A. Saenz-Otero and D. W. Miller, "SPHERES: a platform for formation-flight research," *Opt. Photonics 2005*, p. 58990O–58990O, 2005.

[67] C. Jewison, D. Sternberg, B. McCarthy, D. W. Miller, and A. Saenz-Otero, "Definition and testing of an architectural tradespace for on-orbit assemblers and servicers," pp. 4–7, 2014.

[68] H. Choset and D. Kortenkamp, "Path planning and control for free-flying inspection robot in space," *J. Aerosp. Eng.*, vol. 12, no. April, pp. 74–81, 1999.

[69] T. Corazzini, A. Robertson, J. C. Adams, A. Hassibi, and J. P. How, "Experimental demonstration of GPS as a relative sensor for formation flying spacecraft," *ION J. Navig.*, vol. 45, no. 3, pp. 195–207, 1998.

[70] Y. Toda, T. Iwata, K. Machda, A. Otsuka, Y. Fukuda, and H. Toriu, "Research and Development of Free-Flying Space Telerobot Ground Experimental Model," *J. Japan Soc. Aeronaut. Sp. Sci.*, vol. 40, no. 467, pp. 652–659, 1992.

[71] D. Friedman, "Laboratory experimentation of autonomous spacecraft docking using cooperative vision navigation," M.A. thesis, Naval Postgraduate School, Monterey, California, 2005.

[72] S. Matunaga, K. Yoshihara, T. Takahashi, S. Tsurumi, and K. Ui, "Ground experiment system for dual-manipulator-based capture of\ndamaged satellites," *Proceedings. 2000 IEEE/RSJ Int. Conf. Intell. Robot. Syst. (IROS 2000) (Cat. No.00CH37113)*, vol. 3, pp. 1847–1852, 2000.

[73] P. Boning, M. Ono, T. Nohara, and S. Dubowsky, "An Experimental Study of the Control of Space Robot Teams Assembling Large Flexible Space Structures," *In Proc. of the 9th International Symposium on Artificial Intelligence, Robotics and Automation in Space*, Los Angeles, CA, 2008.

[74] B. Pond and I. Sharf, "Experimental Evaluation of Flexible Manipulator Trajectory Optimization," *J. Guid. Control. Dyn.*, vol. 24, no. 4, pp. 834–843, 2001.

[75] J. L. Schwartz, M. a. Peck, and C. D. Hall, "Historical Review of Air-Bearing Spacecraft Simulators," *J. Guid. Control. Dyn.*, vol. 26, no. 4, pp. 513–522, 2003.

[76] D. Imgram, W. K. Muench, and L. Rabb, "Dynamic Testing of the Oao Stabilization and Control Subsystem," *Arch. Set 2*, 1963.

[77] W. Haeussermann and H. Kennel, "A Satellite Motion Simulator," *Astronautics*, vol. 5, no. 12, 1960.

[78] H. H. Hoop, "Facilities for simulation Attitude motion of Spacecraft," Technical Report, NASA Marshall Space Flight Center; Huntsville, AL, United States, 1967.

[79] R. B. Voas, H. I. Johnsom, and R. Zedekar, *MercuryProjectSummary, Including Results of the Fourth Manned Orbital FlightMay 15–16, 1963*. 1963.

[80] S. Sanz Fernandez De Cordova and D. B. Derba, "Mass Center Estimation of a Drag-Free Satellite," in *Proceedings of the 6th TriennialWorld Congress of the International Federation of Automatic Control*, 1975, p. 35.3 1–35.3 8.

[81] B. N. Agrawal and R. E. Rasmussen, "Air bearing based satellite attitude dynamics simulator for control software research and development," *Proc. SPIE - Int. Soc. Opt. Eng.*, vol. 4366, no. 831, pp. 204–214, 2001.

[82] J.-W. Kim, R. Cristi, and B. Agrawal, "Attitude Determination for NPS Three-Axis Spacecraft Simulator," *AIAA/AAS Astrodyn. Spec. Conf. Exhib.*, no. August, 2004.

[83] D. Meissner, "A three degrees of freedom test-bed for nanosatellite and cubesat attitude dynamics, determination, and control," Naval Postgraduate School, 2009.

[84] J. Prado, G. Bisiacchi, and L. Reyes, "Three-axis air-bearing based platform for small satellite attitude determination and control simulation," *J. Appl. Res. Technol.*, vol. 3, no. 3, pp. 222–237, 2005.

[85] P. Baker and A. V. Funari, "Army Lightweight ExoAtmospheric Projectile (LEAP)," in *Aerospace Design Conference*, 1992, no. February.

[86] P. K. C. Wang, J. Yee, and F. Y. Hadaegh, "Synchronized Rotation of Multiple Autonomous Spacecraft with Rule-Based Controls: Experimental Study," *J. Guid. Control. Dyn.*, vol. 24, no. 2, pp. 352–359, 2001.

[87] D. Gallardo and R. Bevilacqua, "Six Degrees of Freedom Experimental Platform for Testing Autonomous Satellites Operations," *Proc. 8th ESA Int. Conf. Guid. Navig. Control Systems*, 11 June 2011.

[88] F. Roe, D. Mitchell, B. Linner, and D. Kelley, "Simulation techniques for avionics systems - An introduction to a world class facility," *AIAA Flight Simulation Technologies Conference*, San Diego, CA, July 1996, pp. 535-543.

[89] D. Cho, D. Jung, and P. Tsiotras, "A 5-dof Experimental Platform for Autonomous Spacecraft Rendezvous and Docking," in *Infotech at Aerospace Conference*, 2009.

[90] M. W. Regehr et al., "The Formation Control Testbed," in *Aerospace Conference*, 2004, pp. 557–564.

[91] X. Jian, B. Gang, Yang Qin Jun, and L. Jun, "Design and development of a 5-DOF air-bearing spacecraft simulator," *Proc. - 2009 Int. Asia Conf. Informatics Control. Autom. Robot. CAR 2009*, pp. 126–130, 2009.

[92] "Surrey Satellite Technologies LTD. - Actuators & Sensors." [Online]. Available: https://www.sstl.co.uk/Products/Subsystems/Actuators-Sensors. [Accessed: 23-Jun-2016].

[93] "Berlin Space Technologies - NanoSat Air Bearing." [Online]. Available: http://www.berlin-space-tech.com/index.php_id=45.html. [Accessed: 23-Jun-2016].

[94] C. M. Pong, "High-Precision Pointing and Attitude Estimation and Control Algorithms for Hardware-Constrained Spacecraft," PhD thesis, Department of Aeronautics and Astronautics, MIT, 2014.

[95] S. Chesi et al., "Automatic Mass Balancing of a Spacecraft Three-Axis Simulator: Analysis and Experimentation," *J. Guid. Control. Dyn.*, vol. 37, no. 1, pp. 197–206, 2014.

[96] V. L. Pisacane, *The Space Environment and its Effects on Space Systems*, American Institute of Aeronautics and Astronautics, 2008.

[97] C. I. Reference, "COSPAR International Reference Atmosphere - CIRA-2012 Models of the Earth ' s Upper Atmosphere," pp. 1–37, 2012.

[98] O. L. De Weck, "Attitude Determination and Control (ADCS)," Department of Aeronautics and Astronautics, MIT, Spring 2001.

[99] "International Geomagnetic Reference Field." [Online]. Available: http://www.ngdc.noaa.gov/IAGA/vmod/igrf.html. [Accessed: 10-Jul-2016].

[100] B. Hiller, "Ferraris Acceleration Sensor - Principle and Field of Application in Servo Drives," [Online]. Available: http://www.huebner-berlin.net/pdf/ferraris-acceleration-sensor.pdf. [Accessed: 10-Jul-2016].

[101] Aerotech, *ABRS Series Stage User's Manual*, no. February. 2011.

[102] "Aerotech Inc. - ABRS Air-Bearing Direct-Drive Rotary Stage." [Online]. Available: https://www.aerotech.com/product-catalog/stages/rotary-stages/abrs.aspx. [Accessed: 18-Jul-2016].

[103] "EyasSat, LLC." [Online]. Available: http://eyassat.com/3-degrees-of-freedom-see-how-liberating-it-can-be/. [Accessed: 19-Jul-2016].

[104] G. Burditt, "3DoF Informal Demo." [Online]. Available: https://www.youtube.com/watch?v=8JdkZbAk5ns. [Accessed: 19-Jul-2016].

[105] "Air Bearing Application and Design Guide," datasheet New Way air Bearings, 2006.

[106] "Custom Spherical Air Bearings." NEW WAY air Bearings.

[107] T. Yoshikawa, "Analysis and Control of Robot Manipulators with Redundancy," *Robotics Research The First International Symposium*. pp. 735–747, 1984.

[108] B. Siciliano, L. Sciavicco, L. Villani, and G. Oriolo, *Robotics: Modelling, Planning and Control*. 2009.

[109] D. Galdeano, A. Chemori, S. Krut, and P. Fraisse, "Task-based whole-body control of humanoid robots with ZMP regulation, real-time application to a squat-like motion," *2014 IEEE 11th Int. Multi-Conference Syst. Signals Devices, SSD 2014*, 2014.

[110] J. Gall, B. Rosenhahn, and H. P. Seidel, "Robust pose estimation with 3D textured models," *Lect. Notes Comput. Sci. (including Subser. Lect. Notes Artif. Intell. Lect. Notes Bioinformatics)*, vol. 4319 LNCS, pp. 84–95, 2006.

[111] A. E. Forsman, D. A. Schug, and A. J. Haug, "Multi-camera rigid body pose estimation using higher-order dynamic models," no. February 2016, p. 874407, 2013.

[112] D. Grest, J. Woetzel, and R. Koch, "Nonlinear Body Pose Estimation from Depth Images," *Pattern Recognit.*, pp. 285–292, 2005.

[113] B. Siciliano, "Kinematic control of redundant robot manipulators: A tutorial," *J. Intell. Robot. Syst.*, vol. 3, no. 3, pp. 201–212, 1990.

[114] V. Kilic and B. E. Platin, "Determination of the Position and Orientation of Rigid Bodies by Using Single Camera Images," vol. I, pp. 6–11, 2007.

[115] B. H. Groh et al., "IMU-based pose determination of scuba divers' bodies and shanks," *2015 IEEE 12th Int. Conf. Wearable Implant. Body Sens. Networks, BSN 2015*, 2015.

[116] H. Fourati et al. , "Rigid body motions capturing by means of wearable inertial and magnetic MEMS sensors assembly: From the reconstitution of the posture toward the dead reckoning - an application in Bio-logging," *Devices, Circuits Syst.*, vol. 2012, no. Book 15, pp. 313–329, 2013.

[117] A. D. Young, "Wireless realtime motion tracking system using localised orientation estimation," PhD thesis, Institute of Computing Systems Architecture, School of Informatics, University of Edinburgh, 2010.

[118] "Adept Viper s650/s850 Robot with MB-60R," Datasheet, 2012.

[119] M. Brandst, A. Angerer, and M. Hofbaur, "An Analytical Solution of the Inverse Kinematics Problem of Industrial Serial Manipulators with an Ortho-parallel Basis and a Spherical Wrist," *Proceedings of the Austrian Robotics Workshop*, 2014.

[120] H. A. Ardakani and T. J. Bridges, "Review of the 3-2-1 Euler Angles : a yaw – pitch – roll sequence," Department of Mathematics, University of Surrey, 2010.

[121] W. Khalil and E. Dombre, *Modeling, identification and control of robots*, vol. 56. 2004.

[122] M. Gautier and S. Briot, "New method for global identification of the joint drive gains of robots using a known inertial payload," in *Proceedings of the IEEE Conference on Decision and Control*, 2011, pp. 1393–1398.

[123] C. H. An, C. G. Atkeson, and J. M. Hollerbach, "Estimation of inertial parameters of rigid body links of manipulators," in *Proc. of the 24^{th} IEEE Conf. on Decision and Control*, 1985, vol. 24, pp. 990–995.

[124] M. Gautier and S. Briot, "Dynamic parameter identification of a 6 DOF industrial robot using power model," *2013 IEEE Int. Conf. Robot. Autom.*, pp. 2914–2920, 2013.

[125] I. C. Bogdan and G. Abba, "Identification of mechanical parameters at low velocities for a micropositioning stage using a velocity hysteresis model," *Proc. - IEEE Int. Conf. Robot. Autom.*, pp. 430–435, 2012.

[126] N. L. El Yaaqoubi and G. Abba, "Identification of Physical Parameter included Ground Model Parameter for Walking Robot Rabbit," *9th IEEE-RAS International Conference on Humanoid Robots*, Paris, 2009, pp. 269-276.

[127] J. J. Kim and B. N. Agrawal, "System Identification and Automatic Mass Balancing of Ground-Based Three-Axis Spacecraft Simulator," *AIAA Guid. Navig. Control Conf. Exhib.*, vol. 32, no. August, pp. 1–12, 2006.

[128] J. J. Kim and B. N. Agrawal, "Automatic Mass Balancing of Air-Bearing-Based Three-Axis Rotational Spacecraft Simulator," *J. Guid. Control. Dyn.*, vol. 32, no. May-June, pp. 1005–1017, 2009.

[129] E. Wilson, C. Lages, and R. Mah, "On-line Gyro-based, Mass-Property Identification for Thruster-Controlled Spacecraft Using Recursive Least Squares," *2002 45th Midwest Symp. Circuits Syst. 2002. MWSCAS-2002.*, vol. 2, pp. 334–337, 2002.

[130] J. L. Schwartz and C. D. Hall, "System Identification Of A Spherical Air-Bearing Spacecraft Simulator," *Aas 04-122*, pp. 1–18, 2004.

PUBLICATIONS

1 I. Gavrilovich, S. Krut, M. Gouttefarde, F. Pierrot, and L. Dusseau, “Test Bench for Nanosatellite Attitude Determination and Control System Ground Tests,” in *The Small Satellites Systems and Services (4S) Symposium*, 2014.

2 I. Gavrilovich, S. Krut, M. Gouttefarde, F. Pierrot, and L. Dusseau, “Robotic test bench for CubeSat ground testing: Concept and satellite dynamic parameter identification,” *IEEE Int. Conf. Intell. Robot. Syst.*, vol. 2015-December, pp. 5447–5453, 2015.

3 I. Gavrilovich, S. Krut, M. Gouttefarde, F. Pierrot, and L. Dusseau, “Innovative Approach to Use Air Bearings in CubeSat Ground Tests,” in *The Small Satellites Systems and Services (4S) Symposium*, 2016.

4 I. Gavrilovich, S. Krut, M. Gouttefarde, and F. Pierrot, “Determination of a Rigid Body Orientation by Means of Indirect Measurements,” in *New Trends in Mechanism and Machine Science: Theory and Industrial Applications*, P. Wenger and P. Flores, Eds. Cham: Springer International Publishing, 2017, pp. 61–66.